An analysis of the Global Gravitational Data from the GRACE satellites

Department of Applied Mathematics and Computer Science

Bsc project
Earth and Space Physics and Engineering

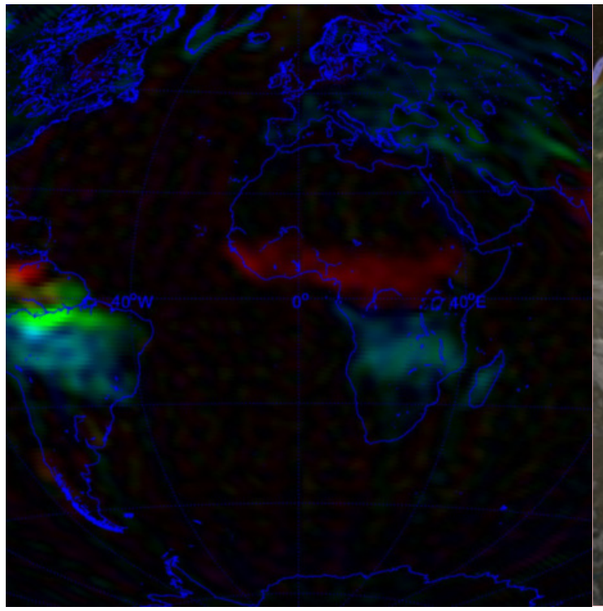

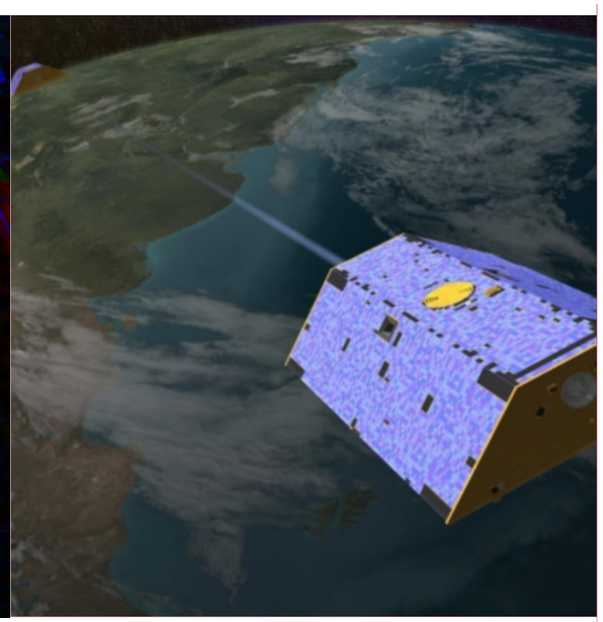

Jonathan Emil Gundorph Jansen, June 2018

Supervisors:
Allan Aasbjerg Nielsen
Ole Baltazar Andersen

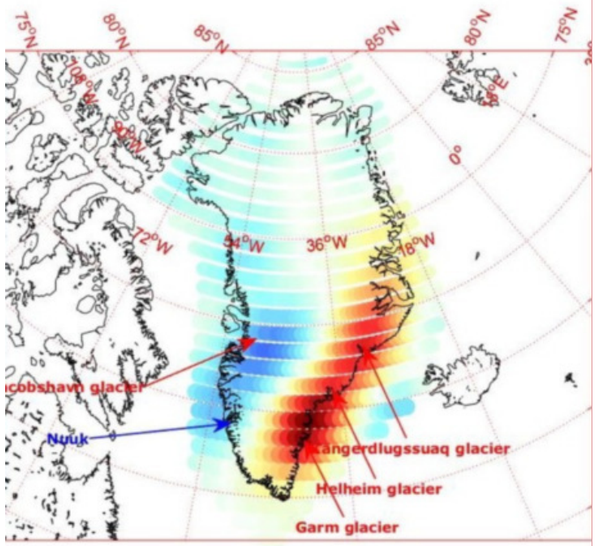

DTU Compute
Department of Applied Mathematics and Computer Science

Department of Applied Mathematics and Computer Science

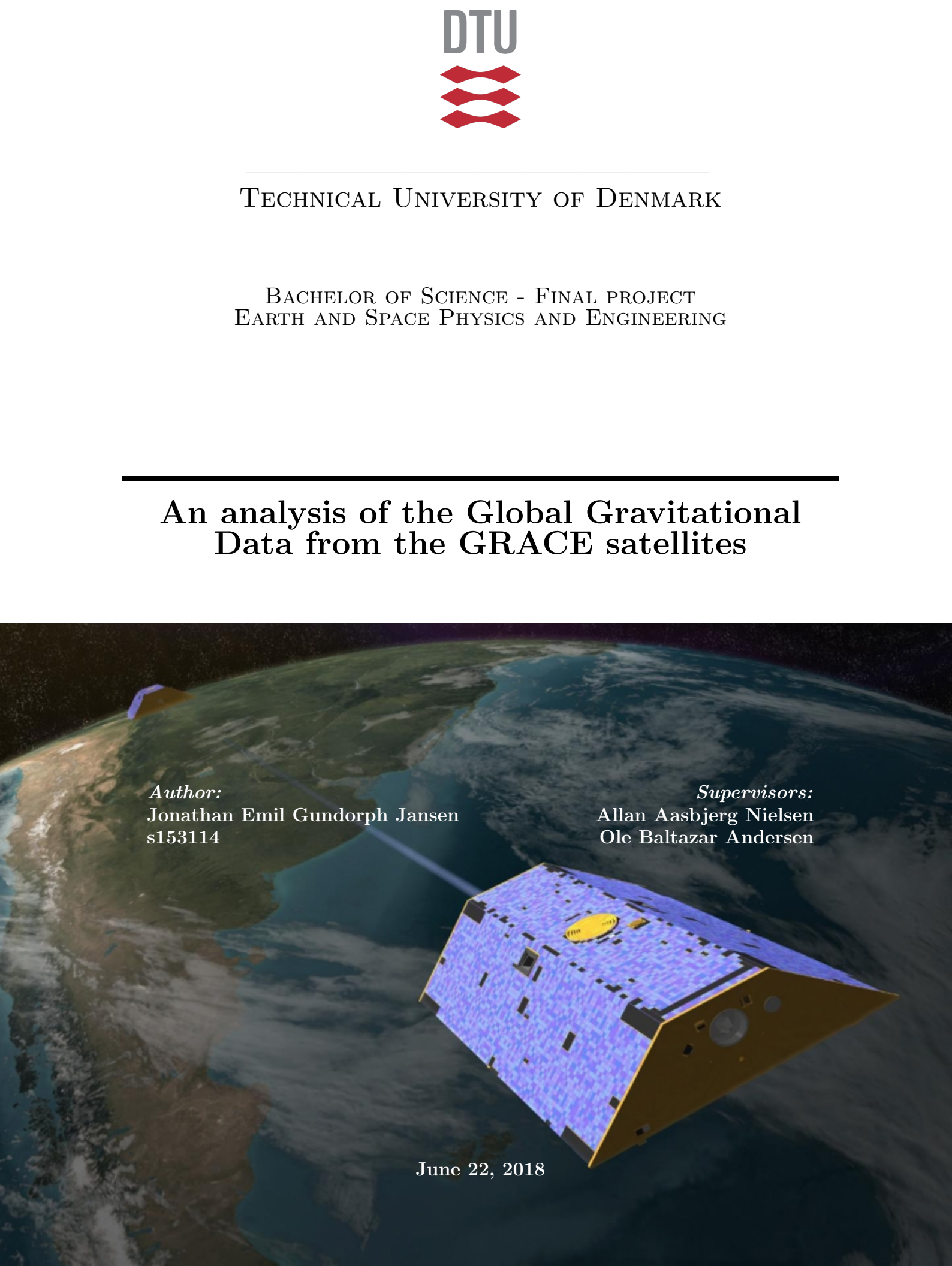

Technical University of Denmark

Bachelor of Science - Final project
Earth and Space Physics and Engineering

An analysis of the Global Gravitational Data from the GRACE satellites

Author:
Jonathan Emil Gundorph Jansen
s153114

Supervisors:
Allan Aasbjerg Nielsen
Ole Baltazar Andersen

June 22, 2018

Technical University of Denmark
Department of Applied Mathematics and Computer Science
Richard Petersens Plads, building 324,
2800 Kongens Lyngby, Denmark
Phone +45 4525 3031
compute@compute.dtu.dk
www.compute.dtu.dk

Abstract

In 2002 NASA launched the GRACE (Gravity Recovery and Climate Experiment) to monitor changes in Earth's gravity on a global scale. This proved to be the most effective method yet for monitoring displacements and movement of water over short time-scales, with very high accuracy.

The goal of this thesis is to analyze the global gravitational data collected by the GRACE twin-satellites, by using regression and principal component analysis and interpreting the results. The open source processed grid data, expressed in an Equivalent Water Height format, was provided by the people of CNES/GRGS, in France.

During this thesis, an analysis was made first on the entire globe, summing up the interesting parts in regards to its distribution of water mass, and then in various regions where substantial changes of water masses are being observed. A full regression model was made for each longitude and latitude point on the globe (there are 64800 of them in total, and they were measured on 454 different time stamps, between 2002 and 2016). This model includes intercept, velocity, acceleration, annual, half annual and $\frac{1}{3}$ annual oscillation estimates, and can express any point at any time on the globe. After this, a separate singular value decomposition and a principal component analysis was made for the data. In this way, it was possible to either analyze the points individually, create a regional (mask) analysis of any place on the Earth, or analyze all of it globally. Additionally, the accuracy of the data was determined using P-values, as well as a Root-Mean-Square error estimate.

In the global analysis, an overview of the water distribution, as well as its dynamical changes between 2002 and 2016, was made. The regression model and the principal component analysis were made for the entire globe, which helped determine what areas were interesting to examine in detail, by looking at the magnitude of the signal, the rate of change, and the magnitude of the amplitude, as well as the phase of different regions.

Following the creation of the global analysis, 7 different regional areas on the globe were studied in closer detail, by creating a mask around them. These different regions express information about different phenomena, such as ice loss trends observed in the Arctic and Antarctic regions, annual oscillations in the rain forests, or large-scale earthquakes in Sumatra or Fukushima. At the end of the paper, the final days of the GRACE satellites, as well as their successor mission the GRACE Follow-on mission, are briefly covered. A discussion of each regional area follows, to attempt to interpret the findings of the results and what implications they might have.

Per the results of the analyses, the areas that were gaining or losing mass in the Arctic and Antarctic regions of Greenland, Alaska, and Antarctica were identified (for example, ice-loss trends were decelerating in south-eastern Greenland, but accelerating in south-western Greenland), and an estimate of the magnitude of annual ice loss was made and visualized for the period of 2002-2016 for these areas as well. In northern South America, the amplitude and phase of the annual oscillation were determined for different areas. In the Caspian Sea located between Europe and Asia, the decline and rate of decline of its water levels were estimated and plotted over time. In the Tibetan Plateau and the Himalayan mountain range, the shift of water-mass balance was determined as well as the magnitude of this shift, between the two regions. Moreover, for Sumatra and Fukushima, the resulting spikes from the gravity change after the large-scale earthquakes of the 21st century were analyzed, resulting in a geographic visualization of the tectonic plate boundaries and movements in these two regions, as seen in the spatial pattern of the principal component analyses.

Preface

This thesis was prepared at DTU Compute in fulfillment of the requirements for acquiring a B.Sc. in Earth and Space Physics and Engineering.

The thesis deals with the analysis of the GRACE satellites gravitational data, on the basis of statistical tools such as regression analysis and principal component analysis. It consists of a global analysis on the entire globe, followed then by several smaller, regional analyses of selected areas around the Earth, such as the Tibetan Plateau, the Amazon Rainforest, the western Antarctica, and others.

I would like to thank my supervisor Allan Aasbjerg Nielsen for tutoring me throughout the project, and dedicating time for me each week to discuss my findings, future approach and the interpretation of my models and results. His mentoring, guidance and teaching has been crucial to my work, and many of the results in this project are derived directly from algorithms and mathematical concepts he taught me.

I would also like to thank my co-supervisor, Ole Baltazar Andersen for assisting me in the complex interpretations of geophysical as well as mathematical concepts, such as correlating principal components and their eigenvectors with real-world phenomena.

I would also like to thank the people of CNES (Centre National d'Etudes Spatiales) and GRGS (Groupe de Recherche de Géodésie Spatiale) for providing the open source, processed RL03-v3 GRACE EWH grid data, so that I may access and work with it. Notably, *R Biancale, J-M Lemoine, G Balmino, S Bruinsma, F Perosanz, J-C Marty (CNES/GRGS, Toulouse, France), S Loyer (CLS, Toulouse, France), S Bourgogne (Toulouse, France), P Gégout (CNRS/GET, Toulouse, France)*

Finally, I would like to extend a big thank you to my family and friends for supporting me throughout the project and helping me proofread this thesis.

Contents

List of Figures

List of Tables

Abbreviations

CNES Centre National d'Etudes Spatiales

DLR Deutsches Zentrum für Luft- und Raumfahrt

ESA European Space Agency

EWH Equivalent Water Height

GIA Glacial Isostatic Adjustment

GPS Global Positioning System

GRACE Gravity Recovery and Climate Experiment

GSHHS Global Self-Consistent Hierarchical High-Resolution Shorelines

HSV Hue Saturation and Value (color model)

NASA National Aeronautics and Space Administration

PC Principal component

PCA Principal Component Analysis

PGR Post-Glacial Rebound

RGB Red Green and Blue (color model)

SVD Singular Value Decomposition

1 Introduction

The purpose of this bachelor thesis is to examine the global gravitational data collected by the twin GRACE satellites.

The GRACE (Gravity Recovery and Climate Experiment) was a joint mission between NASA and the German Aerospace Center (DLR), chosen as the secondary mission under NASA's Earth System Science Pathfinder (ESSP) program, created in 1997. It was a partnership between two of the most influential space agencies in the world, NASA (National Aeronautics and Space Administration) in the United States, and DLR (Deutsche Forschungsanstalt für Luft und Raumfahrt) in Germany. In addition to this, the University of Texas Center for Space Research (UTCSR) in Texas, GeoForschungsZentrum (GFZ) in Potsdam, Germany and the NASA Jet Propulsion Laboratory in California were also involved.

The twin-satellites were designed to map the variations in Earth's gravity field, using GPS and a microwave ranging interferometry system with a precision of up to $10\mu m$. The satellites circled the Earth 15 times a day in a near-polar orbit (89°), and thus collected data from the entire globe, at 500 km (310 miles) altitude (SputnikNews 2017), (Steve Cole 2017).

The two satellites, nicknamed Tom and Jerry (but also known as GRACE-1 and GRACE-2), are moving with a fixed distance of about 220 kilometers (137 miles) between each other, continuously measuring the distance to each other with their microwave ranging interferometry system. When the satellite in the front (Jerry) is entering a region with higher mass, it will travel faster due to the increased gravitational pull from this region, causing a temporary displacement between the satellites, until the other satellite (Tom) enters this region, and thus catches up to the Jerry satellite. These measurements of displacement, made with the GPS module and microwave ranging interferometry, yield essential information about the distribution and flow of mass on, inside and surrounding Earth.

Some of the gravity variations that GRACE can measure include:

1. Variations of mass inside the Earth.
2. Groundwater storage and runoff on land masses.
3. Gravity variations due to changes in the surface and deep currents in the ocean.
4. Interactions between the ocean and ice sheets or glaciers.

In addition to this, another goal of the GRACE satellites is to improve the existing understanding of Earth's atmosphere.
While the satellites provide numerous kinds of important data, the data examined in this project focuses on the gravity field measurements. This data is measured with a 400 km resolution and is expressed as a gravity field in the format [EWH] (Equivalent Water Height) in centimeters [cm]. The format of EWH is elaborated in section 2.1.

2 Theory

2.1 Measuring method: Microwave Ranging Interferometry

The GRACE twin-satellites was capable of tracking the redistribution of water over time with unprecedented accuracy.

As stated previously, this was measured by tracking the distance between the two satellites. Since gravity changes based on how much mass is between the measuring point and the Earths core, when the satellites are flying over an area with greater mass, they will fly a bit faster than usual. Since the satellites are at a fixed distance from each other, the first satellite to enter this region of higher mass will fly faster than the other one, increasing the distance between them. Afterward, the other satellite will increase in speed, and catch up to the first one, restoring their original distance. Based on this little "dance" between the satellites, the scientists can extract the EWH-values from the time and velocity changes during this period (See also illustration in figure 1).
As can be seen in the illustration, the distance between the satellites changes when the first satellite is pulled towards a region of greater mass. So that change, which is continually being measured by the Microwave Ranging Interferometry system, is what tells the scientists what the gravity field underneath them was for such a region.

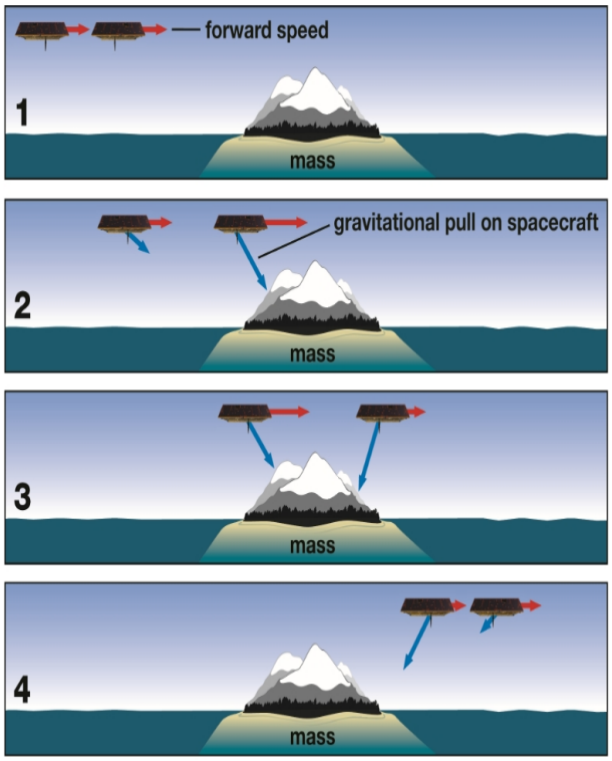

Figure 1: Illustration of the temporal distance change caused by a local gravity field between the GRACE satellites. Source: (NASA/JPL-Caltech 2018)

2.2 The Equivalent Water Height format

The GRACE data is presented in a format known as the Equivalent Water Height.
The GRACE-satellites have collected this in both 10-day periods and monthly periods. The primary focus of the project is to examine the 10-day periods of the GRACE data.
The Equivalent Water Height format is a way to present the local gravity field, expressed in a [1 x 1 x EWH[cm]] water pillar, where EWH is the height of the water pillar, which varies according to the **mass** present in the area. The more mass present, the "higher" the water pillar, and thus the more gravity will affect the satellites. In this way, the satellites can detect how much mass of the dynamic water is present in a grid point. Since the satellites are measuring the same grid points over an extended period (approximately 15 years), it can detect the changes in mass, due to the changes in water/ice being present, over time. Expressing the data in this way is very useful for modeling climate changes and different concepts such as the effects of global warming.

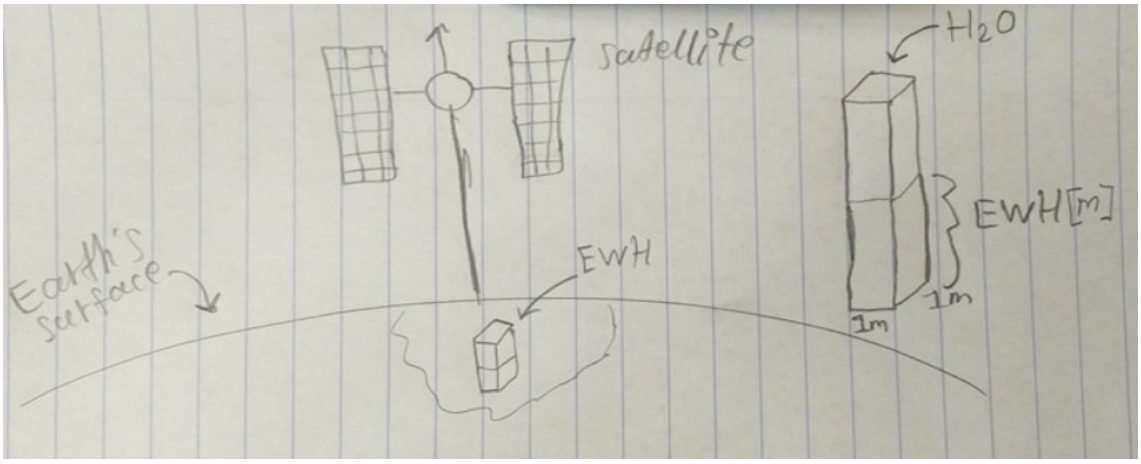

Figure 2: Sketch of the Equivalent Water Height format

In addition to this, due to the incredible accuracy of the GRACE satellites, this can also be used for tracking water on a much smaller scale, such as the amount of rain after a heavy rainfall.

2.3 Other uses of the GRACE satellites

The GRACE satellites use different techniques, from satellite altimetry and radar interferometry to digital terrain models covering vast land and ice areas, to provide essential information in scientific models within many different fields, such Hydrology, Glaciology, Geology, Oceanography and more. However, apart from this, the satellites can also improve scientists understanding of the atmosphere, such as yielding new and better information on the atmospheric pressure, humidity and temperature. This improved understanding of our climate will lead to improved weather forecasts in the future, among other things (Dunbar 2013).

2.4 GRACE Spacecraft and instrumentation

Unlike many other Earth observation satellite missions, the GRACE satellites do not carry a payload of independent scientific instruments.
For example, other Earth observation missions, such as **ICESat (Ice, Cloud and land Elevation Satellite)**, used the **GLAS (the Geoscience Laser Altimeter System)** to measure ice-sheet topography and associated temporal changes, based on transmitted pulses of infrared light and visible green light, whose photons are then reflected back to the satellite from the surface of the Earth (Zwally 2016).

Another example is **TERRA (formerly EOS AM-1)**, which is considered the flagship of NASA's Earth Science missions. TERRA uses, among other things, the **ASTER (Advanced Spaceborne Thermal Emission and Reflection Radiometer)** to obtain high-resolution (15 to 90 square meters per pixel) images of the Earth in 14 different wavelengths of the electromagnetic spectrum, ranging all the way from the infrared light spectrum to the visible light spectrum. This data is then processed to create detailed maps of the land surface temperature, emissivity, reflectance and the elevation (Thome 2018).

In contrast to the previously stated examples, GRACE does not make measurements of the electromagnetic energy reflected back to it from the surface of the Earth, nor does it use other conventional measuring methods. Instead, the bodies of the twin-satellites themselves act as the primary instrument for the measurements, namely, the measurement of the change in distance between them.
A very precise accelerometer is located at each satellites center of mass, and is used to measure

the non-gravitational accelerations induced on the satellites (such as the atmospheric drag), so that only the gravity acceleration from the region of mass itself is considered. The GPS (Satellite Global Positioning System) module is then used to determine the exact location of the satellite, in longitude and latitude coordinates, above the Earth. This position is determined with an accuracy of less than 1 centimeter. Using this data, which is online and open source, scientists can then quickly make a detailed description of the changing gravity profile on Earth, due to the regional mass changes on its surface, over time (Dunbar 2018).

2.4.1 GRACE Instruments

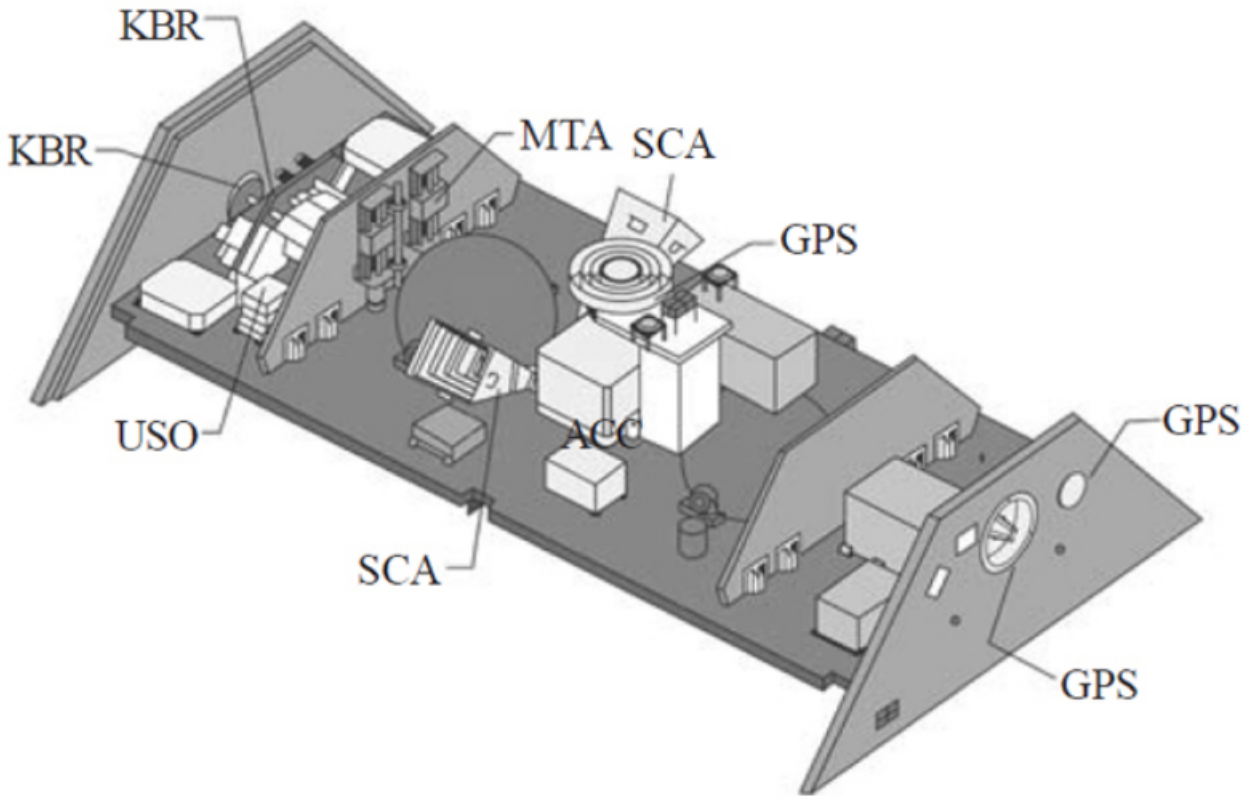

Figure 3: The different components and instruments of the GRACE satellites

Following is a list of the components of GRACE:

1. **K-band Ranging System (KBR)**
   Provides precise (within 10 μm) measurements of the distance change between the two satellites needed to measure fluctuations in gravity.

2. **Ultra Stable Oscillator (USO)**
   Provides frequency generation for the K-band ranging system.

3. **SuperSTAR Accelorometers (ACC)**
   Precisely measures the non-gravitational accelerations acting on the satellites.

4. **Star Camera Assembly (SCA)**
   Precisely determines the two satellite's orientation by tracking them relative to the position of the stars.

5. **Coarse Earth Sun and Sensor (CES)**
   Provides omnidirectional, reliable, and robust, but fairly coarse, Earth and Sun tracking. Used during initial acquisition and whenever GRACE operates in safe mode.

6. **Center of Mass Trim Assembly (MTA)**
   Precisely measures the offset between the satellite's center of mass and the "acceleration-proof" mass and adjusts center of mass as needed during the flight.

7. **BlackJack GPS Receiver and Instrument Processing Unit (GPS)**
   Provides digital signal processing; measures the distance change relative to the GPS satellite constellation.

8. **Globalstar Silicon Solar Cell Arrays (GSA)**
   Covers the outer shell of the spacecraft and generates power.

The information in the above stated list is copied verbatim from the GRACE Science instrument webpage: (Quote: (Dunbar 2018)).

2.5 The Geographic Coordinate System

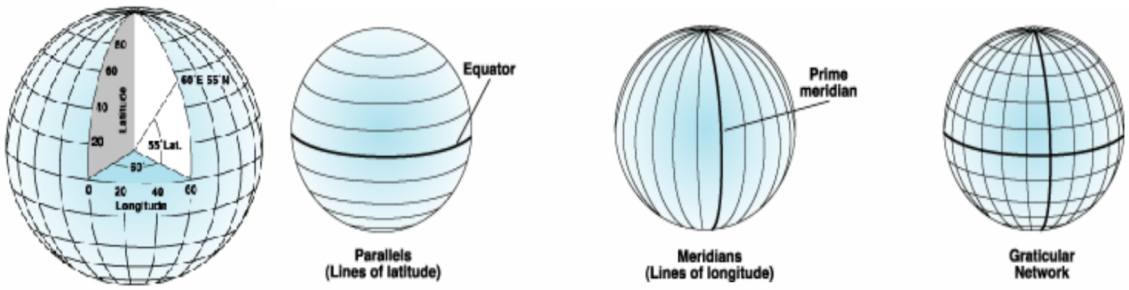

Figure 4: Geographic Coordinate System illustration of the lines of longitude, latitude and the graticular network. Source: (10.3 2018)

The Geographic Coordinate System is a reference system used to pinpoint any geographic location on the surface of the Earth. As seen above in figure 4, the arbitrary position is made out of a longitude and latitude value, which can be perceived as an angle from the center of the Earth to any point on the Earth's surface, measured in degrees (or radians).
The parallels are the lines of latitude and express how far to the north or south the position is, relative to the equator (the equator is at 0° latitude, while the poles are at 90° latitude).
The meridians are the lines of longitude and express how far to the west or east the position is, relative to the prime meridian (The prime meridian is a reference meridian that runs through the city of Greenwich in England). The origin of the graticular network is then the point where the Prime meridian and the equator intersects (0,0).
The distance between two points of longitude varies depending on the position on the globe. It is only at the equator that the distance between two neighboring longitude points is the same as the distance between two neighboring latitude points. However, at positions further to the north or south, the parallel lines get shorter and shorter, while the meridians stay constant. This is because of the spherical nature of the Earth. Thus, as the latitude approximates 90°, the lines of parallels approximates 0 in their circumference, as they converge into a single point at the poles.

In this report, when singular points of longitude and latitude are mentioned, they are addressed as "grid points".

The following table shows the distance between 2 points of longitude at varying degrees of latitude:

Table 1: Distance between degrees of longitude, for varying degrees of latitude

Constant degrees of latitude:	**Distance between 2 degrees of longitude [km]**
0°	**111.32**
30°	**96.40**
60°	**55.66**
90°	**0**

2.6 Glacial Isostatic Adjustment (GIA)

Glacial Isostatic Adjustment is a phenomenon where a land-mass will slowly rise over many thousands of years, in response to the load of ice that was placed upon it and pushed it down during the last Glacial Maximum (commonly known as Ice Age).
During this uprising, the mantle will attempt to pull itself back to its original, pre-Glacial Maximum shape. Figure 5 shows how an ice glacier is loading on a surface, and how it reacts after the ice has melted away.

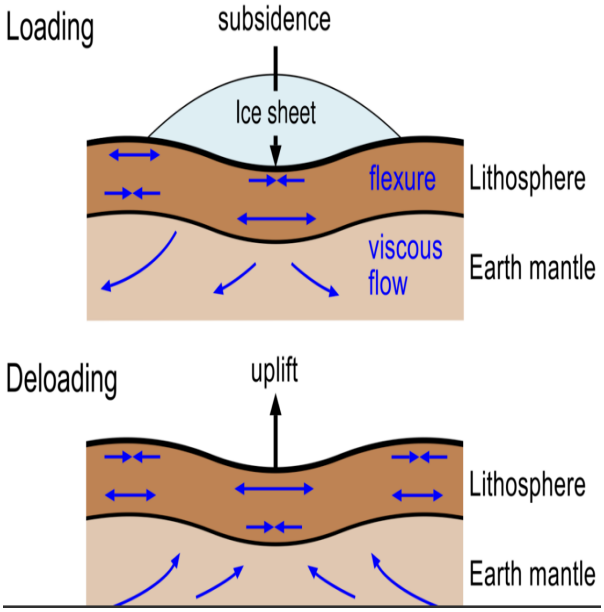

Figure 5: Illustration of the Glacial Isostatic Adjustment.
Picture source: (Klemann n.d.)

The Glacial Isostatic Adjustment effect will induce a significant disturbance in the data of the GRACE satellites, of various magnitudes. This needs to be taken into account when measuring the total amount of loss of ice each year. The magnitude of the error that the GIA effect will induce depends on the model of correction used. In the study *Greenland and Antarctica Ice Sheet Mass Changes and Effects on Global Sea Level* (Scambos and Koenig 2013), it was stated that an international collaboration of polar scientists known as the IMBIE team measured about $\pm 25 Gt/yr$ for Greenland and $\pm 50 Gt/yr$ for Antarctica, predominantly from the GIA effect, in a separate study. This was after the use of the "standard" model for GIA corrections in Greenland and Antarctica. Due to the limiting scope of this project, no model was used to correct for the GIA error, so GIA-errors are likely to be higher.

The GIA-effect is observed in all the areas that were covered by the large ice-sheets of the last Glacier Maximum, so in the analysis, its effect only needs to be taken into account for the areas of Greenland, Alaska, and Antarctica.

3 Method

In this project, various mathematical concepts and algorithms have been used to analyze the GRACE EWH grid data. These include a regression analysis, estimates of amplitude and phase constants, statistical significance and RMSE estimates and a singular value decomposition and principal component analysis. Furthermore, various mapping tools for visualization and projection has been used, as well as corrections for the spherical Earth curvature. All of these algorithms, tools, and concepts can be seen elaborated in this section.

3.1 Regression Analysis

The output of the regression analysis contains all intercepts, velocities, accelerations and annual, half-annual and $\frac{1}{3}$ annual (seasonal) oscillations for the EWH-values, expressed in amplitude and phase constants for every 64800 grid points of each timestamp (out of 454 timestamps). It is constructed as the following;

From the GRACE satellites, all the Equivalent Water Height data from each grid point are obtained, for every timestamp. The grid points are distributed in a network according to their longitude and latitude values, with 180 observations from the north pole to the south pole and 360 observations from east to west, around the globe. This adds up to a total of $180 \cdot 360 = 64800$ grid points for each timestamp.
Each grid point can be expressed through the following formula, where i is the index:

$$EWH_i = \theta_0 + \theta_1 \cdot t_i + \frac{1}{2} \cdot \theta_2 \cdot t_i^2 + \theta_3 \cdot sin(\frac{2\pi t_i}{T}) + \theta_4 \cdot cos(\frac{2\pi t_i}{T}) + \theta_5 \cdot sin(\frac{2\pi t_i}{2T}) + \theta_6 \cdot cos(\frac{2\pi t_i}{2T}) + ... \\ ... + \theta_7 \cdot sin(\frac{2\pi t_i}{3T}) + \theta_8 \cdot cos(\frac{2\pi t_i}{3T}). \tag{1}$$

where $T = 365.25$ days.

Now, it might be interesting to look at the velocity, acceleration and the yearly oscillations expressed through the θ values. These can be solved for, using simple linear algebra and matrix transformations.
First, the equation is transformed into matrix form like so;

$$A \cdot \begin{bmatrix} \theta_0 \\ \theta_1 \\ \cdot \\ \cdot \\ \cdot \\ \theta_8 \end{bmatrix} = \begin{bmatrix} EWH_{1,1} & EWH_{1,2} & EWH_{1,3} & .. & .. & EWH_{1,M} \\ EWH_{2,1} & EWH_{2,2} & .. & .. & .. & .. \\ EWH_{3,1} & .. & .. & .. & .. & .. \\ .. & .. & .. & .. & .. & EWH_{P-1,M} \\ EWH_{P,2} & .. & .. & .. & EWH_{P,M-1} & EWH_{P,M} \end{bmatrix} \tag{2}$$

where $P = 454, M = 64800$, and

$$A = \begin{bmatrix} 1 & t_1 & \frac{1}{2}t_1^2 & sin(\frac{2\pi t_1}{T}) & cos(\frac{2\pi t_1}{T}) & .. & .. & cos(\frac{2\pi t_1}{3T}). \\ 1 & t_2 & \frac{1}{2}t_2^2 & sin(\frac{2\pi t_2}{T}) & cos(\frac{2\pi t_2}{T}) & .. & .. & cos(\frac{2\pi t_2}{3T}). \\ 1 & t_3 & \frac{1}{2}t_3^2 & sin(\frac{2\pi t_3}{T}) & cos(\frac{2\pi t_3}{T}) & .. & .. & cos(\frac{2\pi t_3}{3T}). \\ .. & .. & .. & .. & .. & .. & .. & .. \\ .. & .. & .. & .. & .. & .. & .. & .. \\ 1 & t_P & \frac{1}{2}t_P^2 & sin(\frac{2\pi t_P}{T}) & cos(\frac{2\pi t_P}{T}) & .. & .. & cos(\frac{2\pi t_P}{3T}). \end{bmatrix} \tag{3}$$

the system is then denoted as

$$\underline{y} = \underline{\underline{A}}\, \underline{\theta} - r \tag{4}$$

where r = residual.
Following, the residuals are minimized:

$$min\ \underline{r}^T\underline{r} = (\underline{\underline{A}}\,\underline{\theta} - y)^T(\underline{\underline{A}}\,\underline{\theta} - \underline{y}) \tag{5}$$

Then the minimum is found, by setting

$$\frac{d\,\underline{r}^T\underline{r}}{d\,\underline{\theta}} = 0 \tag{6}$$

and one finally obtains

$$\underline{\underline{A}}^T\underline{\underline{A}}\,\hat{\underline{\theta}} = \underline{\underline{A}}^T\underline{y} \tag{7}$$

$$\hat{\underline{\theta}} = (\underline{\underline{A}}^T\underline{\underline{A}})^{-1}\underline{\underline{A}}^T\underline{y} \tag{8}$$

Now one has an expression for the 9 θ-values for every 64800 grid points on the globe. Thus, an expression for the velocity, acceleration and annual, half-annual and $\frac{1}{3}$ annual oscillations for every grid point on the globe, measured from the period 2002-2016, is calculated (A. A. Nielsen 2013).

3.2 Phase and amplitudes

After obtaining the θ-values, it may be of interest to get estimates for the phase and amplitude data (which expresses the annual oscillations) from the sin and cos terms of the theta values (θ_3 and θ_4).

3.2.1 Trigonometric formulas

Generally, by using the expression for sinusoidal motion and trigonometric identities, it can be seen that

$$x = A \cdot sin(\frac{\omega_0 \cdot t}{T} + \phi) = [A \cdot sin(\phi)] \cdot cos(\frac{\omega_0 \cdot t}{T}) + [A \cdot cos(\phi)] \cdot sin(\frac{\omega_0 \cdot t}{T}) = \tag{9}$$

$$B \cdot cos(\frac{\omega_0 \cdot t}{T}) + C \cdot sin(\frac{\omega_0 \cdot t}{T}). \tag{10}$$

The specific theta values below can also be expressed as:
$\theta 3$, $\theta 5$ $\theta 7 = [A \cdot cos(\phi)] = \mathrm{C}$, $\theta 4$, $\theta 6$ $\theta 8 = [A \cdot sin(\phi)] = \mathrm{B}$
Following this, an expression for the amplitude and phase can be reached:
Amplitude $\mathrm{A} = \sqrt{B^2 + C^2}$
Phase $\phi = tan^{-1}(\frac{B}{C})$

3.3 The significance of the model parameters

When doing data analysis, it is often desirable to have some estimate of how good the model is. There are different statistical approaches to determine this. The ones used in this project include:

1. **Root-Mean-Square Error (RMSE)**
   This is a measure of the differences between the data values predicted by the estimate and the actual values observed. In other words, it represents the sample standard deviations of the differences between the observed values and those the model predicts, known as *residuals*. It is an excellent way to obtain information about the *accuracy* of one's model.

2. **T-values**
   The t-values (or t-statistic) is used in hypothesis testing. It is used to test, within the observed data, factors that would distinguish the null hypothesis from the alternative hypothesis. For example, it could be used to measure how an estimated value of a parameter differs between its hypothesized value and its standard error, or to test if two data sets are significantly different from each other. For large samples, t-distributed data assumes a normal distribution. From the t-values, one can compute the P-values:

3. **P-values**
   P-values is a way to test how significant a result is, and whether or not it can reject the null hypothesis (which, by default, is that there is no significant difference between the result and the sample mean). If the null hypothesis can be rejected (usually with 95% confidence), the result is denoted as being *"Statistically significant"*.
   If assuming some t-distributed data with a large sample size, it can be tested whether or not the result falls inside the rejection area, as illustrated in figure 6 (Brockhoff et al. 2017)

In the example seen in figure 6, a t-value could be calculated to be equal to 2.6. The critical value (denoting the boundary between the 95% and upper 5% area of the confidence bell curve) was 1.645, and thus the p-value, which is the area of the curve above 2.6, was calculated to be equal to $P = 0.0096$. Thus, it could be concluded that the data value was significantly different from the mean with 95% confidence, because $p = 0.0096 < 0.05$, and the null hypothesis H0 could be rejected.

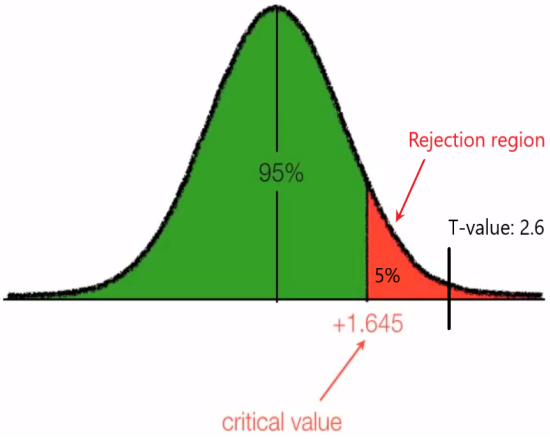

Figure 6: Example for computing the one-tailed t-test

3.4 Calculating the RMSE

All calculations were done in Matlab.
From previously, 9 parameters were estimated for the GRACE data: $\theta_0, \theta_1, ..., \theta_8$ for each of the 64800 grid points.
The matrix **EWH** is the matrix of observed EWH values from the GRACE satellites. It is denoted as y. The theoretical, predicted EWH values are calculated with the [454x9] matrix **A** and the theta parameters, and is denoted as $\hat{y}$ (please refer to earlier regression analysis section, where this is more explicitly shown). It is calculated with the following expression:

$$\hat{y} = \mathbf{A} \cdot \theta \tag{11}$$

where A can be seen defined earlier in section 3.1. The two matrices, y, and $\hat{y}$ differs by the value ϵ, which is the residual errors between the two models.
Then the MSE (Mean Squared Error) of the residuals is obtained, which is the sum of the residuals squared divided by the degrees of freedom, f.

$$\mathbf{MSE} = \frac{1}{f} \cdot \sum (y - \hat{y})^2 \tag{12}$$

where $f = 454 - 9 = 445$
Following this, the Root Mean Squared Error values, which is the square root of the MSE values, are calculated:

$$\mathbf{RMSE} = \sqrt{\mathbf{MSE}} \tag{13}$$

The 64800 RMSE-values are obtained, one for each grid point. In other words, **RMSE** expresses the accuracy of the entire 9-parameter model for each grid point.
For an illustration of the RMSE plotted on a world map, please see section 4.1.2 (A. A. Nielsen 2013).

3.5 Calculating the T-values

When the T-values are calculated, the previously calculated RMSE values can conveniently be used. This leads to a t-value for *each parameter of each grid point*, for all of the grid points.

In general, a t-statistic is calculated in the following way:

$$\frac{\hat{\beta} - \beta_0}{s.e.(\hat{\beta})} \tag{14}$$

Where $\hat{\beta}$ = An estimator of the parameter B, B_0 = A non-random known constant, often = 0 by default, and $s.e.(\hat{\beta})$ = The Standard Error of $\hat{\beta}$. It can also be found by dividing a residual by the sample standard deviation, like so:

$$g(x, X) = \frac{x - \hat{X}}{s} \tag{15}$$

where s = sample standard deviation, $\hat{X}$ = mean of x and x = the observation.
This approach is the more relevant one for this project.
Since the data has a considerable sample size (n = 454), a normal distribution can safely be assumed, because a t-distribution assumes a normal distribution for large samples sizes ($n > 30$).

All calculations were done in Matlab.
When dealing with matrices, a slightly different approach has to be taken. First, the standard deviations for the θ parameters are calculated.
To obtain the standard deviations for the 9 parameters, a new matrix, **iXX**, is created as

$$\mathbf{iXX} = (\mathbf{A}^T \cdot \mathbf{A})^{-1} \tag{16}$$

where A is defined earlier in section 3.1.
The matrix **A** is constant, as it is only dependent on time.
Then, **iXX** is a square 9x9 matrix.
Now, returning to the **RMSE**, it was calculated with the formula

$$\mathbf{RMSE} = \sqrt{\frac{1}{n-9} \cdot \sum (y - \hat{y})^2} \tag{17}$$

which is very similar to the general formula for the standard deviations:

$$\mathbf{Standard\ Deviations} = \sqrt{\frac{1}{n-1} \cdot \sum (x_i - \hat{x})^2} \tag{18}$$

Thus, by multiplying each RMSE value by the square root of the diagonal of **iXX**, the standard deviations for each θ parameter, for each grid point, are obtained.

The standard deviations are computed with the Kronecker Tensor Product, which takes as input 2 matrices, **A** and **B**, and then forms a new matrix by taking all possible products between the elements of **A** and the matrix **B**.
Thus, the matrix **B** is multiplied by each element of **A**.
The Kronecker Tensor product, Kron(A,B), takes as input A (the $1x64800$ RMSE vector), and

B (the square root of the diagonal of the matrix iXX).

Then, the new 9x64800 matrix **Dthetah** is determined, which contains all the standard deviations for each parameter for each grid point.

Following this, one can get the corresponding t-values, by dividing the estimates, θ, with the standard deviations of the estimates, **Dthetah**.
Then, the 9x64800 matrix **t_ford**, which contains all the t-values for each parameter for each grid point, is determined (A. A. Nielsen 2013), (Brockhoff et al. 2017).

3.6 Calculating the P-values

The previously calculated t-values in **t_ford** can be used to calculate the p-values by inserting them into the following Matlab expression: $2 \cdot tcdf(abs(t\_ford), df, 'upper')$, which takes as input the matrix of t-values and the degrees of freedom, and calculates the p-value for each t-value in the matrix **t_ford**. The p-value calculated here is for the one-tailed t-test, with the upper tail or rejection region being the final 5% of the bell curve area (significance level, α, is 0.05). As mentioned before, *if the area of the bell curve above the t-value is less than the significance level, α, the null hypothesis is rejected, and the t-value is statistically significant.*
Then, a measure of the p-values of each parameter of each grid point is obtained, denoted as the 9x64800 matrix, **P**.
To see an illustration of the p-values of the velocity and acceleration parameters plotted on a world map, please refer to section 4.1.2 (Brockhoff et al. 2017).

3.7 SVD - Singular Value Decomposition

The SVD operation is essentially a factorization of a real or a complex matrix.
Supposing A is a m x n matrix, whose values stems from the field k, which is a field of either real or complex numbers. Then there exists a factorization called a singular value decomposition of the matrix A, of the form

$$M = U\Sigma V^T \tag{19}$$

where
U = m x n unitary matrix over the field k (if k = R , the unitary matrix are an orthogonal matrix).
Σ = a diagonal m x n matrix with non-negative real numbers on its diagonal.
V^T = a conjugate transpose of the matrix V, which is a n x n unitary matrix over the field k.
The diagonal elements of the matrix Σ are also known as the singular values of the matrix A (7.548 2002), (Leskovec and Ullman 2016).

3.7.1 Application of SVD

A singular value decomposition on the [64800 x 454] matrix EWH, which contains the 454 columns of timestamps as variables, and 64800 rows as "samples", is computed. However, since running a normal SVD-operation on a matrix of this size would require a huge amount of memory and execution time, the SVD was computed with the 'economy' option instead, in Matlab. As stated in the documentation, "The economy-size decomposition removes extra rows or columns of zeros from the diagonal matrix of singular values, S, along with the columns in either U or V that multiply those zeros in the expression $A = U \cdot S \cdot V'$. Removing these

zeros and columns can improve execution time and reduce storage requirements without compromising the accuracy of the decomposition." (Quote: (Mathworks n.d.)).

$$EWH = \begin{bmatrix} -17.5420 & -17.4250 & -17.3100 & ... & ... & .. & .. & -14.8030. \\ -24.7680 & -24.6930 & -24.6210 & ... & ... & .. & .. & -6.7860. \\ . & . & . & . & . & . & . & . \\ . & . & . & . & . & . & . & . \\ 5.2570 & 5.2700 & 5.2840 & ... & ... & .. & .. & 5.3880. \end{bmatrix} \tag{20}$$

Which returns the following output: $EWH = [U, S, V]$
U = [64800 x 454] matrix of singular vectors.

$$U = \begin{bmatrix} -0.0010 & 0.0027 & 0.0018 & ... & ... & .. & .. & 0.000812. \\ -0.0010 & 0.0027 & 0.0018 & ... & ... & .. & .. & 0.000814. \\ . & . & . & . & . & . & . & . \\ . & . & . & . & . & . & . & . \\ 0.0013 & -0.0029 & -0.0034 & ... & ... & .. & .. & 3.1905e-04. \end{bmatrix} \tag{21}$$

S = [454 x 454] diagonal matrix containing the singular values.

$$S = \begin{bmatrix} 4.9400 & 0 & 0 & ... & ... & .. & .. & 0. \\ 0 & 1.7447 & 0 & ... & ... & .. & .. & 0. \\ . & . & . & . & . & . & . & . \\ . & . & . & . & . & . & . & . \\ 0 & 0 & 0 & ... & ... & .. & .. & 409.6763. \end{bmatrix} \tag{22}$$

V = [454 x 454] matrix of eigenvectors belonging to A.

$$V = \begin{bmatrix} 0.0499 & -0.0199 & 0.0230 & ... & ... & .. & .. & -0.0098. \\ 0.0499 & -0.0305 & 0.0139 & ... & ... & .. & .. & 0. \\ . & . & . & . & . & . & . & . \\ . & . & . & . & . & . & . & . \\ -0.0968 & 0.0033 & -0.0105 & ... & ... & .. & .. & -0.0026. \end{bmatrix} \tag{23}$$

3.8 Principal Component Analysis (PCA)

A Principal Component Analysis is a way to make a linear orthogonal transformation of a large dataset of observations with possibly correlated values into a dataset of linearly uncorrelated variables called principal components.

The principal components are vectors, ranked in order of magnitude, and each principal component corresponds to a certain amount of variance in the original dataset. Thus, the first principal component (PCA1) in the set corresponds to the largest amount of variation, and is considered the "most important". The following principal components are ranked similarly, so the second PCA corresponds to the second most variation, and so forth.
A good way to illustrate the "importance" of each principal component is to make a "scree plot". A scree plot is a bar plot of how much variance each principal component accounts for. An example of this is seen below, where a scree plot is made for the principal component analysis of the global EWH data.

Using the singular value decomposition computed in the previous chapter, a principal component analysis is calculated. The independent columns in the U matrix can be read as the principal components, the diagonals in the Σ as the singular values, and the columns in V as the eigenvector for each principal component.
Also, if one squares the singular values in the Σ matrix, the eigenvalues for each principal component are obtained.

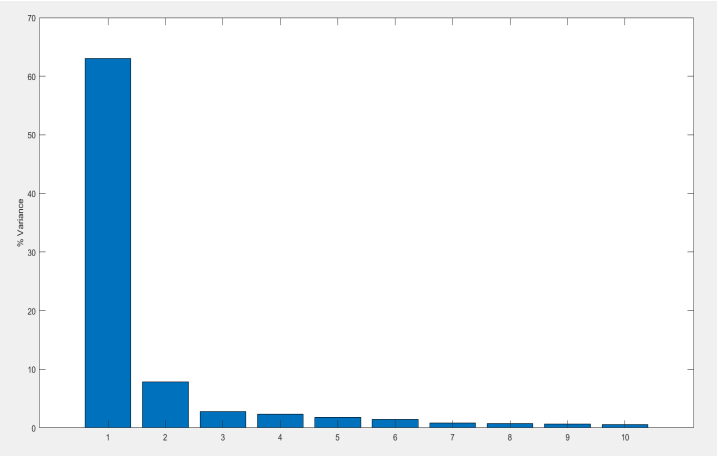

Figure 7: Example of a scree plot for a principal component analysis

This is done on the singular value decomposition from before, which returns information about the principal components (Starmer 2018), (Chen et al. 2017b).

3.9 The Matlab *M_Maps* package

The Matlab *M_maps* package is a user-made mapping toolbox for Matlab and Octave. It is open source and freely available for anyone who wishes to use it.
Throughout this project, the *M_map* mapping toolbox has been used extensively for all geographic projections and visualizations. For the global projections, a *Hammer-Aitoff* projection was chosen, due to its realistic representation and shape of the Earth, and because it has meridians curving together near the poles. For smaller, more zoomed in projections, such as in the analyses of regional areas, the projection depended on the latitude extent of the area to project. For far northern/southern extensions, a *Stereographic* projection was chosen, because of its "bullseye" pattern of latitude lines, meaning the latitude lines comes together at the poles.
For areas near the equator, such as northern South America, Tibet, Sumatra, and others. a *conic Albers Equal-area* projection was chosen, which works well for mid-latitude areas with a large east/west extent.

Figure 8: M_maps logo

The *m_maps* package can provide the user with many different options and plotting tools, including

1. A global coastline database with a $\frac{1}{4}$ degree resolution.
2. An algorithm to make good-looking axes with limits either in a X/Y coordinate plane or with longitude and latitude limits.
3. Algorithms to project different geographical areas and data in 19 different projections, (and provide inverse mappings), using ellipsoidal and spherical Earth models.
4. A 1-degree resolution global elevation database.
5. Ability to quickly and efficiently access high-resolution coastlines and bathymetry databases to project and visualise your work.
6. Many other things.

(Eoas.ubc 2018)

3.10 Decreasing area correction for large latitude extents.

When determining the amount of mass loss in an area, it is important to keep in mind that the area of each grid point decreases, as one moves further northwards or southwards (See also section 4).
Hence, this needs to be taken into account when summing up the total amount of EWH in a given region.
The weighted sum formula below can be used to determine the total amount of mass in an area for each timestamp:

$$Total - EWH - of - region = \frac{\sum_{n=1}^{N} \Delta h \cdot cos(lat)}{\sum_{n=1}^{N} cos(lat)} \tag{24}$$

where Δh is the Equivalent Water Height of any n'th grid point (in [cm]).

3.11 Matlab Mask creation

A significant portion of this report consists of the smaller, zoomed-in analyses of regional areas, such as Greenland, northern South America, the Tibetan Plateau and others, by drawing a "mask" around them. The following algorithm was used to compute this:
First, the original [64800 X 3 X 454] matrix of EWH data was reshaped and permuted into a [180 X 360 X 454] format. This was done by omitting the vectors of longitude and latitude and letting the index of each cell denote the latitude and longitude instead, where each cell contained the value of the EWH at each timestep.
Following this, the data had to fit Matlabs inbuilt coastlines, which is made in a different format than GRACE EWH-data. To match the data with Matlab's coastline function, the vector order was flipped, and the first 180 entries of longitudes switched places with the last 180 entries of longitude (to get it into a -180:180 longitude format instead of the 0:360 longitude format). Finally, the entire matrix was flipped left to right using the fliplr function. Now, the array was in the proper format, and it was visualized with the Matlab command *imshow* along with Matlab's inbuilt coastlines function.
Now, the user can freely determine any polygon of the shown map using the Matlab inbuilt function roipoly. After a mask was chosen and returned, the data was transformed back into the [N X 3 X 454] format, using the same steps as previously but in reverse order, and assigning the proper longitude and latitude values to the proper EWH values of the mask. The size of the mask N depended on the size of the chosen mask.
When back in this original format, the mask can then be plotted and worked with using the *m_maps* toolbox.

4 Results

In this section, the tools and algorithms covered in the Method section (3) are applied to provide meaningful results that can be applied to real-world phenomena, first in a global analysis and then in a smaller, regional analysis of different areas of interest.
For each analysis, a regression analysis model is first estimated for each grid point of longitude and latitude. This model includes parameters such as the velocity and acceleration estimates, and amplitudes to three pairs of cosinus and sinus terms, that together express the annual, half-annual and $\frac{1}{3}$ annual oscillations, respectively. Then from these terms, a phase and amplitude constant is determined, to show the oscillation of each grid point. Following this, the statistical significance and RMSE estimate of each grid point are analyzed. Finally, a singular value decomposition and a principal component analysis for the areas of interest (both globally and regionally), are calculated.

4.1 Global analysis

Now that all the tools necessary for doing a complete analysis of the data has been covered, it is time to analyze the data more closely. First, the velocity and acceleration parameters from the regression model are examined:

4.1.1 Velocity and Acceleration parameters

It is interesting to observe the rate of change in mass in different areas of the world. Which regions are gaining or losing mass, and how fast? Also, is this tendency of mass change accelerating or decelerating?

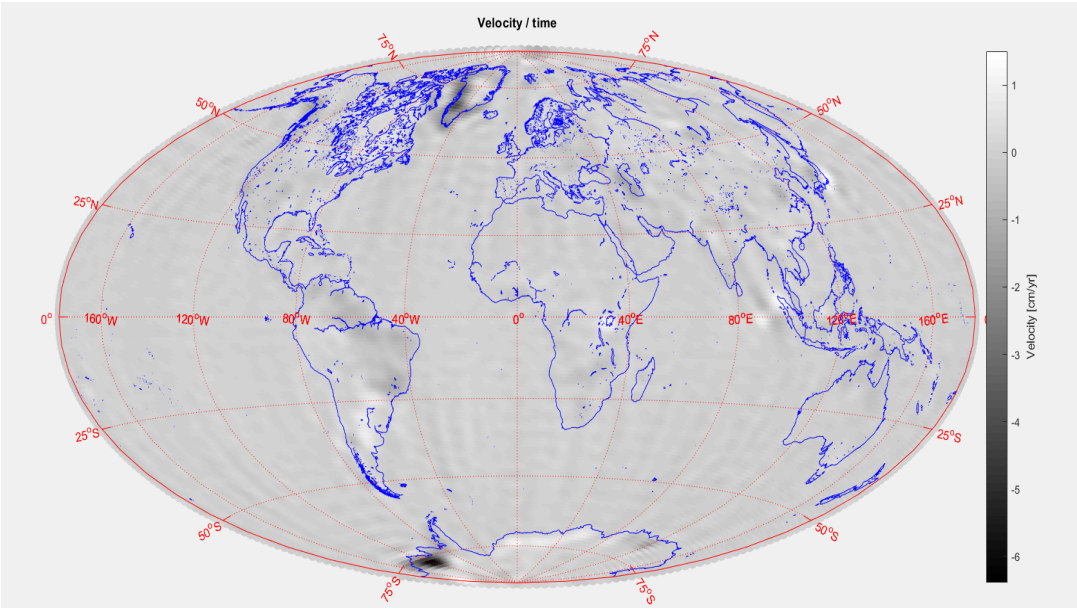

Figure 9: Global analysis - Velocity parameters as of 15-Jun-2016

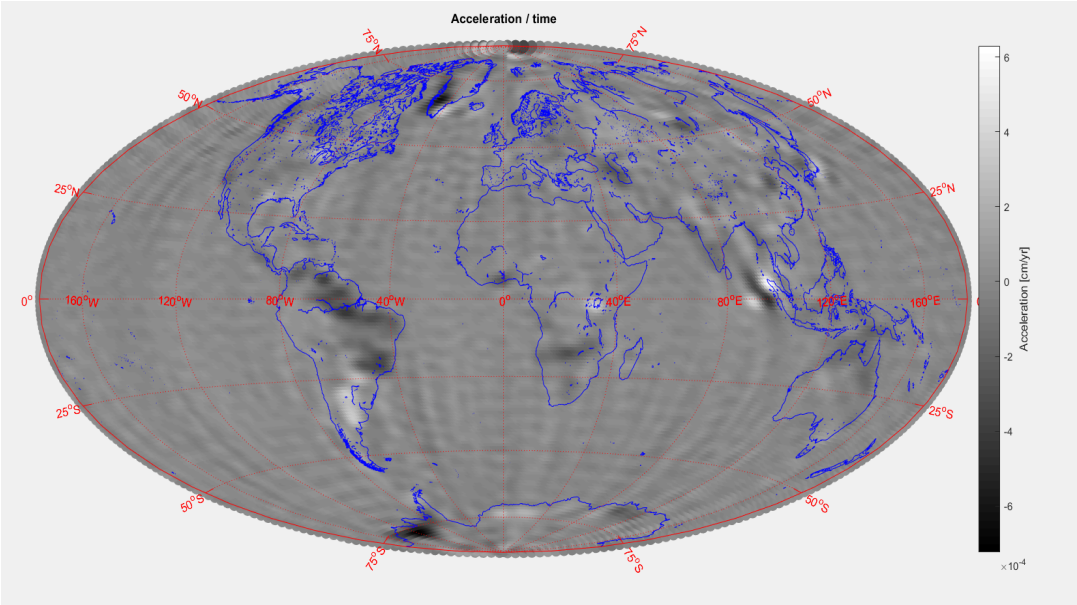

Figure 10: Global analysis - Acceleration parameters

As seen in figure 9, the largest negative velocity is found at Greenland's southwest coast, as well as a considerable negative velocity at west Antarctica (as of 15th of June, 2016). However, if one compares this plot with the plot of the accelerations in figure 10, a **positive** acceleration in south-east Greenland can be seen, for example.

This is due to the acceleration being calculated across the entire period, and the velocity only being an estimate at the very last timestamp. Hence, the way to interpret this is that, even though there might have been a substantial melt-off of ice in south-eastern Greenland through the majority of the period, that trend has stopped, and it is decelerating now. A positive acceleration in south-eastern Greenland does not mean that it is gaining mass, but that the **tendency of loss of mass in south-eastern Greenland is decreasing**.

Another fascinating phenomenon worth considering is the substantial acceleration and velocity values at Sumatra, Indonesia. This large signal is due to the massive Sumatra-Andaman islands earthquake in Sumatra, Indonesia on Boxing day, 25th of December 2004, measuring 9.1-9.3 of moment-magnitude. It was caused by the Indian tectonic plate being subducted by the Burma tectonic plate, and triggered several tsunami's (Japanese for "harbor wave", which is a special type of sea-wave that can be triggered by factors that creates long-wavelength disturbances of the ocean surface, such as an uplift or a large-scale collapse of part of the ocean floor, for example). (Fundamentals of Geophysics). This destructive tsunami hit most countries bordering the Indian Ocean, probably killing more than 250,000 people in many different countries bordering the Indian Ocean, as far away as Somalia.

The displacements on the fault were 20 m, and it had a rupture zone of about 1300 km in length, and 150 km in width, and the earthquake also the longest duration of faulting ever recorded (atleast 10 minutes) (Technology n.d.). This massive movement of mass, over such a (relatively) short period, caused the ocean bottom to uplift several meters, which caused the destructive tsunami in 2004 (Fundamentals of Geophysics).

And this huge movement of mass was why it was seen so clearly on the plot, even though the event only lasted for such a short time during the 14 year period. For further elaboration on this event and other earthquakes, please see section 4.2.7.

4.1.2 Statistical significance and accuracy of the model and its parameters (P-values and RMSE)

As mentioned earlier in section 3.4 and 3.6, estimates for the accuracy of the model (the Root-Mean-Square Error) as well as the statistical significance (p-values) for each parameter has been calculated. These can also be illustrated on a world map, to show where the model is more precise and less precise:

P-values of the velocity and acceleration:

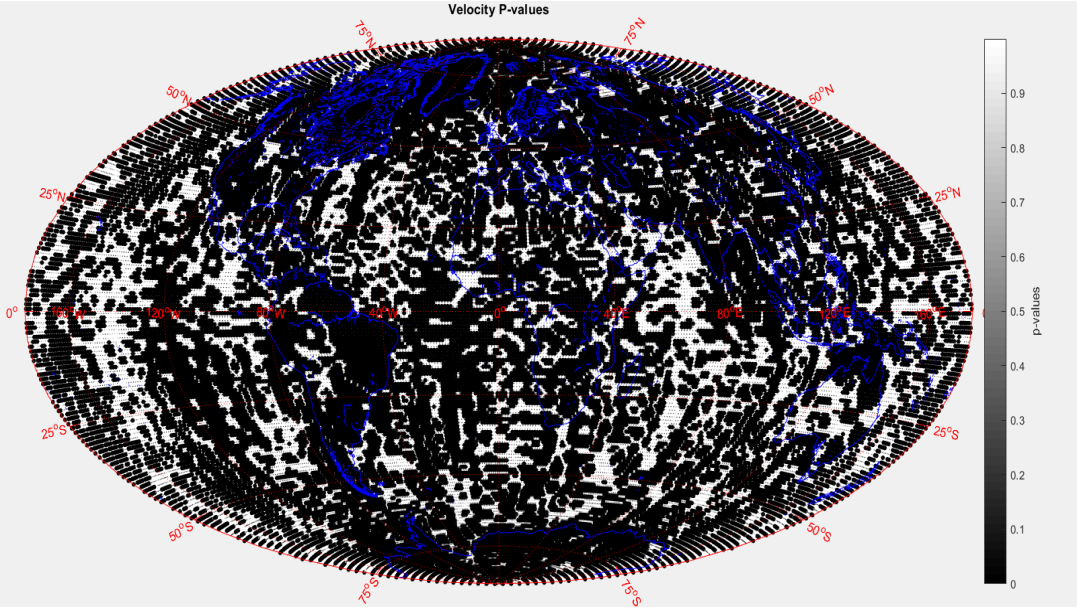

Figure 11: Global analysis - P-values for the velocity parameters

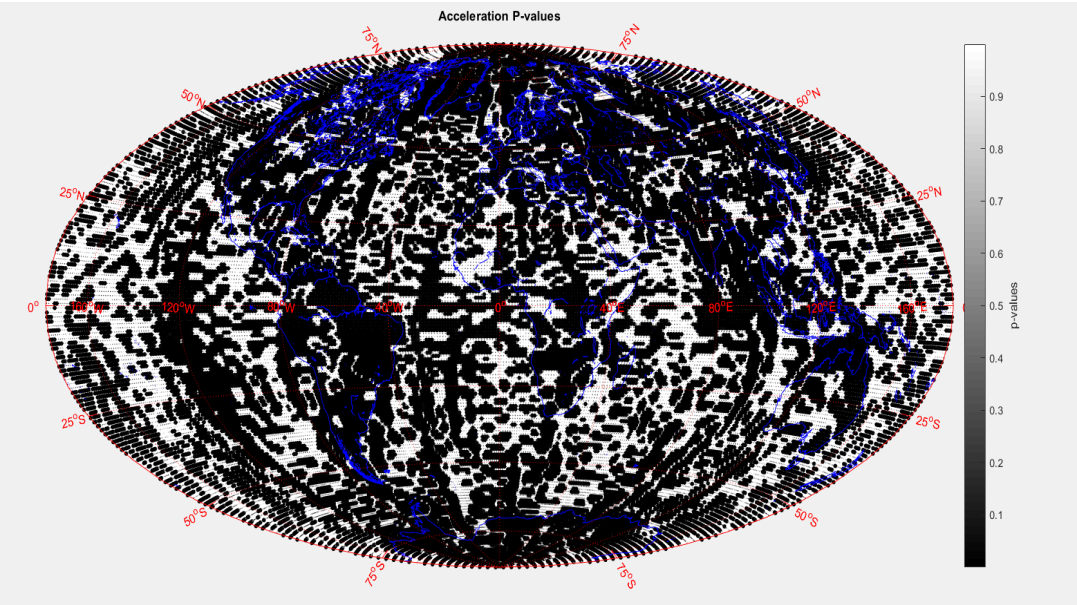

Figure 12: Global analysis - P-values for the acceleration parameters

As expected, there is statistical significance ($p - value < 0.05$) in all the "areas of interest", i.e., the areas containing large amounts of change over time in [EWH] values, for example, the Amazon rainforest, Greenland, West Antarctica, and others.

Accuracy of the model, Root-Mean-Square Error (RMSE):

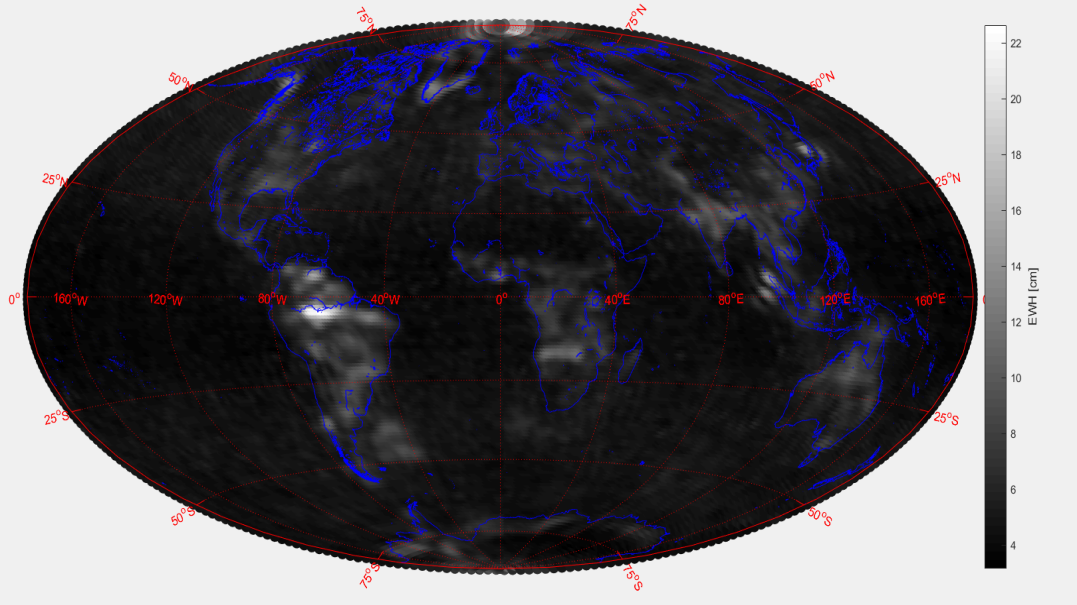

Figure 13: Global analysis - Root-Mean-Square Error (RMSE) for the regression model

The RMSE explains how good the model is, by measuring the standard deviations of the residuals (residuals being the deviation of each data point from the regression line of the best line fit). It is expected to observe higher values of RMSE in the areas of more substantial change in regards to the EWH-values.
In this model, a deviation of up to a bit more than 22 [cm] in the Amazon rainforest, and slightly less in the areas of Greenland and Antarctica, can be seen.
This means that the model is not as good at predicting the model parameters, such as the velocities and accelerations, of the [EWH] in the Amazon than it is in Greenland and Antarctica, for example. Considering the highly oscillating nature of the water distribution in the Amazon rainforest, this is expected.

4.1.3 The annual oscillation of water

The amount of water in different geographical areas on the globe oscillates. Depending on the location, this can be a very significant oscillation, like the one in the Amazon rainforest, where there is an annual cycle of dry and wet periods, the latter of which is characterized by heavy rainfalls (Carol Rasmussen 2017). This oscillation is expressed as a sinusoidal motion, where the amplitude explains the magnitude of the oscillation, and the phase explains during which month of the year the peak of the rainy season hits. Drawing a plot of the different phases on a world map, one may visualize when the rainy season peaks in different parts of the world:

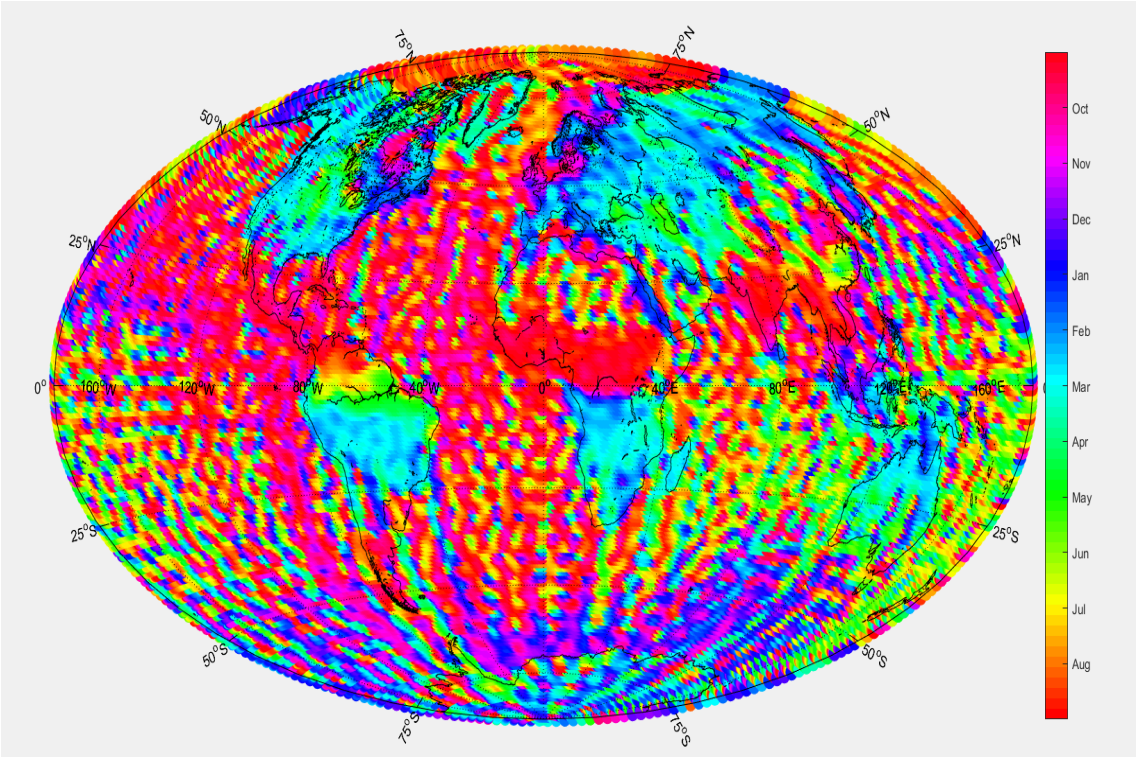

Figure 14: Colorcoded onset of the rainy seasons in different parts of the globe

Looking at figure 14 above, it is a very colorful and noiseful figure. Every single grid point has its own phase, since all grid points have some oscillation of wet and dry periods, even though some of these are miniscule. To account for this problem, the phase and amplitude constants can be put into an HSV-color model [Hue,Saturation,Value] instead of an RGB [Red, Green, Blue] color model. A hand-drawn illustration of the relationship between the RGB and HSV color models can be seen in figure 15, where the [H,S,V]-parameters are denoted by the colors Blue, Red and Black, respectively, and the RGB parameters are drawn in gray.
The RGB color model has 256 different values in each axis of Red, Green and Blue, meaning that it has $256^3 = 16.8$ million different color combinations. In the HSV color model however, the Saturation and Value parameters only takes values in the interval of [0,1] (which is equivalent to a range between 0 and 100 %), while the Hue parameter only takes angle values in degrees in the interval of [0°, 360°]

Hue:
The **Hue** parameter is a circular color scale, which determines the color to be expressed. The different possible colors are similar to the colors that RGB can express (Red, Green, Blue or a combination of those 3 parameters).
Saturation:
The **Saturation** parameter can be seen as the "radius" of the circular color scale. It can take values between 0 and 1. When the value of Saturation approximates 0, the picture will have no color saturation and become gray. The shade of gray depends on the Value parameter. When the value of Saturation approximates 1 however, it approximates the full "richness" of whichever color is determined by the Hue parameter, unless the *value* parameter ap-

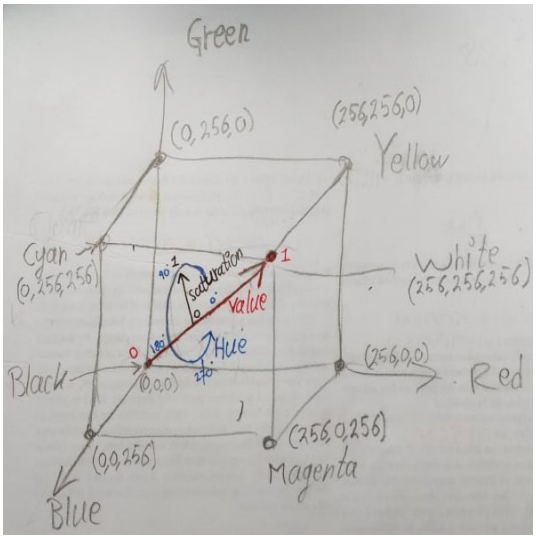

Figure 15: HSV2RGB sketch showing the relationship between the HSV color model and the RGB color model

proximates 0.
Value:
The Value (or Intensity) parameter, which also only takes values between 0 and 1, denotes the interval between black and white. Thus, when the Value parameter approximates 0, the color approximates black, no matter what value Hue and Saturation have. Moreover, when the Value parameter approximates 1, the color approximates whichever color is chosen by the Hue and Saturation values, in its full intensity. Thus, if Saturation were close to 0, the color would become white. However, if Saturation were close to 1, the color would become whatever Hue has determined it to be.

Using an inbuilt function in Matlab named HSV2RGB, the phase, which is a circular color scale, can be input as the Hue parameter and the amplitude of the oscillation can be input as the Value parameter. Saturation is constantly set to 1.
This way, each grid point is shown relative to its amplitude. This means that all points with a low amplitude, for example, points in the ocean, is shown as black while the more "interesting" areas are shown in their respective colors. The result is illustrated in figure 16 below:

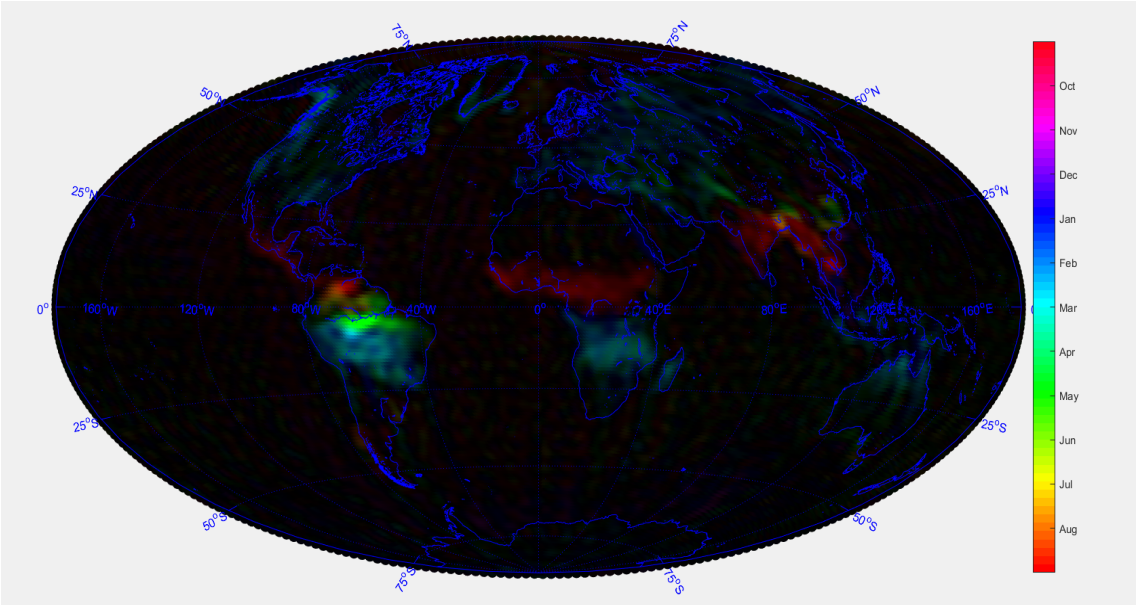

Figure 16: Global analysis - HSV2RGB amplitude-corrected phase plot: Colorcoded onset of the rainy periods in different parts of the globe. Only regions with a high amplitude annual oscillation are seen clearly

As can be seen, the areas with a high amplitude oscillation is the most visible, which is mostly the tropical rainforest areas of Amazon, Central Africa and some parts of south-eastern Asia.

The most significant principal components are plotted onto a world map, and their corresponding eigenvectors are plotted separately as a time series. The scree-plot can be seen illustrated below in figure 17.

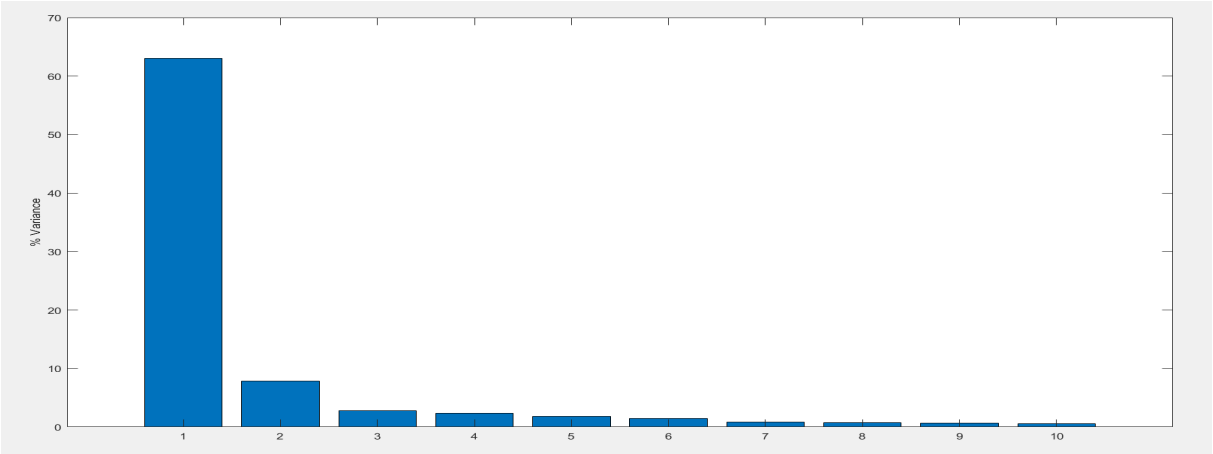

Figure 17: The scree plot belonging to the global principal component analysis

4.1.4 Global Principal Component 1 and its eigenvector

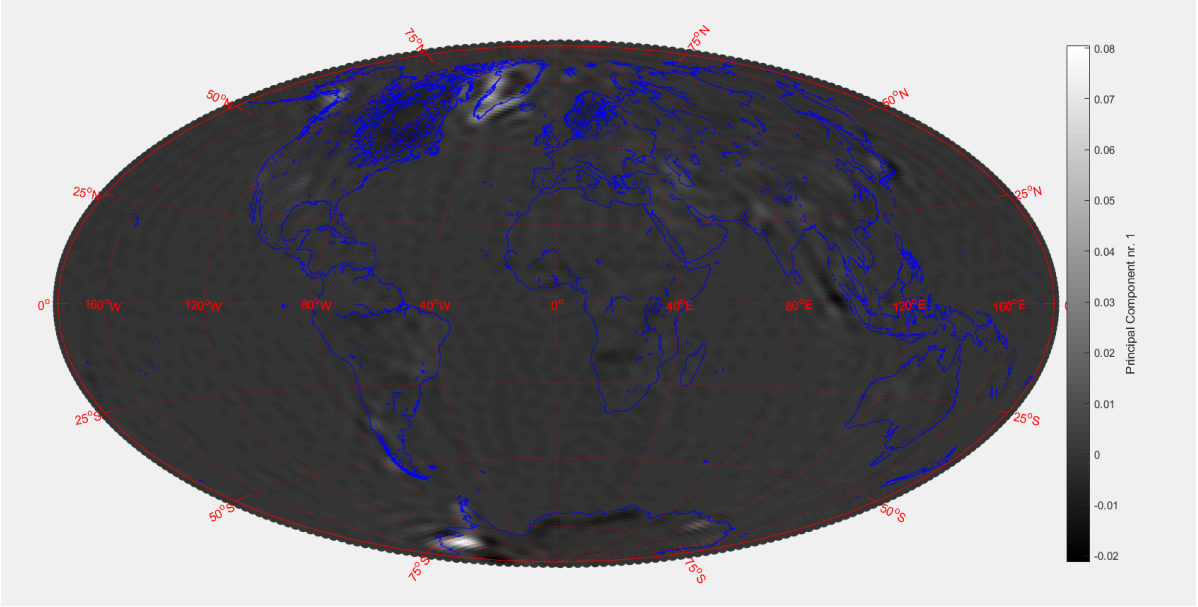

Figure 18: Global analysis - Principal component nr. 1

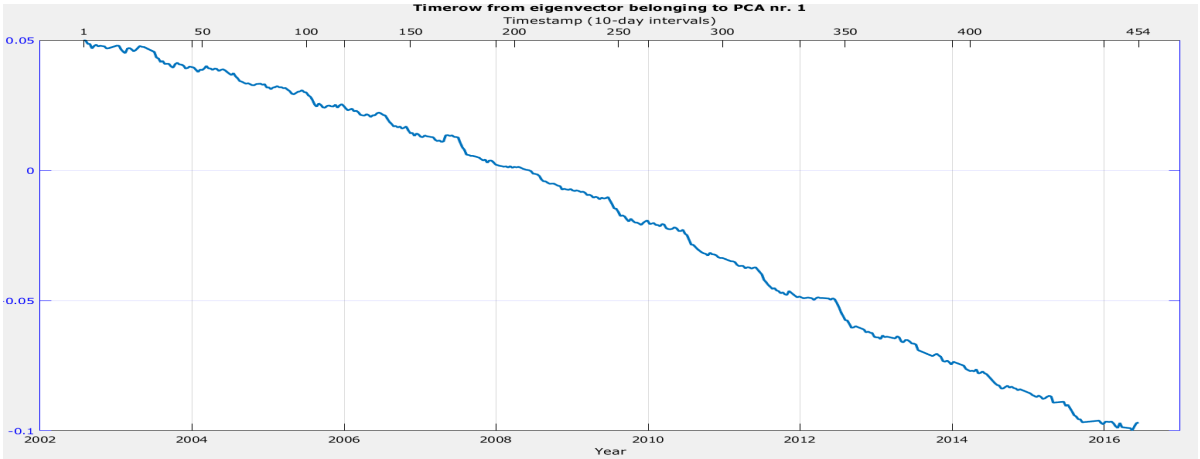

Figure 19: Global analysis - Eigenvector nr. 1

As seen illustrated above on figure 18 and figure 19, the largest amount of variance, (63%), in the dataset comes from the ice melt-off in the Arctic, most prominently in Greenland, Western

Antarctica and Alaska. The values on the y-axis can be interpreted as "weights" of the variance of each point. The sign of the weights is arbitrary, but the decreasing trend of the eigenvector in figure 19 is not. What the eigenvector likely explains is that the ice is melting, or that the amount of "mass" in these areas is falling (due to ice-melt off). Also, it can be seen that it is not an entirely linear decrease, but an accelerating one, as the slope gets more and more steep towards the last time periods. If one compares this decreasing trend with the velocity and acceleration estimates in figure 9 and 10, this seems like a plausible assessment.

Interestingly, the slope changes direction and begins moving upwards at around 450, but this is not necessarily meaningful, since the last GRACE data taken in 2016 was very noiseful, and the GRACE satellites operated under very poor circumstances in this period, due to them flying far past their supposed lifetimes.

4.1.5 Global Principal Component 2 and its eigenvector

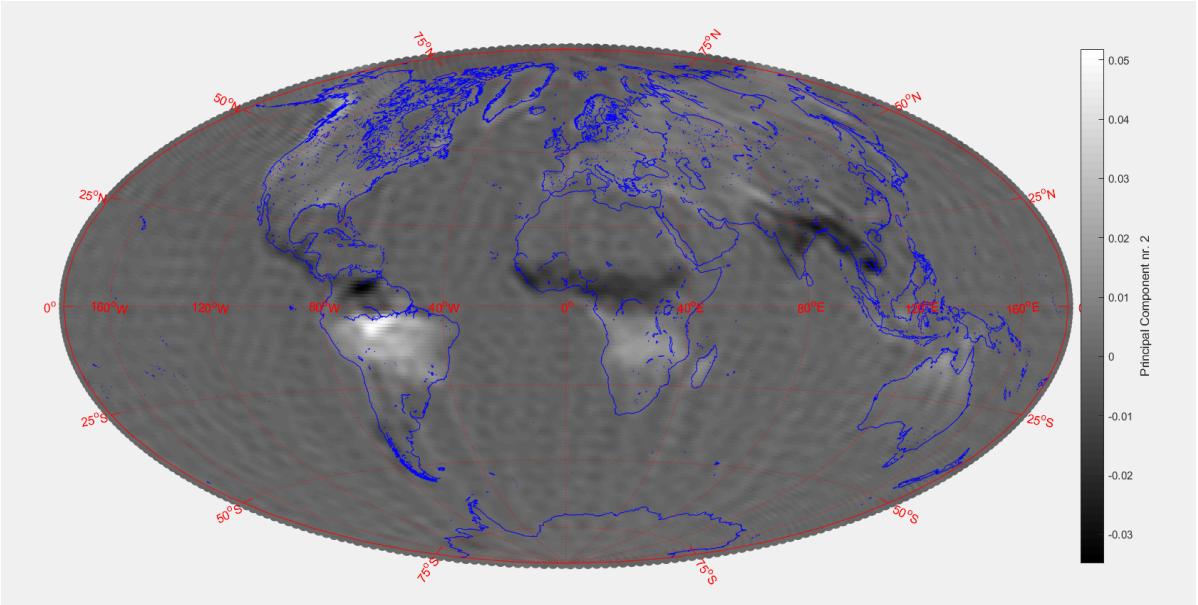

Figure 20: Global analysis - Principal component nr. 2

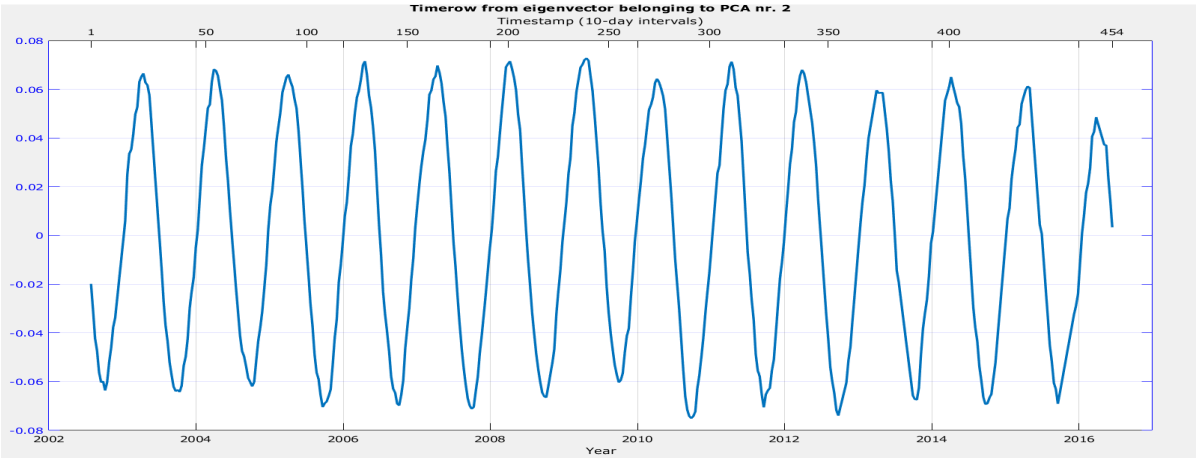

Figure 21: Global analysis - Eigenvector nr. 2

This principal component, which accounts for 7.87% of the total variance, expresses the oscillating masses of water in the tropical rainforests of the Earth. These oscillations are especially large in the Amazon Rainforest, which is the largest rainforest in the world.

On its accompanying eigenvector in figure 21, it can be seen how the masses of water oscillates over time. Interestingly, it seems to oscillate a bit less towards the end period, but this could also be due to the GRACE satellites operating under poor circumstances due to them still being in service so far beyond their intended lifetimes.

4.1.6 Global Principal Component 3 and its eigenvector

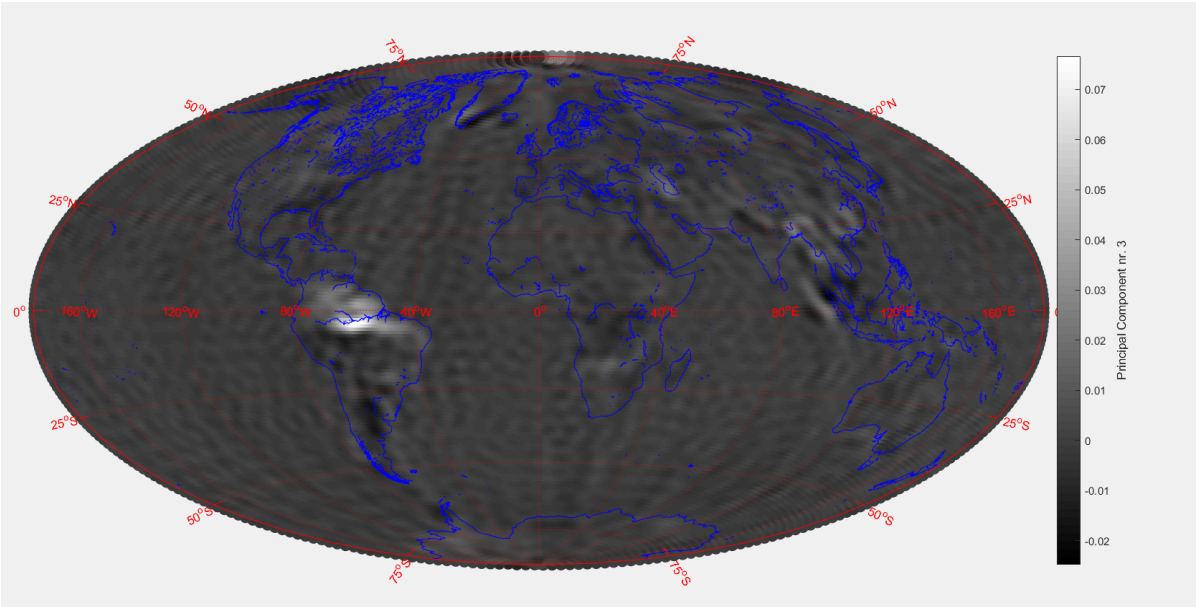

Figure 22: Global analysis - Principal component nr. 3

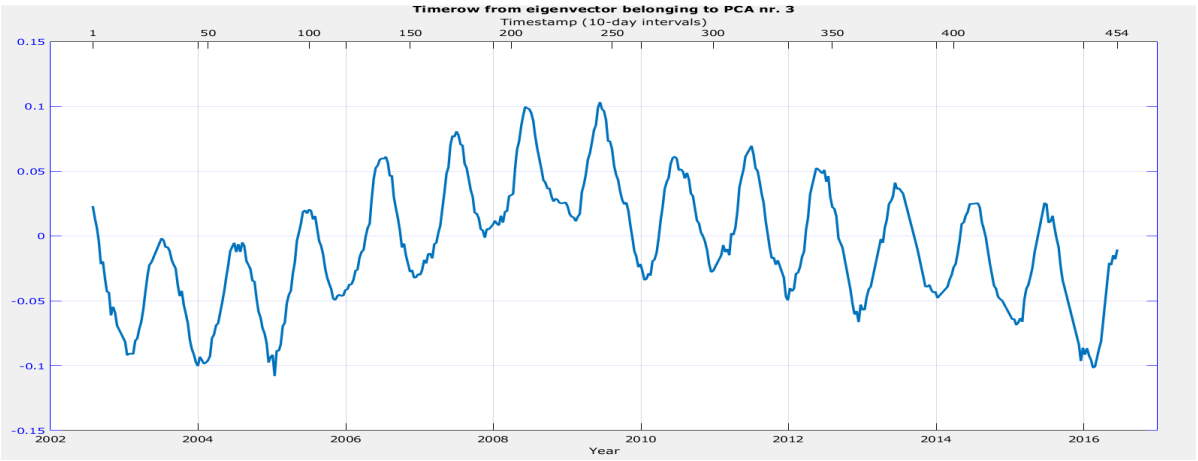

Figure 23: Global analysis - Eigenvector nr. 3

This principal component accounts for only 2.84% of the total variance, so it is becoming increasingly difficult to interpret the factors behind it.
Interestingly, an 11-year cycle can be seen for this eigenvector and its principal component. Moreover, the most significant values are still observed in the Amazon Rainforest.
One could argue that this principal component explains the varying masses of water due to the activity in the sun since solar activity and solar cycles also run through an 11-year period. However, this might be a fallacy, since solar activities only affect the magnetic field around the Earth, and not necessarily the annual oscillation of water in the rain forests, at least not enough to see it so clearly on the principal component.

Another factor that could explain the third principal component is the PDO (Pacific Decadal Oscillation). The PDO features warm or cool surface waters in the North Pacific

Ocean, up to about 20^o N. It changes between "warm" (positive) and "cold" (negative) phases. During a cold phase, the west Pacific warms up to 0.5^oC, and a portion of the eastern part of the Pacific cools. During a warm phase, the opposite phenomenon occurs.
The PDO oscillation is "quasi-periodic", and each phase has a duration of about 20-30 years. Unlike the ENSO (El *Ñino* Southern Oscillation), which is a single physical mode of oceanographic variability, the PDO phenomenon is a cause of multiple influences, such as the ENSO, atmospheric variability in the extratropics, and the North Pacific Ocean gyre. (Earths Climate System) This 'vibration' of the oceans and ocean heights could be the explaining factor behind what is seen in the third principal component. However, this is merely speculation. The data and calculations needed to pinpoint the explaining factor for the third principal component is beyond the scope of this project, so nothing is stated with certainty here.

It is easy to see that when principal components are plotted in this way, all the unnecessary noise in the data is filtered away (such as the noise in the ocean). An illustration of this noise can, for example, be seen in the 7th. principal component:

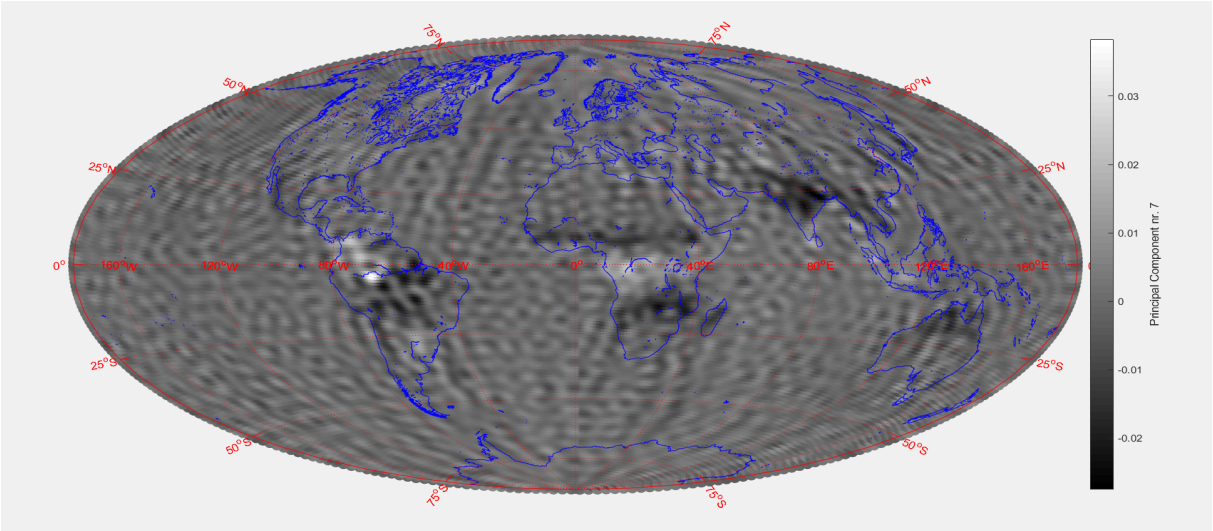

Figure 24: Global analysis - Principal component nr. 7 example

Thus, by just taking the 2-3 largest principal components and plotting them, it is possible to explain everything that's happening in the dataset, without the disturbance of the noise, and thereby to obtain a better and more accurate illustration of the distribution of mass on the globe.

4.2 Regional analysis

Now that an estimate of how the mass is distributed globally over time has been made, it would be interesting to zoom into smaller regional areas and do a new analysis of these places. For example, what is happening in Greenland and Antarctica? How does the flow of water oscillate over time in the Amazon Rainforest? And how does the water dry out or evaporate in the Caspian Sea? By making a mask and analyzing the data of only these chosen regions, all the noise from other places of the world, which could disturb the signal, are filtered away.

In Matlab, it is possible to gain information about these regional areas by drawing a "mask" of the area of interest. This area is drawn by hand as a polygon using the Matlab function **Roipoly**, and the user can then freely determine the size and shape of the area of interest. Then, the mask is extracted consisting of a new matrix of the latitude and longitude vectors of interest, with their corresponding [EWH]-values. The algorithm for creating such a mask is elaborated in section 3.11.

There are different geographical areas on the globe that are more interesting to examine than others, of course. However, GRACE is capable of picking up on many different factors, not

just the melting of ice. For example, it is one of the most precise instruments in the world for monitoring how the worlds water landscape is changing in response to the human influence upon it. A broad term of the essential components of Earths water landscape is called the Terrestrial Water Storage (TWS). It consists of the following 5 dynamic components:

1. Groundwater
2. Soil moisture
3. Surface waters
4. Snow
5. Ice

The GRACE satellites are capable of monitoring these 5 components with unprecedented accuracy. A recently published scientific paper identified the regions where the TWS appears to be trending below its previous range of values, primarily due to ice-calving and melt-off of glaciers and ice sheets and locations where the groundwater is decreasing at an unsustainable rate (Rodell 2018). The paper, published in 2018 by M. Rodell, examined the Terrestrial Water Storage trends and changes more closely, based on data from the GRACE satellites. Figure 25 below, which was published in the paper, illustrates the different TWS trends and masks in different places on Earth, and also the likely cause of these effects:

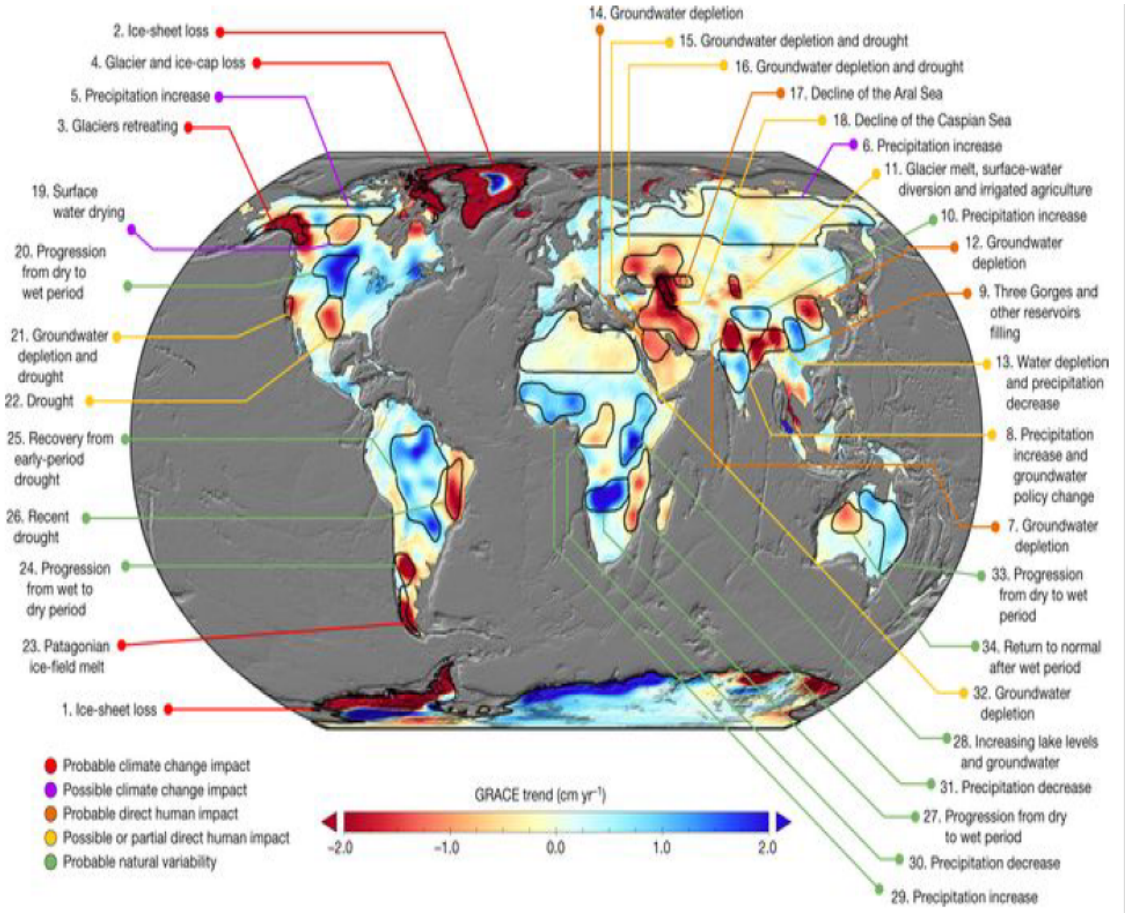

Figure 25: Annotated map of Terrestrial Water Storage trends in TWS (in centimetres per year) obtained on the basis of GRACE observations from April 2002 to March 2016. The cause of the trend in each outlined study region is briefly explained and colour-coded by category. Source: M. Rodell, et.al. 2018. Emerging trends in global freshwater availability. Nature.

Using figure 25 for inspiration, a mask was created around the following regions for a closer analysis:

1. Greenland mask for examining ice loss.
2. West Antarctica for examining ice loss.
3. Alaska for examining ice loss.
4. Amazon Rainforest for examining annually oscillating masses of water.
5. Tibetan-Plateau for examining loss of Terrestrial Water Storage (TWS).
6. Caspian Sea for examining the decline of the sea due to evaporation and river runoff.
7. Sumatra, Indonesia and Fukushima, Japan for examining earthquakes.

Authors note: A short introduction is given for each region, explaining why I chose each region instead of so many others.

4.2.1 Greenland mask

Authors note: Over the years, Greenland has been the subject of much debate, study, and controversy. Innumerous scientific papers have been released on the subject of Greenlands melting ice sheets and changing landscape, and what consequences this might imply for our future. Therefore, the region of Greenland is an obvious first choice for an analysis, in my view.

As can be seen in figure 25, Greenland is an area where the Terrestrial Water Storage is declining at a fast rate each year. According to the figure, it is plausible that climate change impact is a probable factor for this.

By using the roipoly tool for creating masks (see section 3.11), an area around Greenland is extracted (see D.1 for the chosen mask region). The size of the mask is now [1372 x 3 x 454], with longitudes spanning between 78.5000**W** to 8.5000**W** and latitudes spanning between 56.5000**N** to 87.5000**N**.

As mentioned earlier, the GRACE satellites measure with a resolution of 400 [km], which can give large problems when measuring at a far northern/southern extent. The reason for this is that the longitude points lie closer and closer to each other, due to the curvature of the Earth. This means that the data points on Greenland on the same longitude parallel line (constant latitude) lies very close to each other (61.44 [km] at 56.5**N** and just 4.86 [km] at 87.5**N**). As the latitude approaches 90 degrees north or south, this distance approximates 0 (see also section 2.5 for further elaboration).

Hence, when plotting and calculating the data, it is critical to account for these latitude-dependant areas of the grid-points. A way to do this visually is by defining a vector of "bubble sizes" for the scatterplot, which decreases as the latitude moves further northward/southward. Thus, each bubble is multiplied by cos(latitude), to account for the falling longitude distance (distance between latitudes is more or less constant between the equator and the poles). When calculating the amount of ice lost in each gridpoint, this method becomes especially important (see section 3.10 for the equation and approach on how to do this).

There is still the problem of the 400 [km] resolution, however, one that can't be avoided. For example, this is also the reason why there seems to be accelerating EWH values out in the ocean, outside of Greenlands coastline. However, in truth, these values come from the measured grid points right on Greenland's coast, their measurement resolution just goes 200 km out into the ocean. This is why it is crucial to create the mask with the polygon reaching

(approximately) 200 kilometers outside of Greenland's coastline, to account for this resolution problem, and not risk losing data.

After the mask is created, the complete analysis covered in the method section is created for the chosen area.

First off, the Velocity and Acceleration parameters are estimated:

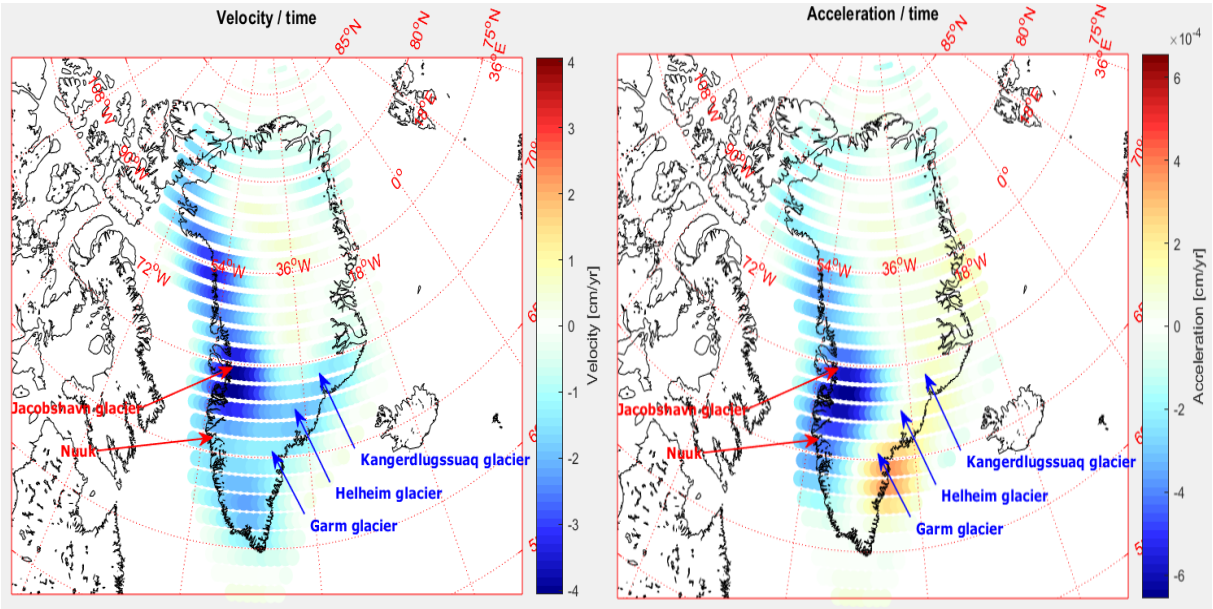

Figure 26: Greenland mask - Velocity (as of 15th June, 2016) and acceleration parameters

Here, a positive acceleration in south-eastern Greenland is observed, indicating that the tendency of ice melt-off in this region is decreasing, while there is a significant negative acceleration in south-western Greenland, indicating that the tendency of ice melt-off in this region is increasing. Also, looking at the velocity values (as of 15th June 2016), it can be seen that while there still is a negative velocity of ice melt-off in south-eastern Greenland, it is miniscule compared to that of south-western Greenland.

Following this, a singular value decomposition and principal component analysis were done for the area, to try and relate to the findings of the velocity and acceleration parameters.

Greenland mask - Scree plot:

First, a scree plot is created. It is seen that by far the largest amount of variance is accounted for in the first principal component (accounting for 95.7% of the total variance). This most likely expresses the ice-melt off trend of Greenland as a whole.

The second principal component is also interesting, even though it only accounts for 1.2% of the total variance. It likely explains the change of melt-off in the different areas, especially south-eastern Greenland.

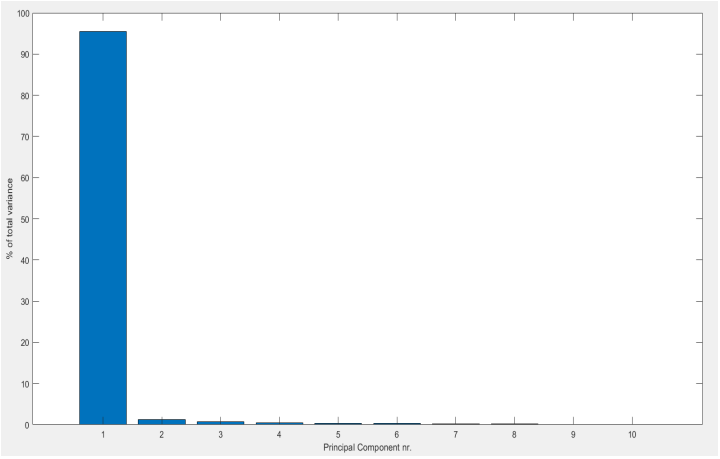

Figure 27: Greenland mask - Screeplot from the principal component analysis

Greenland mask - principal component nr. 1:

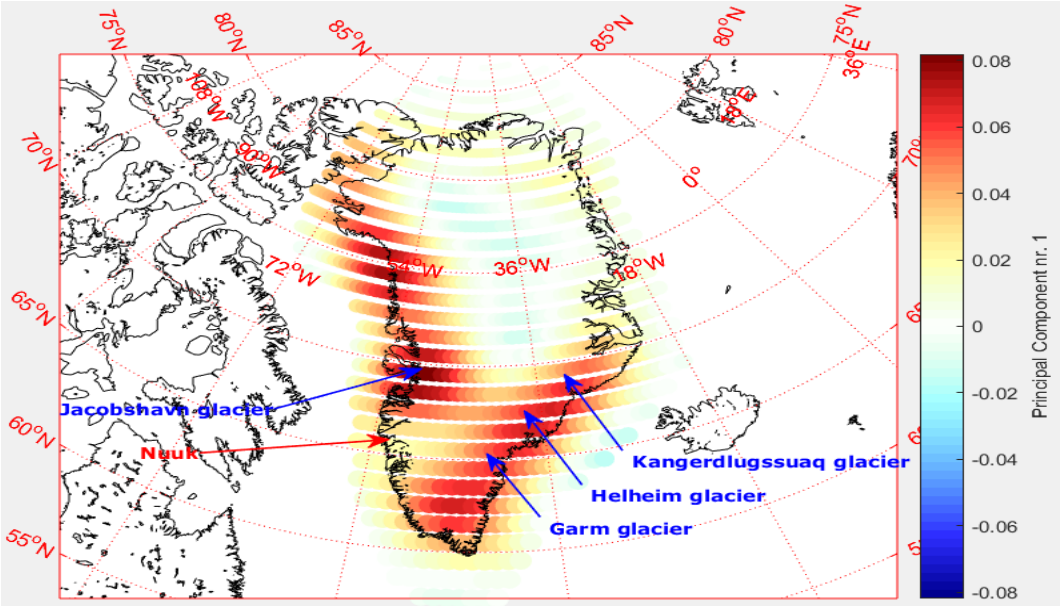

Figure 28: Greenland mask - Principal component nr. 1

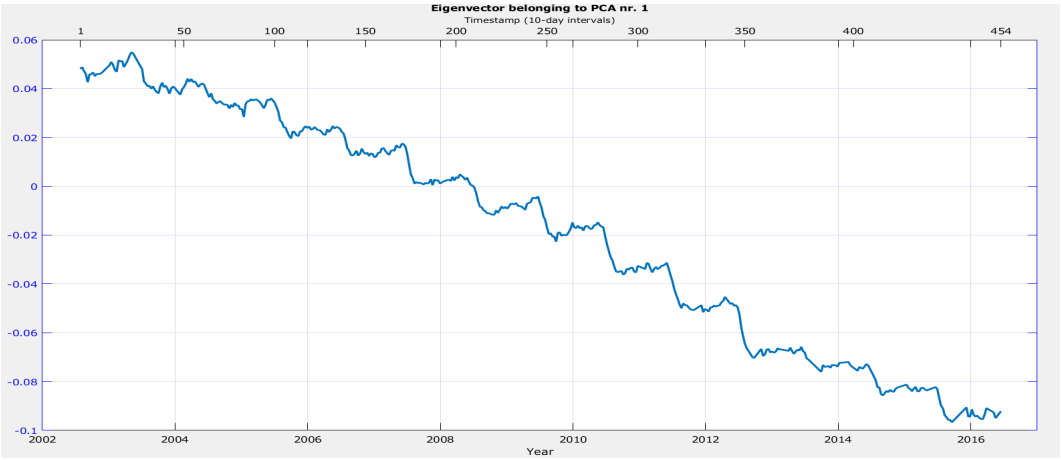

Figure 29: Greenland mask - Eigenvector belonging to principal component nr. 1

Comparing the spatial pattern of PC1 (principal component nr. 1) with its eigenvector, it likely shows the ice melt-off trend happening around Greenland, especially around south-western and south-eastern Greenland. The trend of the eigenvector belonging to PC1 could explain that there is a substantial melt-off of ice in all areas and that this melt-off is accelerating.

To confirm these assumptions, it can be related back to the estimates of velocity and acceleration, seen in figure 26. Here a negative velocity is seen in the same geographic areas as the ones observed in the spatial pattern of PC1, and the magnitude of the signal of these different areas also fits nicely with the first principal component. Therefore, it seems plausible that PC1 explains the ice-melt off trend around Greenland's coastlines.

Greenland mask - principal component nr. 2:

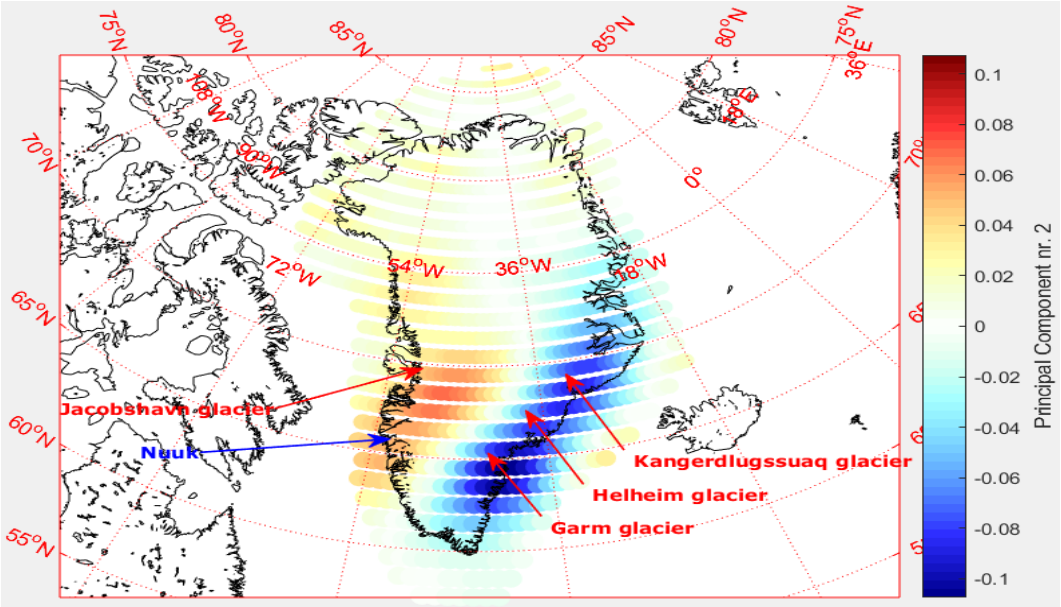

Figure 30: Greenland mask - Principal component nr. 2

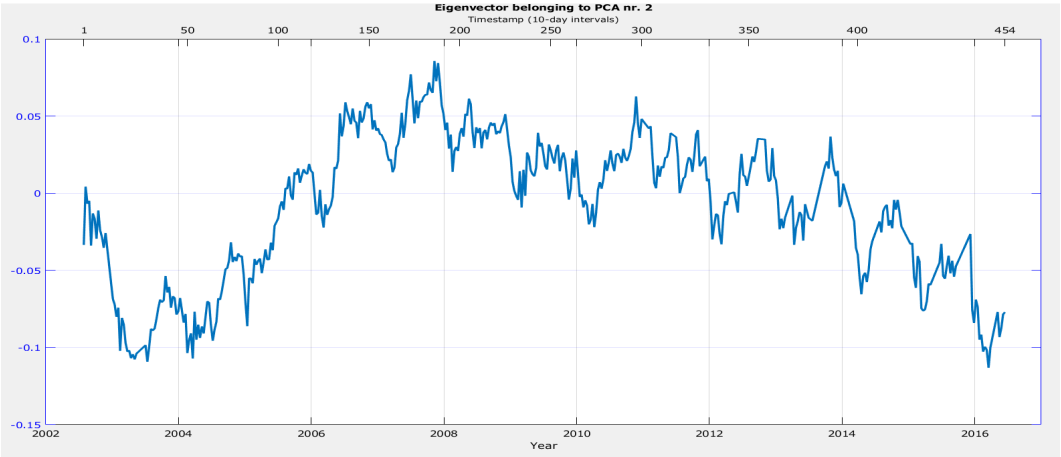

Figure 31: Greenland mask - Eigenvector belonging to principal component nr. 2

Comparing the spatial pattern of principal component nr. 2 with its eigenvector, here a clear contrast is observed between the south-east coast and south-west coast of Greenland. The south-western coast has large positive values in the spatial pattern, while the south-eastern coast has large negative values. Also, comparing it with eigenvector 2, there seems to be a shift of weights happening around 2005, where it increases and then falls back down around 2011.

What this could explain is a change in the velocity estimates of the different areas of Greenland. To increase the insight of this phenomenon, it is compared to the physical interpretations seen in the velocity and acceleration estimates in figure 26.

Here a positive acceleration is observed in south-eastern Greenland, and a negative acceleration is observed in south-western Greenland. This supports the claim that principal component nr. 2 explains a shift in acceleration and velocity that is happening over time, and that the tendency to ice melt-off in south-eastern Greenland is decreasing, while it is increasing in south-western Greenland.

Another thing to note is that the spatial area in south-western Greenland (south of the Disco fjord), which has an accelerating ice melt-off rate, was not visible at all in the first principal component. This could mean that it was important to also examine the second principal component, despite its somewhat low percentage of the total variance, because it could detect a substantial signal that was completely omitted from the first principal component.

Amount of ice-loss in mask in Gt/yr:
Finally, an estimate of the amount of ice that is melting in Greenland each year is calculated. This is done by summing the total amount of measured EWH in each timestamp (10-day periods) and then subtracting the total amount of EWH in Greenland at the start September by the total amount of EWH at the start of September the following year, to get an estimate of the total change of ice (in gigatons).

However, it is critical to account for the changing area of each grid point, since the area decreases as the latitude increases. To do this, the formula covered in section 3.10 was used to calculate the total amount of mass at each timestamp for the mask.

Following is then an illustration of the total amount of ice loss in Greenland at every year from September 2002 to September 2015 (2016 is excluded, since data is only available until 15th June 2016):

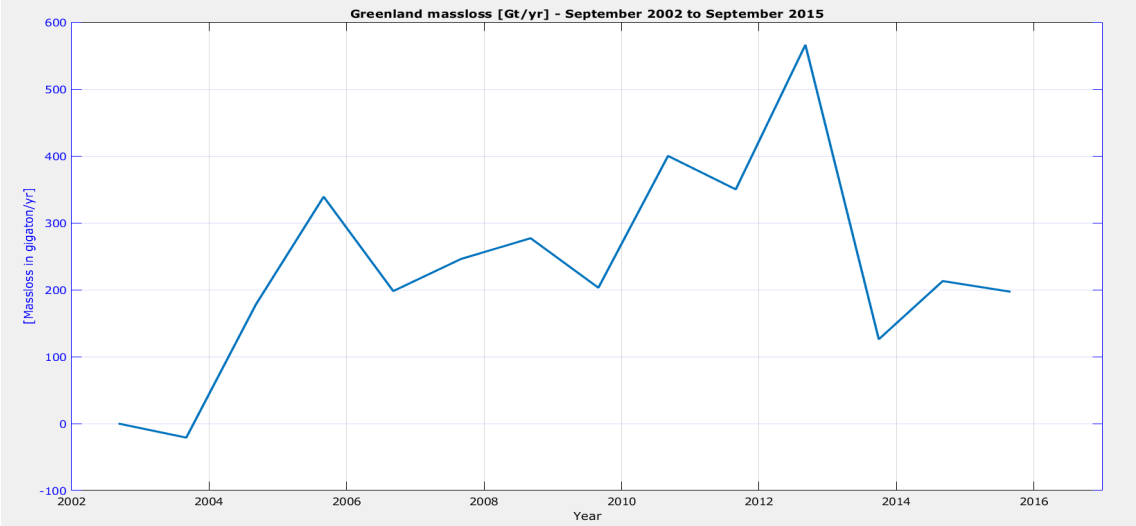

Figure 32: Greenland mask - Ice loss in Gigaton/year from Sep 2002 - Sep 2015

This result is consistent with recent reports of record high ice-loss around 2010 to 2012, and quite low ice-loss during 2013. In addition, the magnitude of the ice melt off also fits that of various scientific papers, such as the paper *Greenland and Antarctica Ice Sheet Mass Changes and Effects on Global Sea Level (2017)* (Forsberg et al. 2017), (Scambos and Koenig 2013).

Finally, it should be noted that there is a small error present here. The EWH data that was used to measure this ice loss is given for different time stamps, and sometimes there are holes in the measurement times. For example, measurements for all of August and almost all of September is missing in 2013. Additionally, the timestamp of each data matrix is not consistently available for the same dates each year, so this might lead to a small error, since there is a deviation of about ± 6 days for the dates of the measurement data in September (except in 2013). But overall, it is a good estimate to gain some overview of what is happening in Greenland in terms of ice loss.

It would also be possible to estimate the ice loss using the regression model, and thus avoid the potential error from the different time stamps. Then, the predicted EWH values is estimated for the 1st September each year, and the predicted ice loss is calculated again, as seen in figure 33:

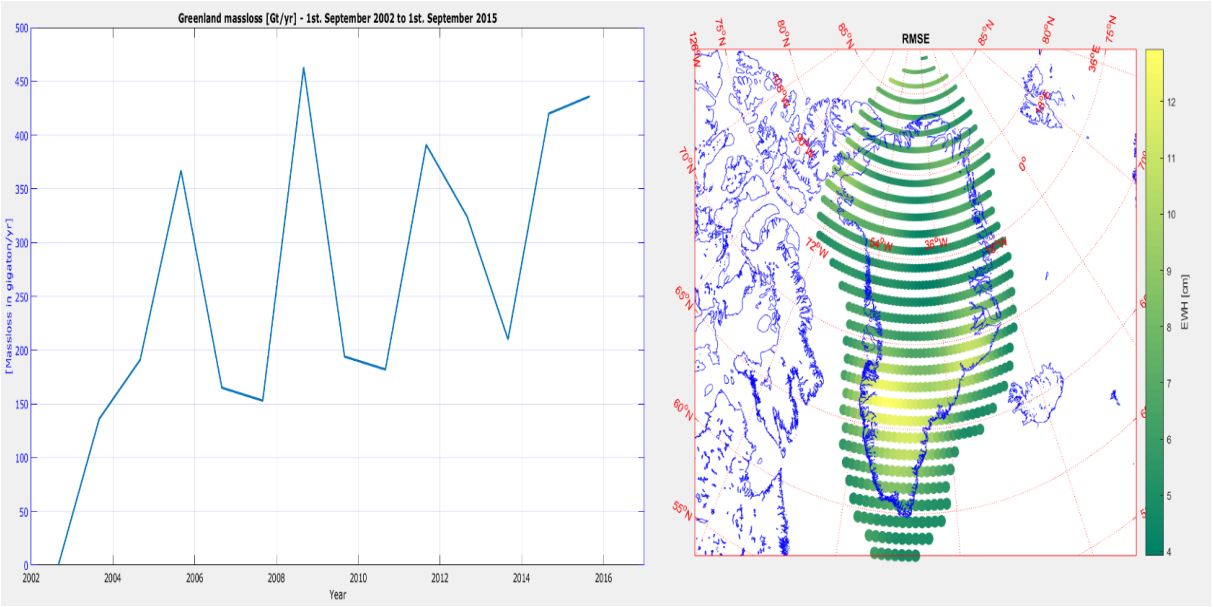

Figure 33: Greenland Iceloss measured with the regression model, compared with its RMSE

As seen above, this estimate is quite different from the first one. Both are more of less consistent with the scale of annual ice loss reported by other scientific studies however, even though the estimate from the model has its largest ice loss around 2007-2008, which is not consistent with the highest iceloss ever being recorded in 2012 (Scambos and Koenig 2013). The explaining factor behind such a large deviation could be the large values of RMSE around Greenland, as can also be seen in figure 33, meaning the model is just not as good at measuring the predicted EWH values in this region. Furthermore, the model is not at all corrected for the Glacial Isostatic Adjustment, which might also lead to a significant error in the measured values.

To see the timestamps and the measurement dates used to calculate the ice loss, please see figure 80 in the Appendix.

4.2.2 Western Antarctica regional analysis

Authors note: When plotting the EWH data worldwide, the most significant rates of change, concerning velocity and acceleration estimates of ice melt-off, is observed in western Antarctica, around Pine Island Bay. That is the main reason I chose this region for closer analysis, to examine the factors behind such a dramatic rate of change.

To examine the region of western Antarctica further, a mask is created around the area as can be seen illustrated in appendix D.2.

The mask extracted in the bottom left of figure 82 has a size of [1209 X 3 X 454].
Its longitude spans from 134.5**W** to 50.5**W**, and its latitude spans from 56.5**S** to 80.5**S**.
The map in the right side of figure 82 in the appendix shows the region of interest, where the yellow polygon marks the mask area.

To improve the insight of what is happening in the region, the velocity and acceleration parameters for the region are calculated:

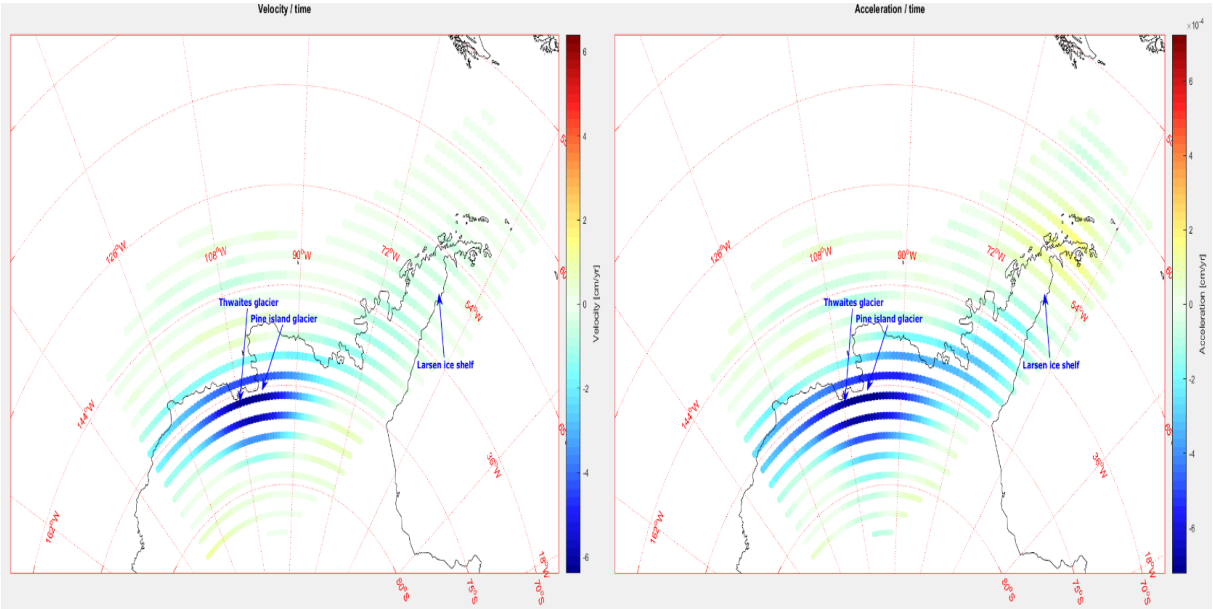

Figure 34: Antarctica mask - Velocity (as of 15. June 2016), and acceleration parameters

As of summer 2016, there still seems to be a significant negative velocity at Pine-Island bay, one that hasn't stopped accelerating. So the tendency of accelerating ice melt-off in western Antarctica seemed to continue for the entirety of the GRACE satellites data collection.

Also very interesting is that it seems like the ice melt-off around the tip of the Antarctic Peninsula (north of Larsen ice shelf) is stopping, since a positive acceleration is measured here. However, this might be a coincidence since almost all of the Larsen B ice-shelf (a 3,250 square kilometers ice-shelf) collapsed in 2002 as one of the largest ice-shelf collapses recorded in modern history, and similarly, a 2,500 square kilometre iceberg calved from the Larsen-C ice shelf in 2017, also one of the largest ice-shelf collapses in modern history. Both of these events are just outside of the measurement period for this data. If these events had been included in the data, the acceleration estimated at the tip of the Antarctic peninsula might have looked entirely different (Lindsey 2002), (Ong and Potenza 2017).

To compare what was found in the velocity and acceleration parameters, a principal component analysis is made. The distribution of the principal components are seen on the scree plot in figure 35:

It is seen that most of the variance is by far accounted for in the first principal component (98% of the total variance), while the second largest principal component accounts for just 0.65% of the total variance.

Following, the principal components are examined more closely:

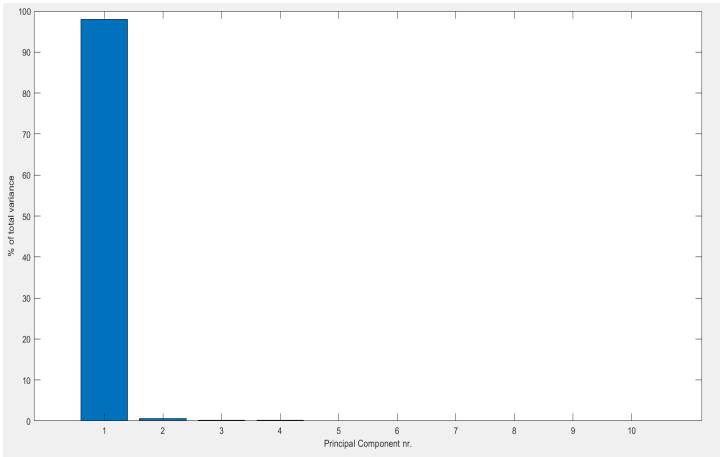

Figure 35: Antarctica mask - Scree plot for the principal component analysis

Antarctica mask - principal component nr. 1:

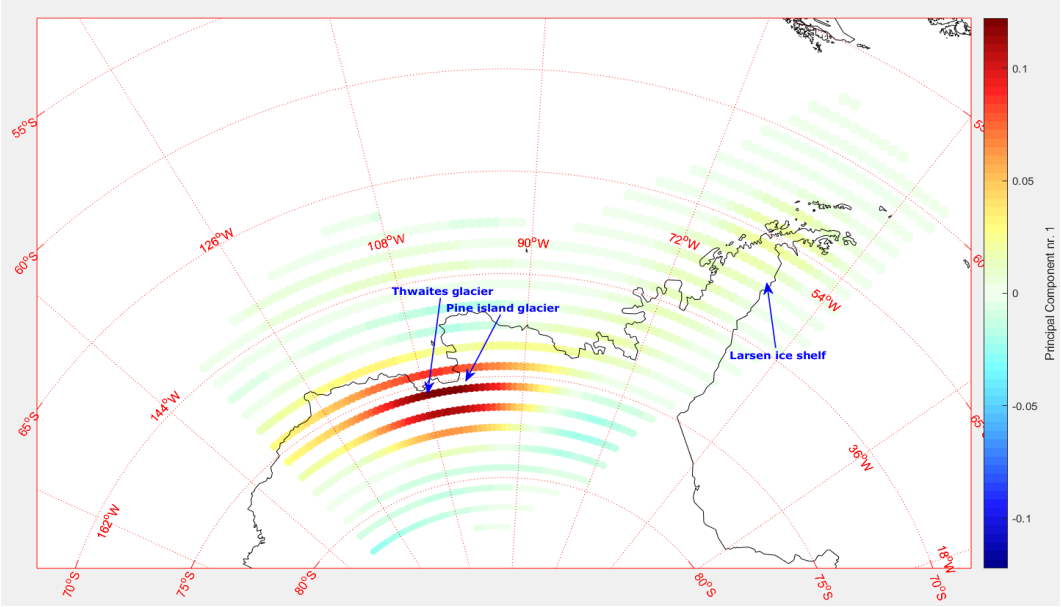

Figure 36: Antarctica mask - Principal component nr. 1

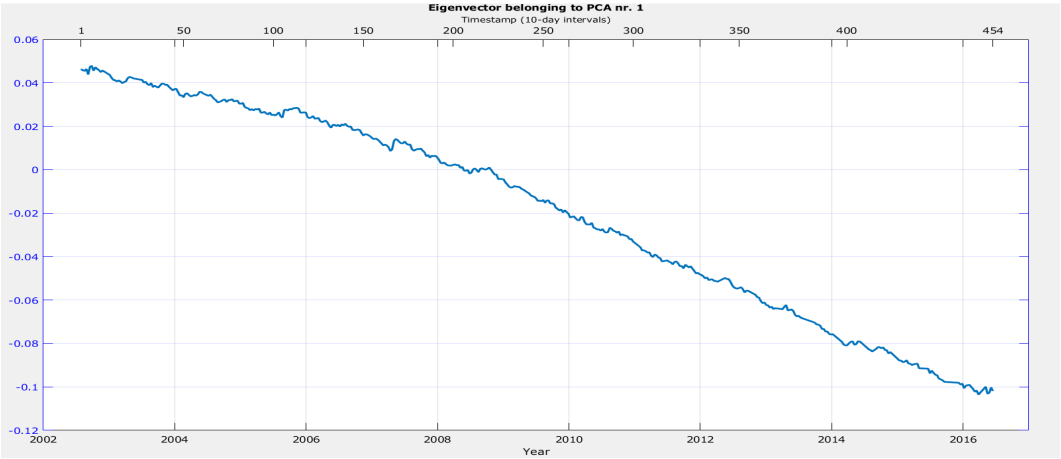

Figure 37: Antarctica mask - Eigenvector belonging to principal component nr. 1

Comparing the spatial pattern of principal component nr. 1 with its eigenvector, a clear trend of decreasing values is observed for the mask area, centered around the area of Pine Island Glacier and Thwaites Glacier. The area with positive values in the spatial pattern seems to correspond to the region that is losing large amounts of ice and having both negative velocity and acceleration, as seen in figure 34. Hence, 98% of the variance, expressed in the first principal component, most likely explains the main ice-loss trend that is happening in Antarctica.

Antarctica mask - principal component nr. 2:

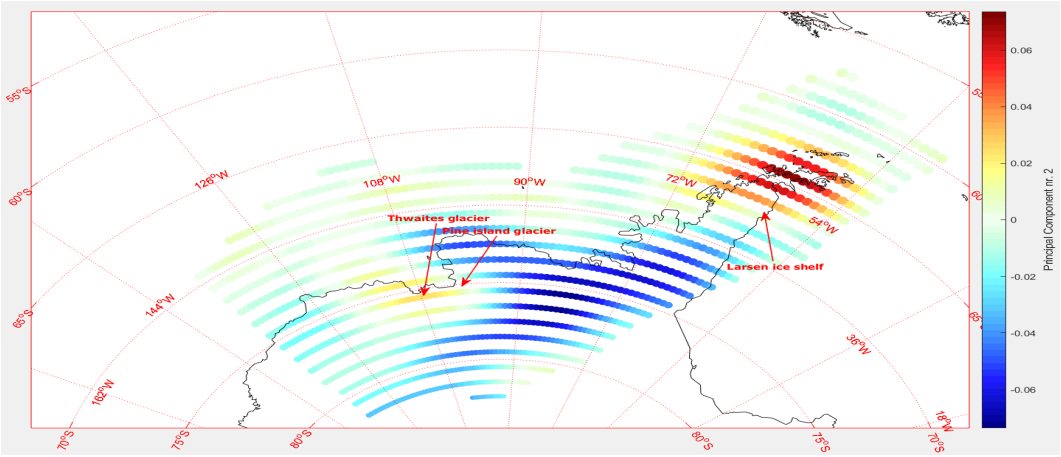

Figure 38: Antarctica mask - Principal component nr. 2

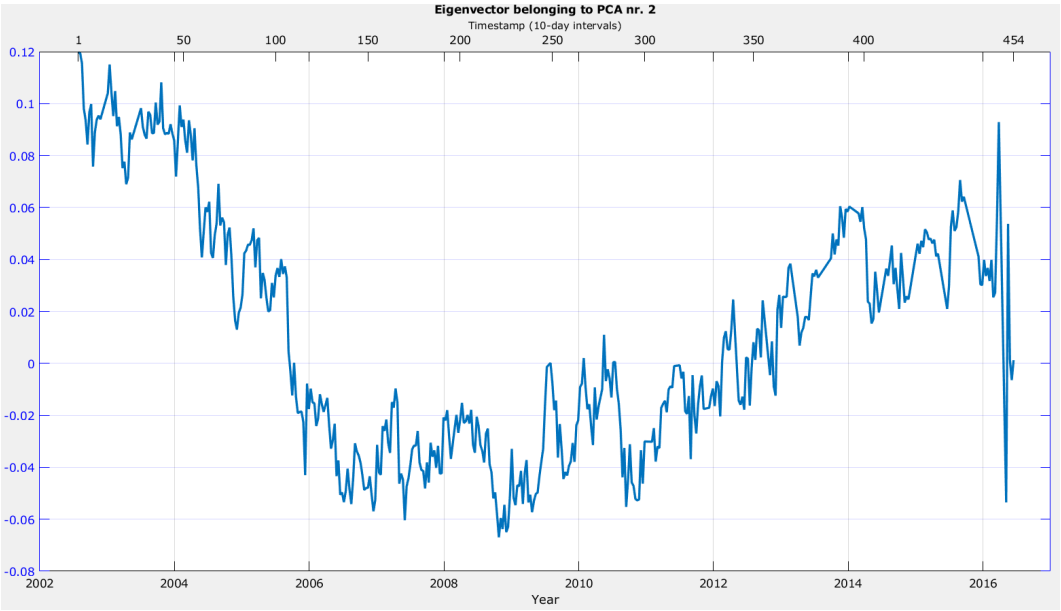

Figure 39: Antarctica mask - Eigenvector belonging to principal component nr. 2

Comparing the spatial pattern of principal component nr. 2 with its eigenvector, a large shift in the magnitude and sign of the weights can be seen, especially between the area of Pine-Island bay area and at the tip of Antarctic Peninsula, and the area of mainland Antarctica. The pattern observed here is similar to what was seen in PC2 of Greenland as well (See 4.2.1), where there was a regional shift, during a particular period (that didn't start around the first timestamp, but later on). What this could mean is that there could be a shift in the acceleration or velocity, that is happening around mid-2004 (seen in the eigenvector). This shift continues until around 2011, where it changes direction again for the remainder of the period.

Unfortunately, not much can be gained from comparing it with the velocity and acceleration estimates in figure 34 since the acceleration here is an estimate for the entire period, and the velocity is an estimate for only the 15th of June, 2016. It could be possible to gain further insight by making a new velocity estimate in the middle of the period, perhaps, but considering the small amount of percentage of the total variance this principal component has, it will hard to conclude anything with certainty here, no matter what.

Antarctica Ice Melt-off

Also very interesting, considering it is an Arctic area with a high amount of ice melt-off, is to examine how much ice it loses each year:

The total amount of mass loss in western Antarctica is measured from March 2003 to March 2016.

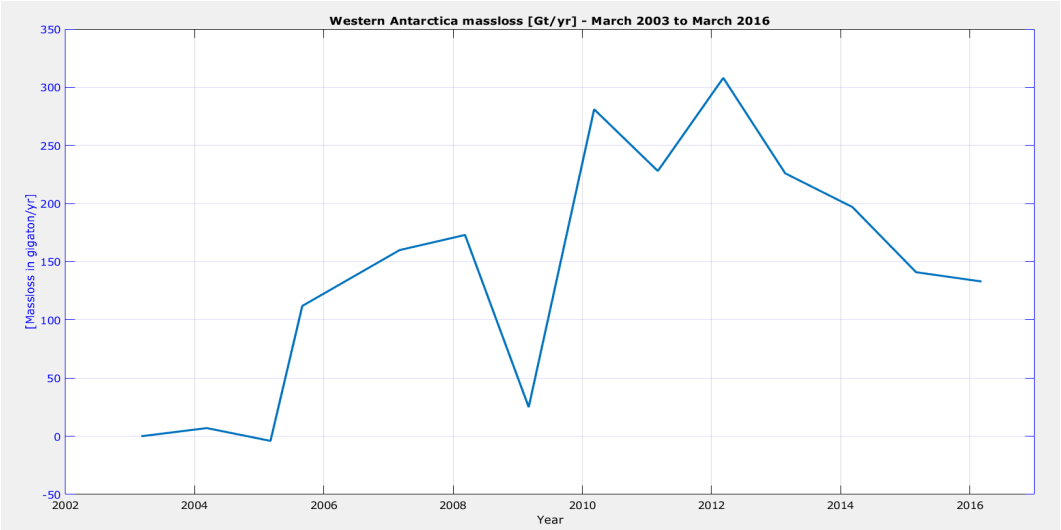

Figure 40: Antarctica mask - Ice melt-off in western Antarctica, 2003-2015

From the graph in figure 40, a significant trend of mass-loss is observed in this area.
However, looking back at figure 25, it can be seen that in eastern Antarctica, it seems to gain mass instead of losing it, from the positive signal observed here. If a new mask was made of all of Antarctica, the ice loss in its entirety could be examined. This might lead to a fuller picture of the total change of mass on the continent:

Ice melt-off in all of Antarctica, 2003-2015
(*The newly chosen mask can be seen in appendix D.2*)

By examining the total ice melt-off of this region, a quite different result can be seen:

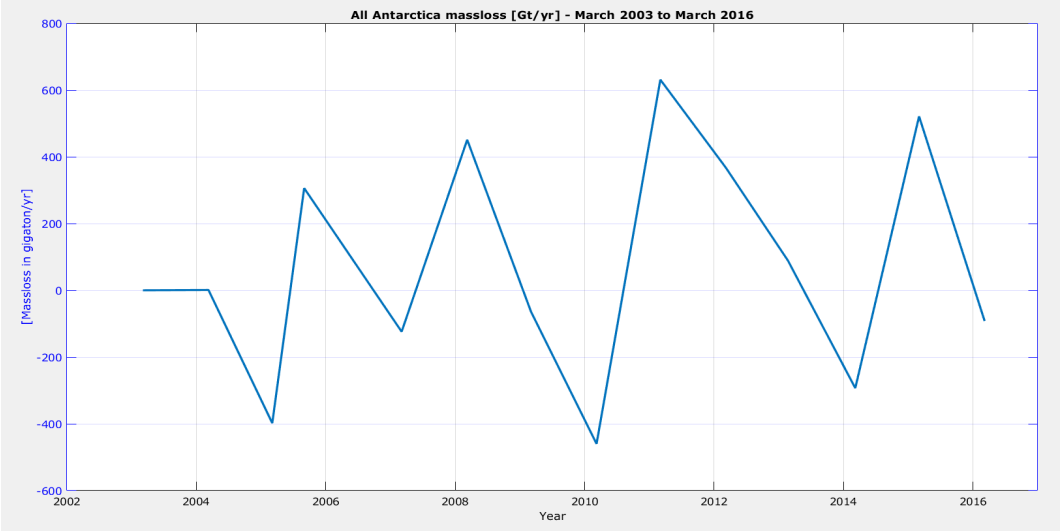

Figure 41: All of Antarctica mask - Total melt-off from March 2003 to March 2016

The total amount of ice lost in western Antarctica seems to be almost evened out by the ice gained in eastern Antarctica.
There still is a net loss of ice, however, as expected. However, this net-loss is much smaller than one might initially think, due to the other factors that come into play. Also, this total estimate fits well with the findings of other reports, which estimated a total mass loss between 80-110 Gt/year for Antarctica (Forsberg et al. 2017).

4.2.3 Western Alaska

Authors note: For a long time now, numerous scientific newspapers have reported on the retreating and melting of glaciers in this region. For example, the paper by M.Rodell published in the Nature science journal (Rodell 2018), pinpointed the cause of the glacier retreating to a probable climate change impact. Being the Arctic area with the third largest signal regarding ice melt-off and rate of change, I chose this region as the final arctic area to study in the regional analysis.
Below can be seen a typical example of the vast change the glaciers in Alaska (and elsewhere) have gone through over the last 100 years, taken from the White Thunder Ridge Glacier in southeastern Alaska.

Figure 42: White Thunder Ridge Glacier, 1941 (left) and 2004 (right).

Creating a mask in similar fashion for this area (which can be seen in appendix D.3), leads to the following data regarding the velocity and acceleration.

Velocity and acceleration estimates:

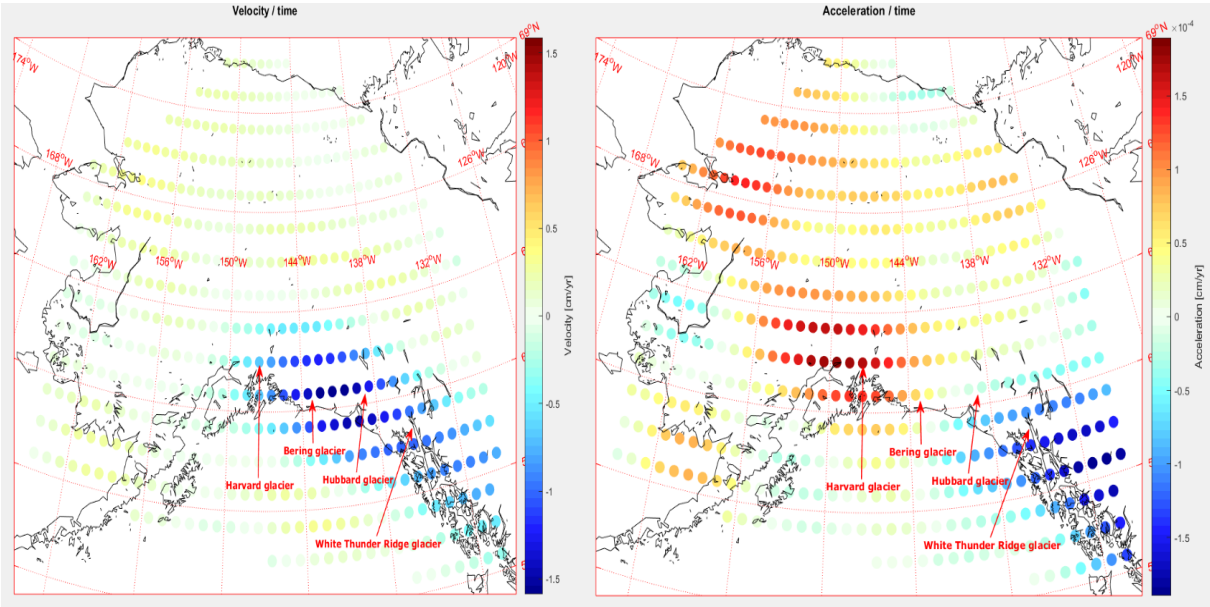

Figure 43: Alaska mask - Velocity (as of 15th June 2016) and acceleration parameters

Here it can be seen that there is a large negative velocity in the summer of 2016, but that it has a positive acceleration, meaning that this ice melt-off tendency is decreasing overall, for

south-central Alaska. In comparison, ice melt-off in south-eastern Alaska seems to be accelerating with a large magnitude but has a smaller negative velocity as of summer 2016. Even though the regression model used in this project cannot be used for prediction past the last time stamp, it can be argued that if this trend continues, climate researchers should keep a closer eye on this area in the years to come.

This can be compared with the eigenvector and spatial pattern of the second principal component, which accounts for about 7% of the total variance:

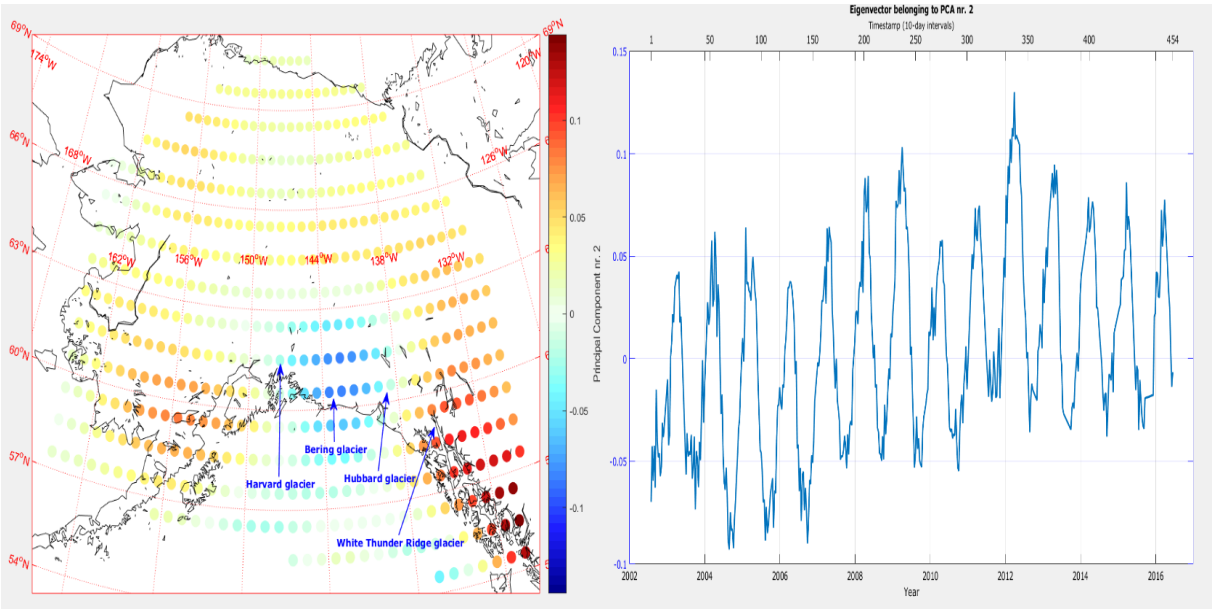

Figure 44: Alaska mask - Principal component nr. 2 and its eigenvector

It looks like this principal component expresses the annual oscillation of water masses. The direction of the eigenvector is arbitrary, but it seems to support what the acceleration and velocity parameters explains, that there is an increase in velocity over time in south-eastern Alaska (around White Thunder Ridge) and a decrease in south-central Alaska (around Bering glacier).

The second principal component also seems to show a change in acceleration or velocity of ice-loss at around 2008 for south-eastern Alaska. Also, it looks like a trend that is accelerating all the way to the last time stamp. Relating this back to the estimates of the velocity and acceleration parameters regarding south-eastern Alaska, this seems to confirm the finding that the ice-melt off of Alaska is accelerating.

Regarding the first principal component, it is not so interesting to look at as it just shows the main ice-loss being centered around south-central Alaska, so it won't be examined more closely for this regional analysis (but can be seen in the appendix, 8, along with its eigenvector).

Alaska Ice Melt-off:
As with Greenland and Antarctica, examining the amount of ice lost (or gained) each year is an important part of the analysis:

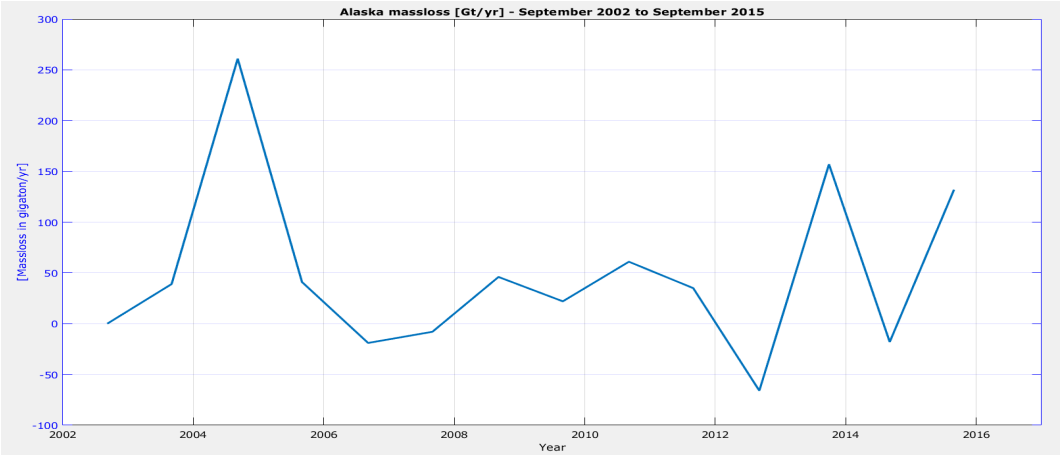

Figure 45: Alaska mask - Ice melt-off in Alaska from September 2002 to September 2015

While smaller compared to Greenland and Antarctica, there still is a significant loss of ice in Alaska observed here between September 2002 and September 2015.

4.2.4 Northern South America and the Amazon Rainforest mask

Authors note: The Amazon rainforest has the largest amplitude of oscillation in regards to water-distribution in the entire world, making it an interesting region to analyze with the GRACE satellites. As seen earlier for the global analysis in figure 20, it accounts for the second-most percentage of variance in the global principal component analysis, accounting for about 7.8% of the total global variance. This is likely because of its incredibly large annual oscillation of water-mass each year, due to the rainy season that peaks every May for the river area. I chose this region because of these vast amounts of water oscillation, to prove how GRACE is capable of doing more than just examining the melt-off of ice.

The peak of the rainy season changes depending on the location in South America. This can be seen in the figure below:

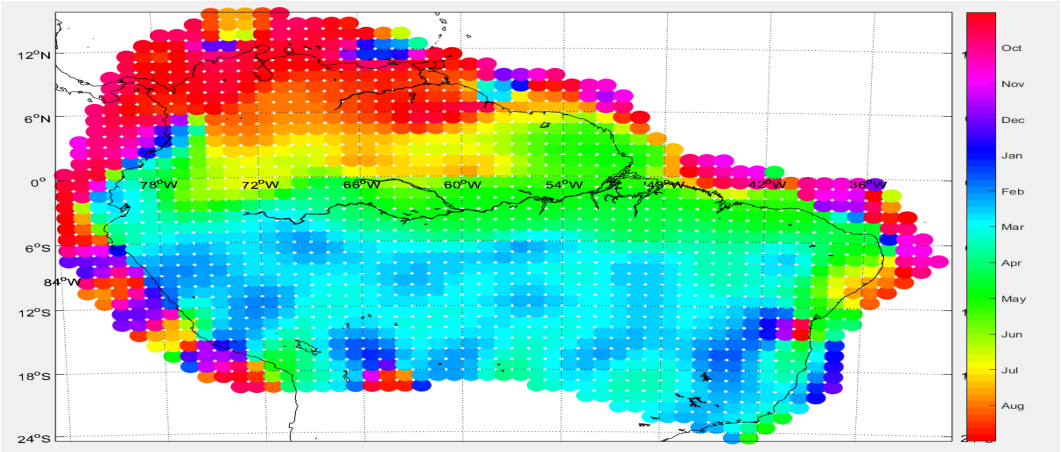

Figure 46: Amazon mask - The colorcoded peak of the rainy season in different areas of northern South America

To analyze the region, a mask is drawn around northern South America, as can be seen in appendix D.4:

The mask has a size of [1382 X 3 X 454], with longitudes spanning from 83.5**W** to 32.5**W**, and latitudes spanning from 15.5**N** to 24.5**S**.

Contrary to the earlier analyses, where the ice melt-off trend dominated the principal components, the situation is a bit different for this area of the world. The Amazon Rainforest is more complex, and the factors behind the change of water in this region can be explained by more than one factor, as illustrated on the scree plot in figure 47:

It is seen that most of the variance is still accounted for in the first principal component, which makes out (55.1% of the total variance), whilst the second largest principal component accounts for 23% of the total variance, and the third largest accounts for just 6.3% of the variance.

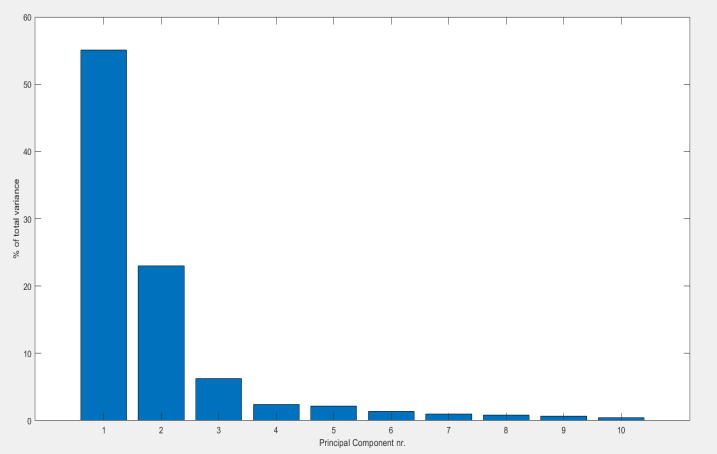

Figure 47: Amazon mask - Scree plot belonging to the principal component analysis

Another way to look at how the EWH oscillates in the Amazon river area is to examine a single gridpoint instead:

Point oscillation:

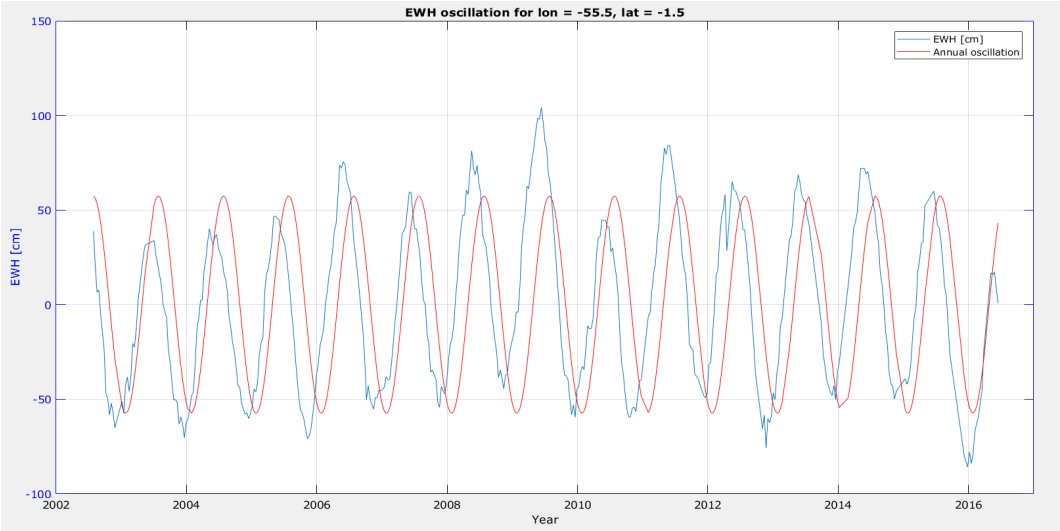

Figure 48: Amazon mask - Acceleration for a single point in the Amazon river area (coordinates can be seen in the title)

Interestingly, it can be seen that there exists some deviation between the annual oscillation and the [EWH] oscillation as a whole. Where does this come from?

The deviation is due to the half-annual and $\frac{1}{3}$ annual oscillations also having some impact on the total [EWH] value. The model as a whole account for these oscillations as well, as seen earlier in equation 1 in section 3.1. Therefore, these oscillations offset the complete model a little bit from the annual oscillation.

To gain some insight into what is happening here, the principal components are examined with their eigenvectors:

Amazon mask - principal component nr. 1:

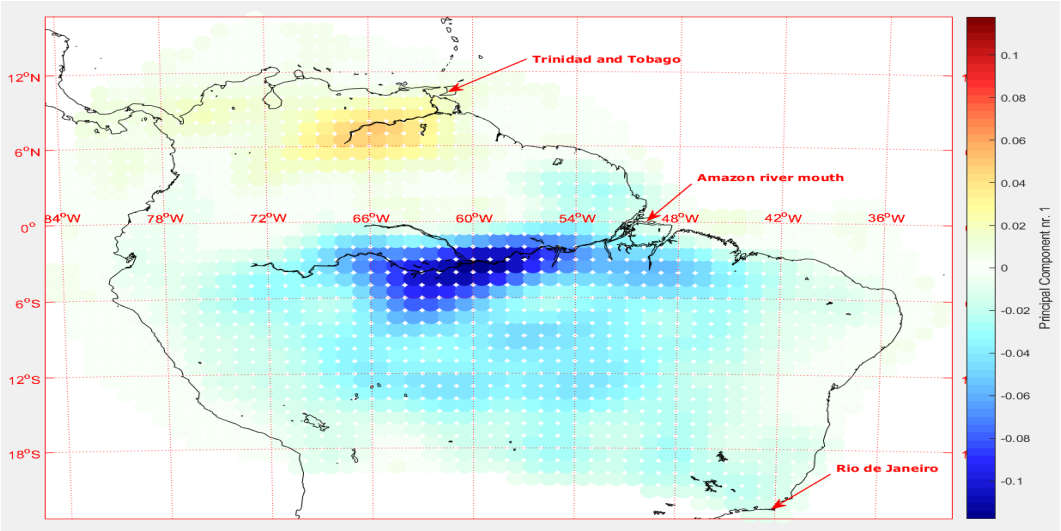

Figure 49: Amazon mask - Principal component nr. 1

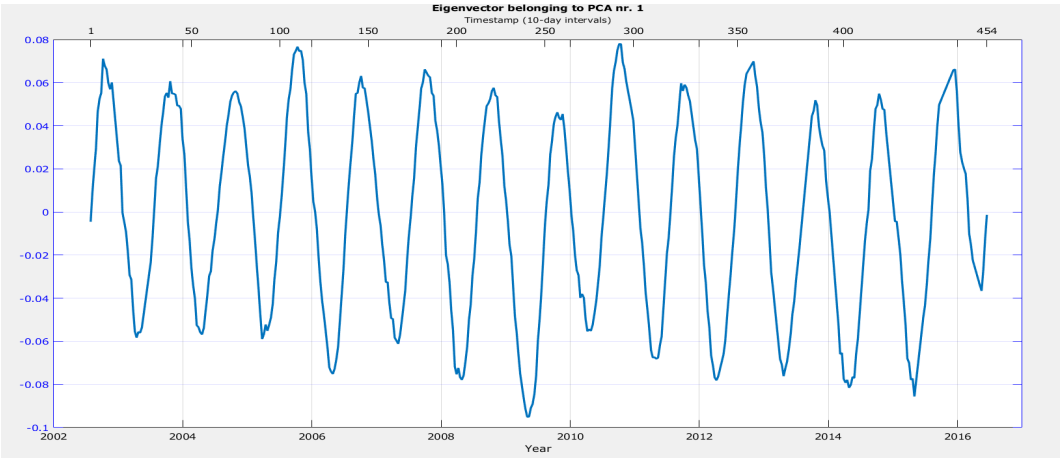

Figure 50: Amazon mask - Eigenvector belonging to principal component nr. 1

This is the most significant principal component. As seen on the eigenvector in figure 50, there is a very large oscillation, whose amplitude only vary slightly from year to year through the period.

It can then be argued that the first principal component likely express the main annual oscillation of water in the region. Comparing the spatial pattern with the eigenvector, it is also apparent that different areas peak at different times, in regards to its rainy season, if this is true. For example, the area around the central Amazon river seems to peak in the spring-early summer of the year (negative values area), and the area in the north-eastern part of the mask, in Venezuela close to the island of Trinidad and Tobago, seems to peak late in the year, around late fall-winter months.

To compare if this is true, these findings can be compared with the phase-plot first seen in figure 46. This confirms the assumption, that the rainy season in north-eastern Venezuela peaks around August-September, and the Amazon river peaks around May.

Additionally, the reason the two areas are differently weighted like that, and peak at such different times of the year, is likely because they are on opposite sides of the equator. The phase for the annual oscillation changes based on what side of the equator it is measured from. Furthermore, the water that flows through these two areas comes from 2 different places, which also explains the difference in the phase of the annual water mass peak accumulated here (O. B. Andersen and Allan Aasbjerg Nielsen 2018).

Amazon mask - principal component nr. 2:

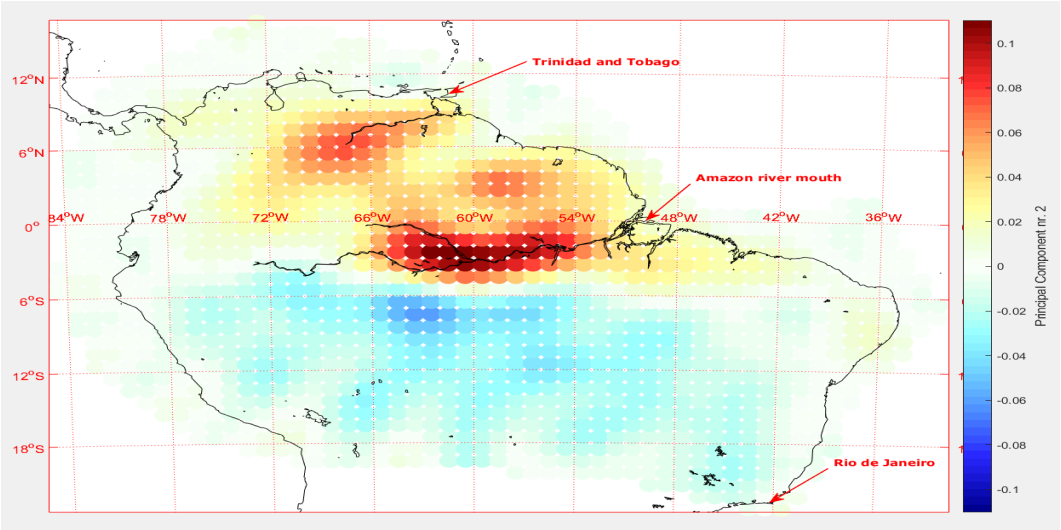

Figure 51: Amazon mask - Principal component nr. 2

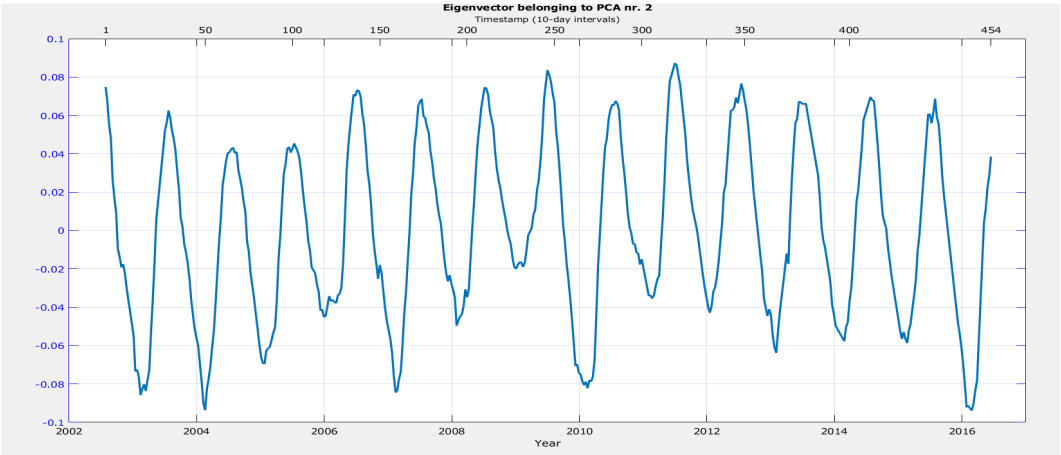

Figure 52: Amazon mask - Eigenvector belonging to principal component nr. 2

This principal component, accounting for 23% of the total variance, is also quite significant. The eigenvector seems to show some type of oscillation as well, that spans a cycle of about 12-years. To better understand it, it is compared with its spatial pattern.

In the spatial pattern, the same areas highlighted as in the first principal component can be seen, but this time they have the same sign, and it's only the magnitude of the weights that differentiates. So it might not be another seasonal oscillation that is seen here.

What it could show, however, is either an influence from the 11-year cycle of sunspot activity (activity in the sun) that changes the climate significantly in the area. Alternatively, it could be the quasi-periodic Pacific Decadal Oscillation (an ocean-atmosphere climate variability influenced by various factors, such as the El Nino event). However, this is just speculation. It could be caused by other factors as well, and the information and data needed to explain this phenomenon are beyond the scope of this project.

4.2.5 Decline of the Caspian sea

Authors note: As seen in figure 25, the Caspian Sea has been declining steadily for some time now. Considering the analysis has been on the movement or displacement of large water masses

so far, I thought that it could be interesting to examine more closely how water dries out and evaporates instead, as is the case for the Caspian Sea.

The Caspian Sea is the largest inland water body in the world, covering an area of $371,000km^2$ and extending 1200 [km] from north to south. It has no connection to the global oceans, and the variation of its sea levels varies mainly by the inflow of water from rivers as well as precipitation, and outflow from evaporation. Over the past several hundred years, the Caspian Sea Level has been declining. Recently, a collaboration between the Center of Space Research in Texas, Austin and many Geographics and Oceanology institutes around the world, published a paper in 2017 titled "Long-term Caspian Sea level change". In the paper, it was concluded that over the past 37 years, an increased rate of evaporation over the Caspian sea had played a significant role in the decrease of its water levels and that this decrease is expected to continue and increase in the future, due to climate changes.
In the study, they used a historical record of the Caspian Sea Level changes based on tide gauge measurements between 1840 and 2000 (shorter time scale and seasonal variations were omitted here) from a study published in 2014, titled *kostianoy et al., 2014*. With the help of 4 tide gauge stations, an average of their observations could be examined. To gain a profile of the entire period, leading up to 2015, they concatenated the satellite altimeter and tide gauge estimates of the Caspian Sea Level to construct a change time series covering the entire period (Chen et al. 2017a).

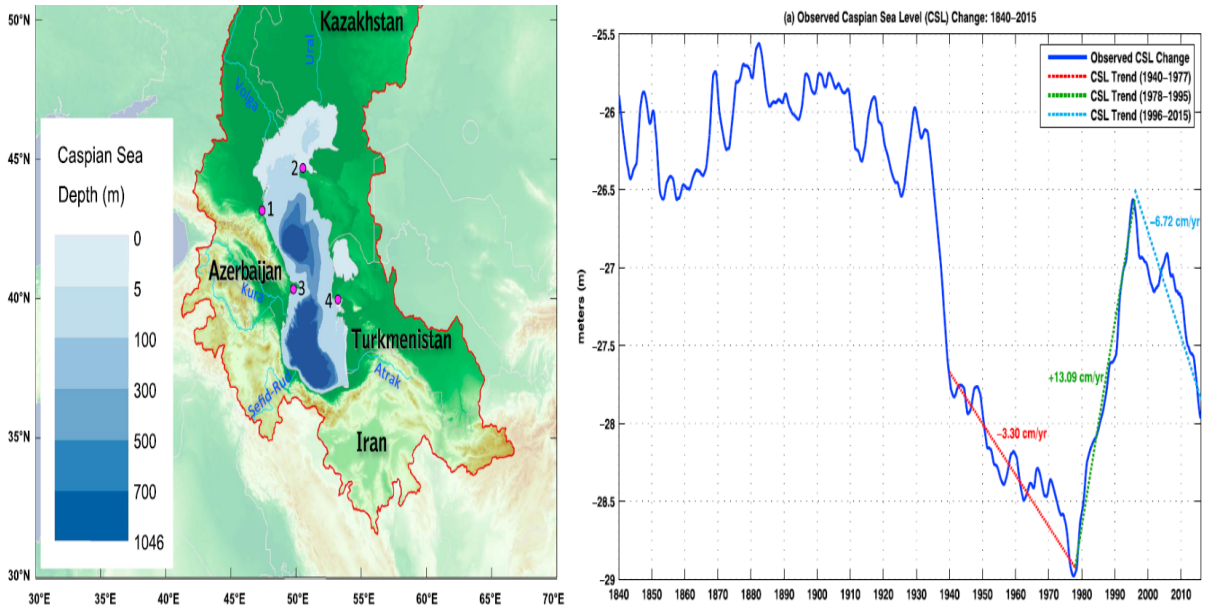

Figure 53: Caspian Sea map and its Sea Level changes. Source: (Chen et al. 2017a)

The 1940-1997 period in the graph above is based on tide gauge measurements, while the remaining period from 1997-2015 is based on satellite altimetry data, provided by CNES/Legos (Centre, CNES, and LEGOS n.d.)

The study examined the period 1979-1995 and the period 1996-2015 separately, to study the more recent changes in the Caspian Sea Level change rate. And it was concluded that during this time, the relative mean change rate was - 19.15 [cm/yr], (from +12.25 [cm/yr] to -6.90 [cm/yr], over these two periods. Moreover, the largest factor behind this change could be explained by an average increase of evaporation, equivalent to about 8.82 [cm/yr], along with an average decrease in precipitation, equivalent to about 5.13 [cm/yr]. Additionally, the observed river runoff from the Volga River (believed in the study to account for about 80% of the total discharge or runoff into the Caspian Sea) decreased by about 5.20 [cm/yr] during these 37 years.

While the GRACE satellites only operated from 2002 to 2016, it might still be possi-

ble to see some similarity between the examined GRACE data and this study. It should be noted, however, that GRACE measures the changes in mass, and that this study used different methods to monitor the change in sea levels. So it will be difficult to make a direct correlation between the graph in figure 53, and the graphs computed from the GRACE data in this project. However, the graphs that are computed from the GRACE data might confirm whether or not the Caspian sea is losing water (in terms of mass) and lead to an estimate of its own regarding the rate of change here, from 2002-2016.
A mask is drawn around the Caspian Sea, as can be seen in appendix D.5.
This is a quite small mask, of only [136 X 3 X 454] in size, with longitudes spanning from 45.5**E** to 55.5**E**, and latitudes spanning from 34.5**N** to 49.5**N**.

To study the decline of the sea, a single point is extracted from inside of it, and its decline in [EWH]-values over time is examined, as illustrated below:

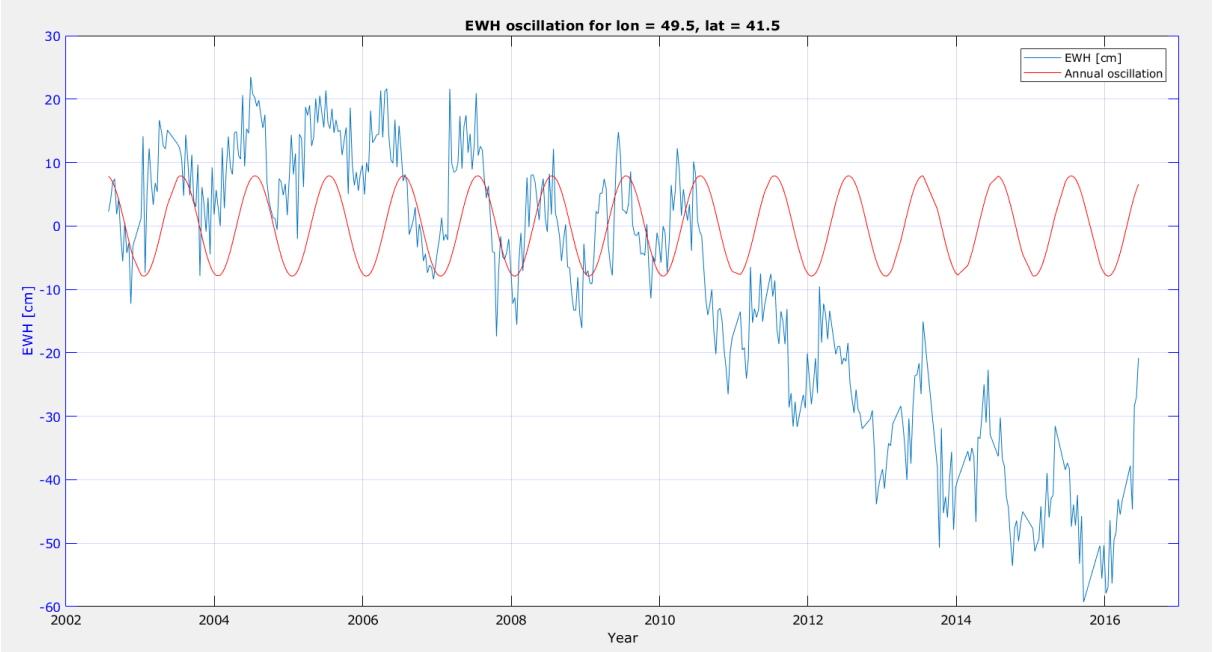

Figure 54: Caspian Sea mask - Decline of the Caspian sea (point examination)

Looking at this grid point change over time, a clear, declining trend is observed. Now, to increase the understanding of this phenomenon, the velocity and acceleration parameters are estimated:

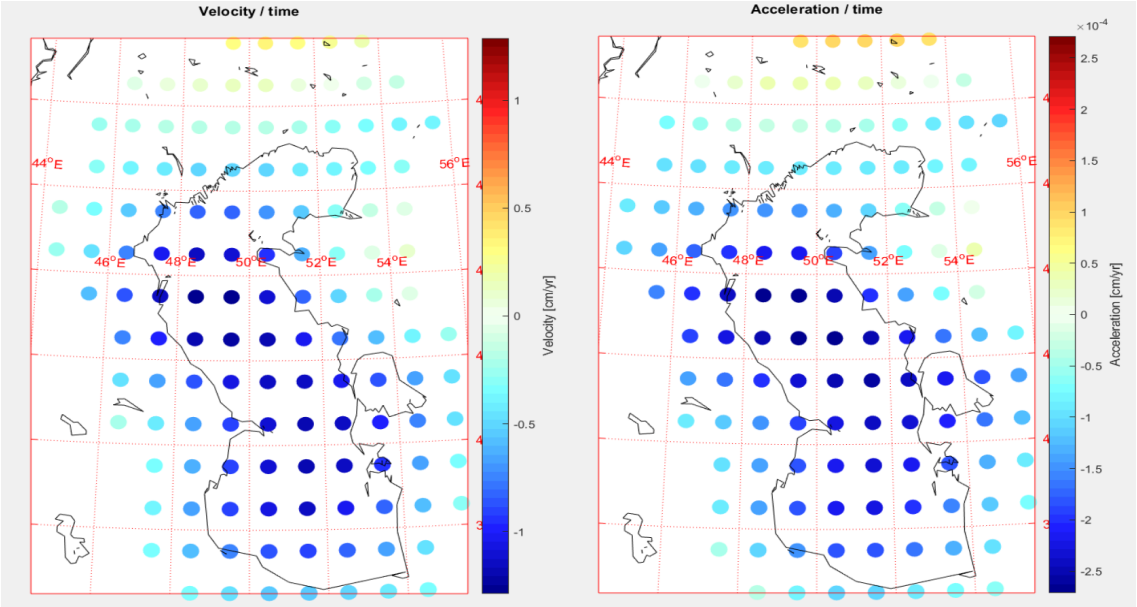

Figure 55: Caspian Sea mask - Velocity and acceleration parameters

It is seen above that the Caspian Sea is still declining at a fast rate, as of the 1st of January 2016, and that this decline is accelerating overall.

Following this, the total amount of water (in gigatons) over time in the sea is plotted for the mask area. The latitude-dependant areas of each grid point has been correlated according to the formula seen in 3.10.

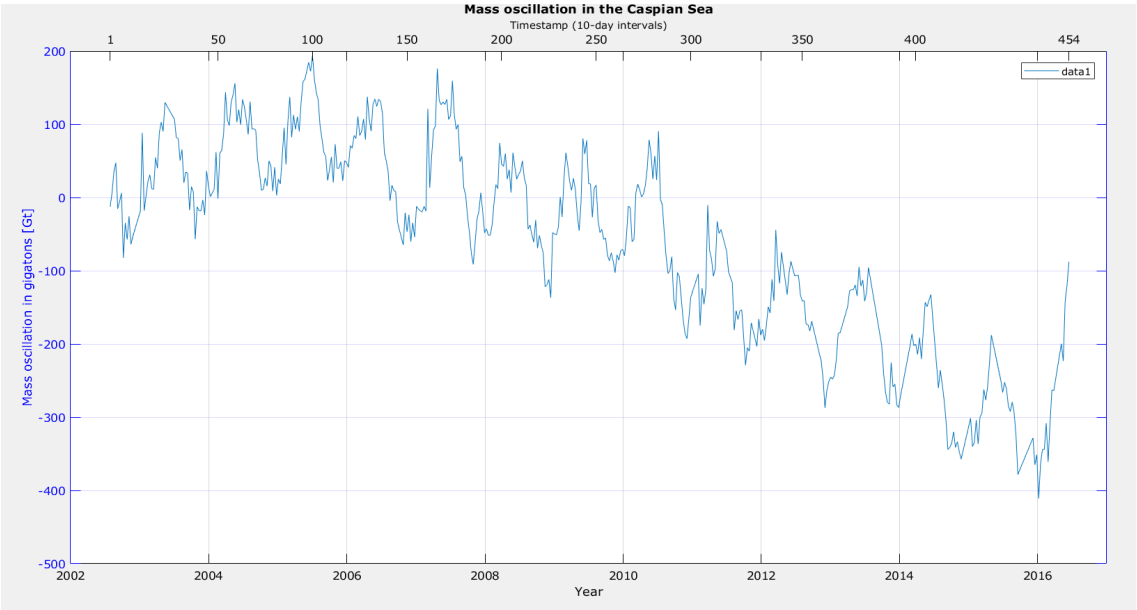

Figure 56: Caspian Sea mask - Mass oscillation in the Caspian Sea (in Gigatons)

Here a clear, accelerating trend of water loss in the Caspian Sea can be seen for the entire mask. Hence, it is easy to conclude that the Caspian Sea is losing water at an accelerating rate.

Even though the Caspian Sea is a relatively large basin, this is **alot** of water loss. Considering that 1 gigaton is approximately 264 billion gallons of water and that an increase in 365 gigatons of water in the oceans would contribute to about 1-millimeter increase in global sea levels (Boening 2014), this is a rate of change that is much more dramatic, considering the

Caspian Sea "only" covers an area of $371,000km^2$ with a water volume of about $78,200km^3$ (Observations 2005), (worldlakes.org 2004).

4.2.6 Water-mass balance shift in the Himalayas and Tibetan Plateau

Authors note: In the article by M.Rodell in Nature (Rodell 2018), it was stated that the mountain ranges of Himalaya suffered groundwater depletion, water depletion, and precipitation decrease, while the Tibetan Plateau was being subjected to increased precipitation. I chose this region because I think that this water-mass balance shift of the region could be interesting to examine more closely with GRACE, especially regarding its supposed decline of snow-water storage.

A map of the region can be seen below:

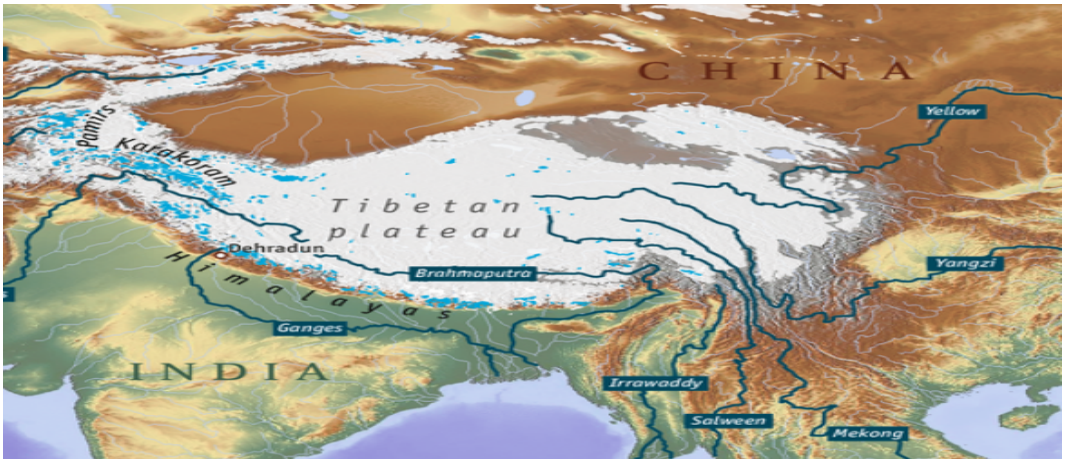

Figure 57: Map of the Tibetan Plateau

A mask is drawn around the Himalayas and Tibetan Plateau, as can be seen in appendix D.6.

The mask has a size of [274 X 3 X 454], with longitudes spanning from 74.5**E** to 101.5**E** and latitudes spanning from 27.5**N** to 38.5**N**.

Following, the full analysis is computed for the mask area, including the principal component analysis. The scree plot is illustrated for the mask in figure 58:

For this mask, the principal component nr. 1 accounts for (48.6% of the total variance), while the principal component nr. 2 accounts for 18.6% of the total variance, and the third largest accounts for 9.9% of the total variance.

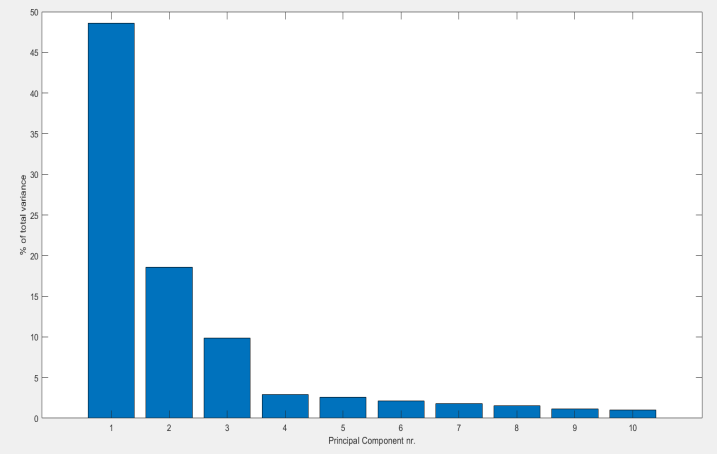

Figure 58: Tibet and Himalaya mask - Scree plot belonging to the principal component analysis

Unfortunately, the *M_maps* package operates poorly in this region, as it is difficult for it to visualize this geographical area well enough. Therefore, a different plotting method has been used for plotting the principal components in this region. The plotting method used is a user-made function called *Plot_google_maps*, which "Plots a google map on the

current axes using the Google Static Maps API" as is quoted from its documentation. A normal scatter function (instead of the conventional *m_scatter*, as used in most of this report) had to be used to project the principal components correctly with the *plot_google_maps* function. The results are seen below.

Tibetan Plateau Mask - principal component nr. 1:

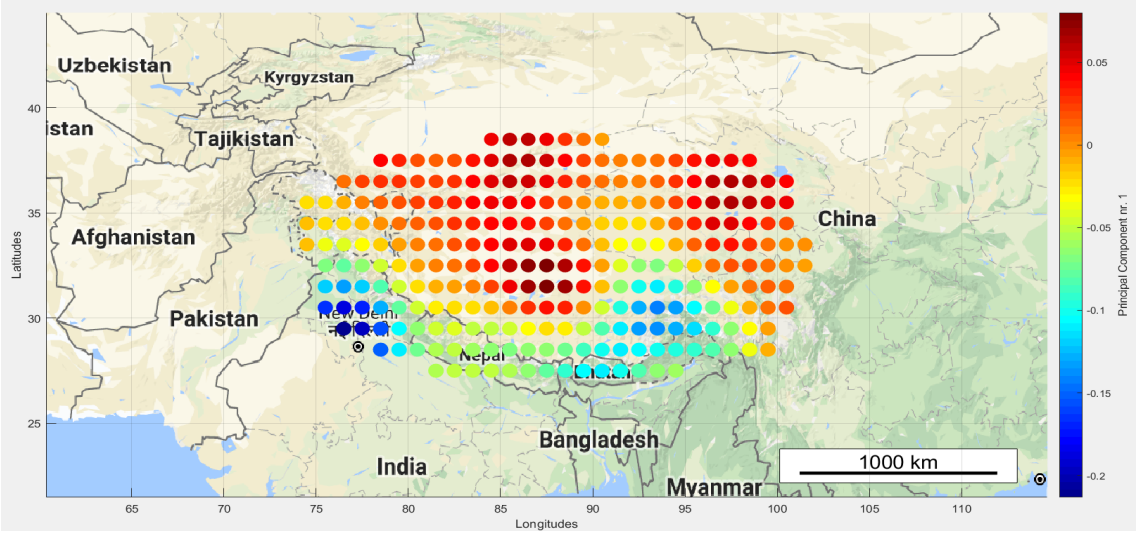

Figure 59: Tibet and Himalaya mask - Principal component nr. 1

Figure 60: Tibet and Himalaya mask - Eigenvector belonging to principal component nr. 1

Interestingly, a quite dramatic shift can be seen between the mountain ranges of Himalaya and the Tibetan Plateau. The Tibetan Plateau is known for being quite dry and barren, while the Himalayan mountains contains vast amounts of ice and snow, more than any other region in the world outside of the polar regions, that melts on a large scale during the summer. The shift between negative and positive values fits well geographically with the mountain ridge that separates the Tibetan Plateau with the Himalayan mountain ranges, as it makes sense to see two different climate phenomena here.

Comparing with the eigenvector, a small oscillation may be seen that peaks during the first months of the year, and drops most during the summer-fall period of the year. This fits well with the snow melting off during the summer months (the direction and sign of the eigenvector is arbitrary). The snow and ice that melts from the glaciers of the Himalayan mountain ranges supplies permanent flow to most of the major river systems in Asia, transporting the water far away, sometimes all the way out into the ocean (such as through the Yangtze river that flows

through all of China, or the Ganges river that flows through India and Bangladesh) (Earths Climate System).

Also interesting is to see that there is a trend of mass change in this principal component. Comparing with figure 25 from the Nature paper, an overall trend of groundwater depletion, water depletion and precipitation decrease in the areas of the Himalayan mountains (region 7 and region 13 in the figure depicting the annotated map of TWS trends) can be seen. The overall trend contribution from these regions should then be negative. However, a precipitation increase in region 10 in the model can also be seen, which looks to be roughly the same geographical area as the Tibetan Plateau. And this is the area that had the large positive values.

So if the large negative values on the eigenvector is equivalent to a loss of mass, from ice melting for example, then the large positive values might mean an increase in mass. So the overall trend of the model explains that the area of the Tibetan plateau is increasing in its mass of water, possibly due to increased precipitation and greater melt-off from the surrounding mountains. Meanwhile, the Himalayas are losing water over time (possibly due to climate change increasing temperatures and therefore ice melting in the mountains).

Tibetan Plateau mask - principal component nr. 2:

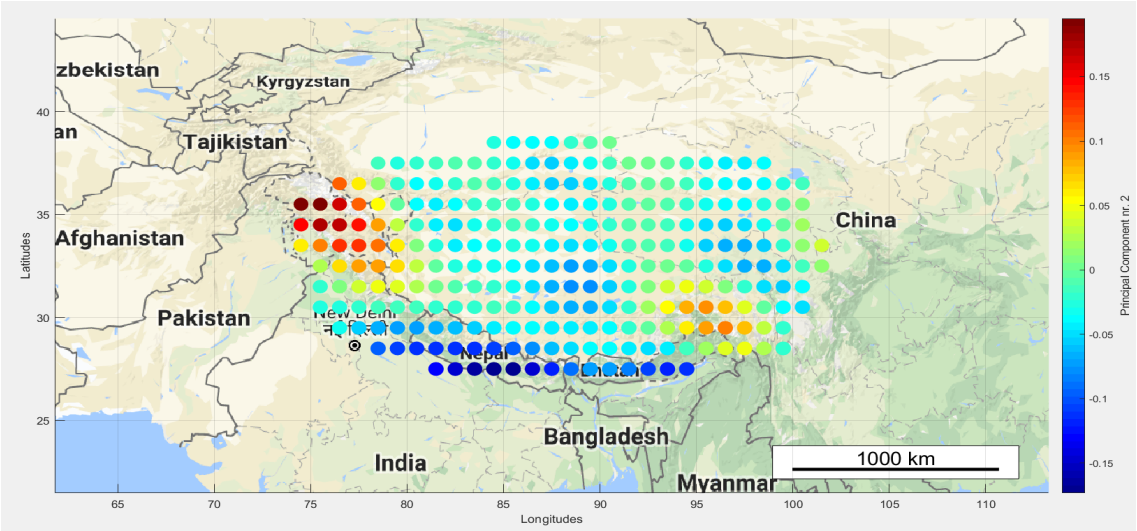

Figure 61: Tibet and Himalaya mask - Principal component nr. 2

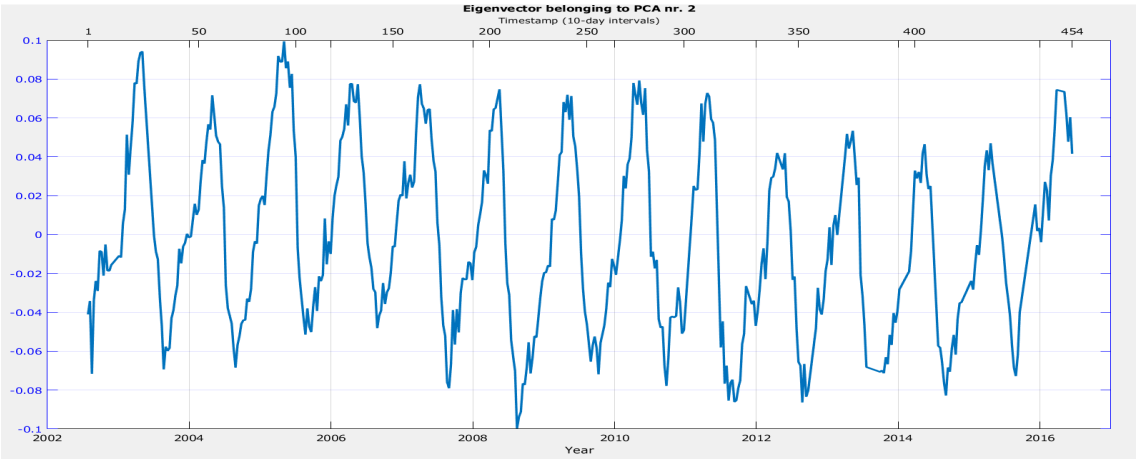

Figure 62: Tibet and Himalaya mask - Eigenvector belonging to principal component nr. 2

This principal component shows a significant, annual oscillation.
Looking first at the weights of the areas in the spatial pattern of principal component nr. 2, it is seen that most of the region around the Tibetan Plateau is weighted zero or slightly negative. So these are not so interesting.

However, there is a quite powerful, negative signal around the mountain ridge of Himalayas, and also a quite sizeable positive signal in the far western part of the mask, around Jammu and Kashmir in northern India.

What this could mean is a difference in the peaks of the rainy season, based on the geographical areas. The oscillation seen in the eigenvector seems to peak around the beginning of the year and drops to its lowest around summer-fall. Comparing this with the spatial pattern, and noting the weight difference in the different areas, it can be deduced that this makes sense. For the area of Jammu-Kashmir, it peaks in the spring months of about March-April, and for the Himalayan mountain ranges, the rainy season peaks around the late summer or fall months of August-September (similarly to the phenomenon that was seen in Principal Component nr. 1 for the Amazon Rainforest mask (see figure 49). To confirm that this is true, it is compared with a phase-plot of the mask:

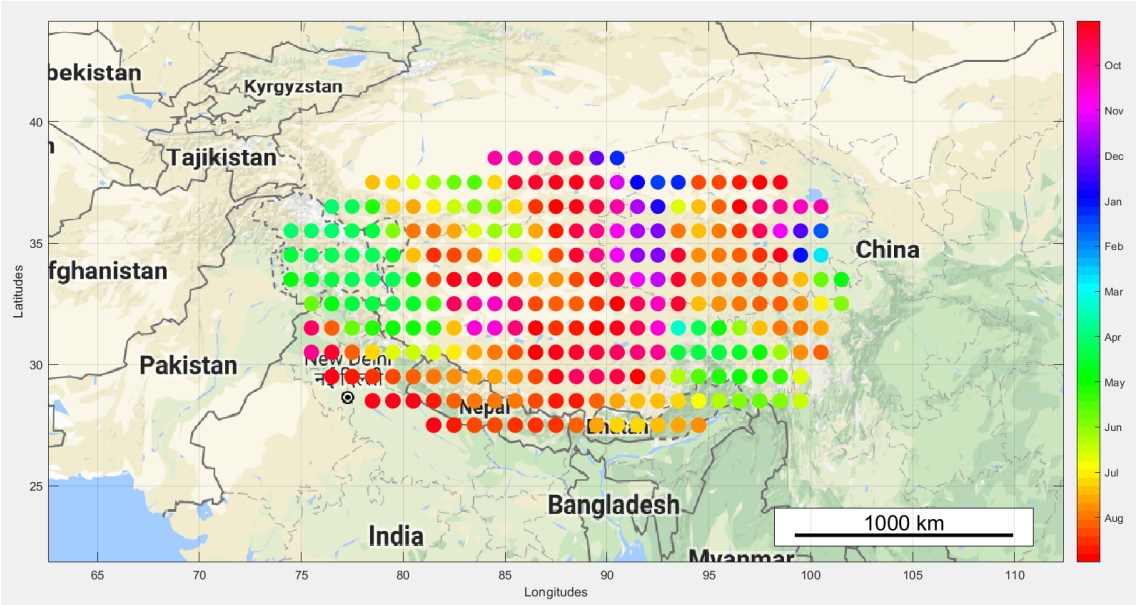

Figure 63: Tibet and Himalaya mask - Peaks of the rainy seasons

As seen on the phase plot this indeed adds up, as it shows that the rainy season peaks in April-May for the Jammu-Kashmir region and that it peaks around August-September for the Himalayan mountain ranges. So in conclusion, the principal component nr. 2 and its eigenvector expresses the large, seasonal oscillation for these two regions.

It was previously concluded that there seems to be increased precipitation and mass increase in the Tibetan Plateau, as well as some mass decrease in the Himalayan mountain region. But how does it look for the distribution of mass as a whole? Is the region analyzed being subjected to a net loss of water, over the years? This can be examined by summing up the amount of water in each grid point for each time stamp, and plotting it as a time series as seen below:

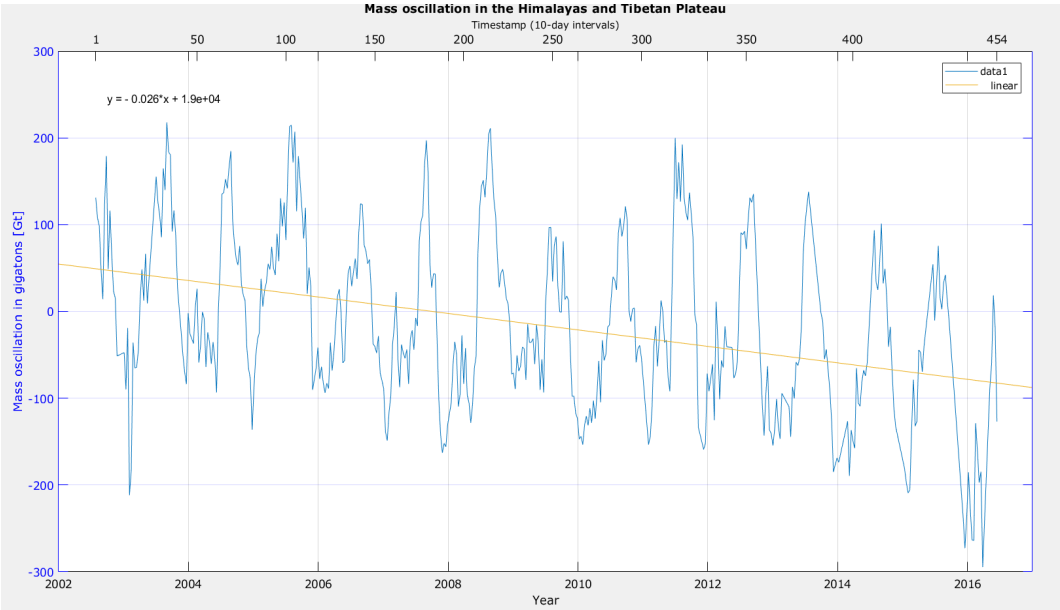

Figure 64: Tibet and Himalaya mask - Mass oscillation in the Tibetan Plateau and Himalayas

On the plot in figure 64, the distribution of water masses seems to oscillate between ±200 gigatons at the beginning of the period. However, moving towards the end of the time series, it is seen on the linearly fitted line that the amount of water is declining over time. Why?

Looking back to the paper by Rodell published in Nature, it is stated that "Satellite altimetry and Landsat data indicate that the majority of lakes in the Tibetan Plateau have grown in water level and extent during the 2000s owing to a combination of elevated precipitation rates and increased glacier-melt flows, which are difficult to disentangle." (Quote: (Rodell 2018)). This confirms the previous conclusion that the Tibetan Plateau increases in water levels. However, the article also states that there is a trend of "glacier offset and warming-enhanced evaporation" and that "it is probable that warming-induced glacier mass losses will begin to exceed surface-water gains, particularly if the fraction of frozen precipitation decreases." (Quote: (Rodell 2018)). This is more concerning the coming years, though, leading all the way up to the year 2100. So this itself might not be enough to explain the loss of mass over time, as is seen here.

In conclusion, it is hard to pinpoint the factors that might lead to this loss of water seen in the analysis, except that it is most probably due to global warming-enhanced melt off in the Himalayas, whose water is then washed out into the oceans by the major rivers in the area.

4.2.7 Earthquakes in Sumatra and Fukushima

Authors note: The GRACE satellites gather information about the changes of gravity in each grid point on the globe, with a 1^o resolution. This is primarily due to the changes in water flow, as water is one of the only sources that can change its gravity significantly over a 10-day period. Most other things on Earth changes much more slowly, over a very long timescale.

There is one particular natural phenomenon that stands out quite clearly, though: Earthquakes. Since earthquakes rupture over a very brief period, the signals from these events stand out as "spikes" in the EWH data quite clearly. So by making a regional mask analysis of an area around the earthquake, what is likely the movement of the tectonic plates themselves can be seen in the spatial pattern of the principal components quite clearly, at least if it is a subduction earthquake (see for example PC1 and PC2 for the Sumatra earthquake below in this chapter). This is very interesting I think, which is why I chose especially Sumatra but also

Fukushima for a region to analyze more closely.

Before moving on with the analysis, a summary is given on the definition of an earthquake first:

A brief introduction to earthquakes and plate tectonics:

This is a shortened summary of earthquakes. For the full elaboration, please refer to appendix C.

Most earthquakes arise from tectonic events, and in most cases from movements on faults (A *fault* is a fracture of a volume of rock, resulting from a large displacement due to rock-mass movements, usually due to tectonic plate forces and active plate boundaries. A *fault plane* represents the fractured surface of this deformation) (Fundamentals of Geophysics; Interior and U. G. Survey 2006; Program 2018)

The following *Elastic Rebound Model* depicts the way an earthquake typically may occur. It is illustrated below in the far left side of figure 65, along with the three different types of faulting an earthquake can have, and the three types of tectonic plate boundaries that exist.

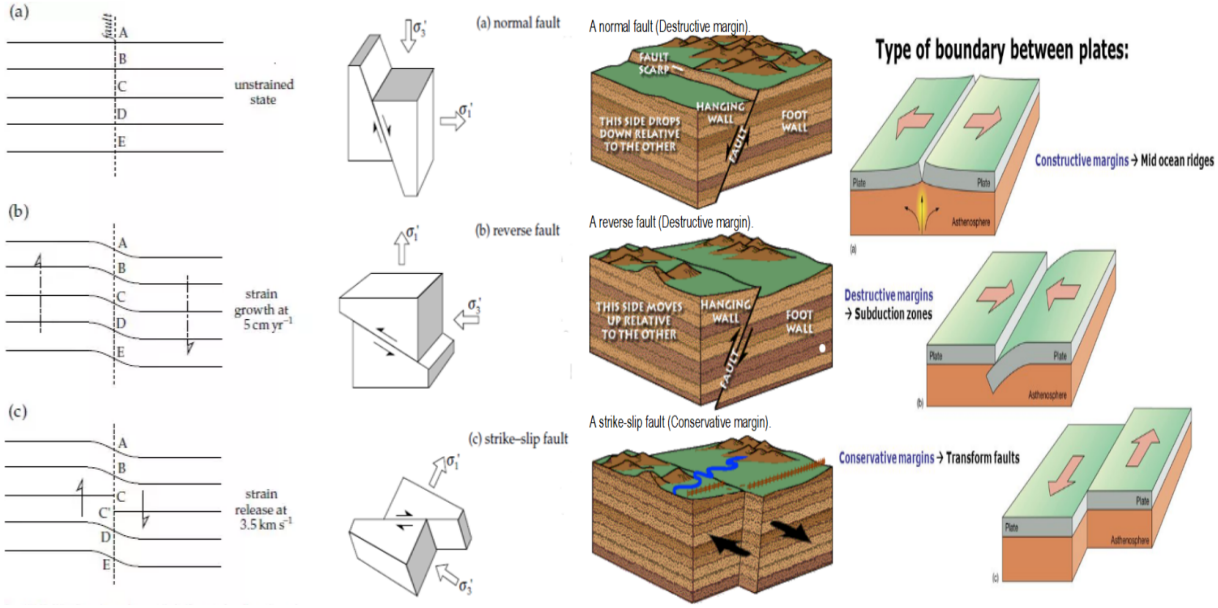

Figure 65: Earthquakes, fault types and plate boundaries
Source: (U. S. G. Survey 2017), (Fundamentals of Geophysics)

When 2 tectonic plates meet, they will "rub against each other", thus building up tension over many years. The stress or strain between the plates continues to accumulate until it exceeds the *yield stress* of the tectonic plate (the maximum amount of elastic deformation a material can withstand. See also appendix B for further elaboration). When this breaking point is exceeded, the rupture occurs, and a violent displacement along the fault-plane takes place. During this event, all the stored potential energy between the plates, which have been accumulating over many years, is released in a couple of seconds as a *shock wave*. It is not the entire length of the fault-plane that is activated though, only the section of which the breaking point has been exceeded. The magnitude of the resulting earthquake depends on the length of the activated fault-plane (Fundamentals of Geophysics).

The behavior and impact of the earthquake also depend greatly on the fault type. For example, the Sumatra 2004 earthquake was a subduction megathrust earthquake (type b in figure 65), which makes a violent upward-downwards motion. This is the kind of earthquake that creates devastating tsunamis, which was also seen in Fukushima, 2011. So in this type of earthquake, where one plate is subducting beneath the other, enormous amounts of mass are moving relatively to each plate (for the complete elaboration, please refer to appendix C) (Stein and Okal 2005).

GRACE measurements of earthquakes:
When earthquakes occur, enormous amounts of mass, over a vast region, can shift very suddenly. A good example is the Sumatra 2004 example mentioned above. This kind of mass-displacement signal is very visible for the GRACE satellites since they measure changes in mass over short time periods. So all large-scale earthquakes that happened during the period that the GRACE satellites were in operation can be seen clearly as outlying "spikes" in the EWH data.

Below are two examples for the two earthquakes in Sumatra, Indonesia (the 9.1-9.3 magnitude 2004 earthquake and the 8.6 magnitude 2012 earthquake), and the 9.0-9.1 magnitude earthquake in Fukushima, Japan in 2011, where just one point was extracted for examination:

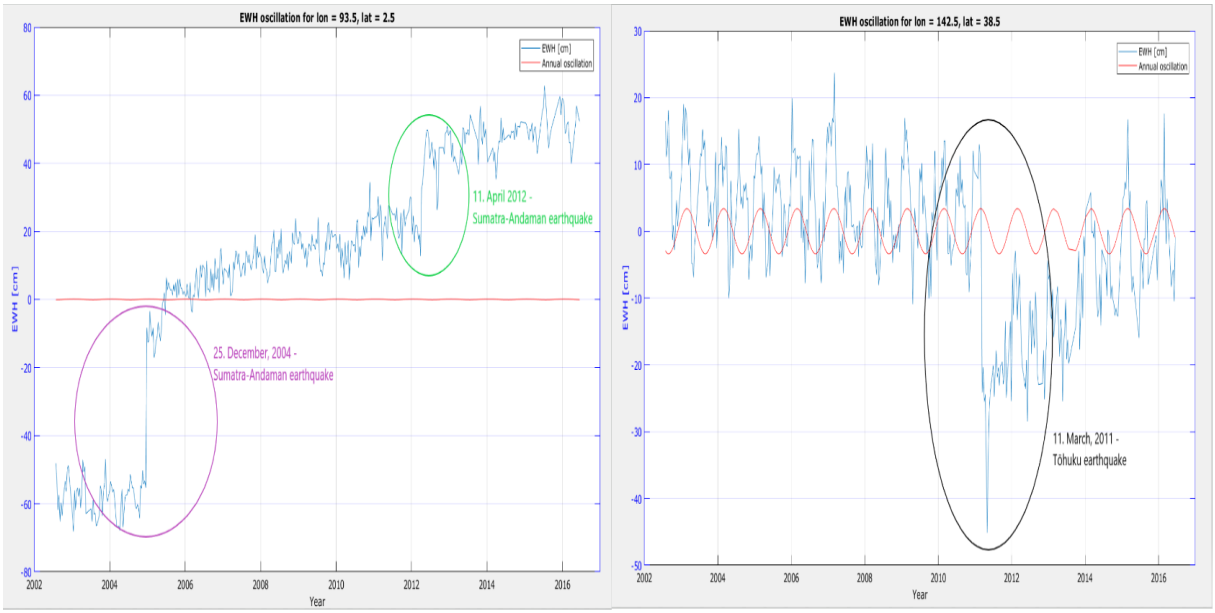

Figure 66: Earthquakes - Point examination in the earthquake epicentres of the Sumatra 2012 and Fukushima 2011 earthquakes

In the figure above, the spikes in the EWH-data can be clearly seen around the time of the earthquakes. These grid points were chosen having coordinates equal to the epicenter of the 2012-Sumatra earthquake (left) and the 2011-Fukushima earthquake (right).

Looking at the timestamp of the spikes, it is apparent that it fits the timeframe of the earthquake incidents precisely.

The reason the epicenter of the 2012 earthquake was chosen instead of the epicenter of the 2004 earthquake, for example, was so not to drown out the signal of the 2012 earthquake. The 2004 earthquake was so powerful that its "spike" could be seen in most places in the Sumatra region, but this is not the case for the 2012 earthquake. As an example, figure 67 shows another point examination just a 249 [km] away from the 2012-earthquake epicenter:

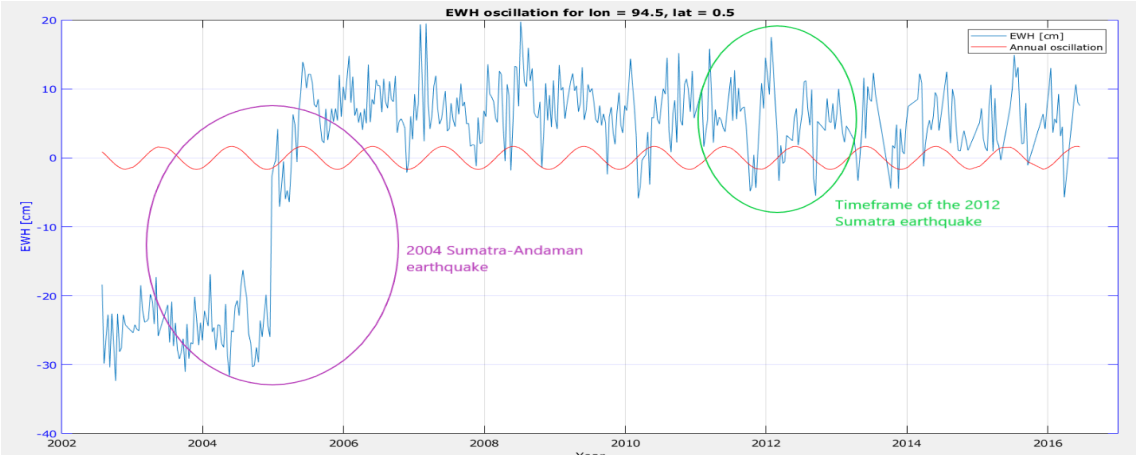

Figure 67: Earthquakes - Comparison of a different point examination, 249 [km] from Sumatra 2012 earthquake epicenter and 343.5 [km] from Sumatra 2004 earthquake epicenter

As seen in the above figure, the 2012-Sumatra earthquake is not visible at all anymore, even though its epicenter was only 249 [km] away. However, the 2004 Sumatra-Andaman earthquake, being 343.5 [km] away, is still clearly visible (the distances was calculated by a *M_maps* function named *m_lldist*, which computes the spherical earth distance between points in long/lat coordinates). This clearly shows how much more powerful the Sumatra 2004 earthquake was. The large difference in the spike signals is most likely due to the difference in the fault types since the 2012 earthquake was a strike-slip earthquake, and the 2004 earthquake was a reverse fault or thrust fault type earthquake (see figure 65). A strike-slip earthquake is characterized by only a horizontal movement between the plates, which means there is much less, if any, relative mass displacement between the two plates (O. B. Andersen 2018).

Drawing a mask around Sumatra (as seen in appendix D.7), the spikes are still quite visible in the time series of the eigenvector. It can also be seen below that the epicenter of the earthquakes fit the spatial pattern of the principal components:

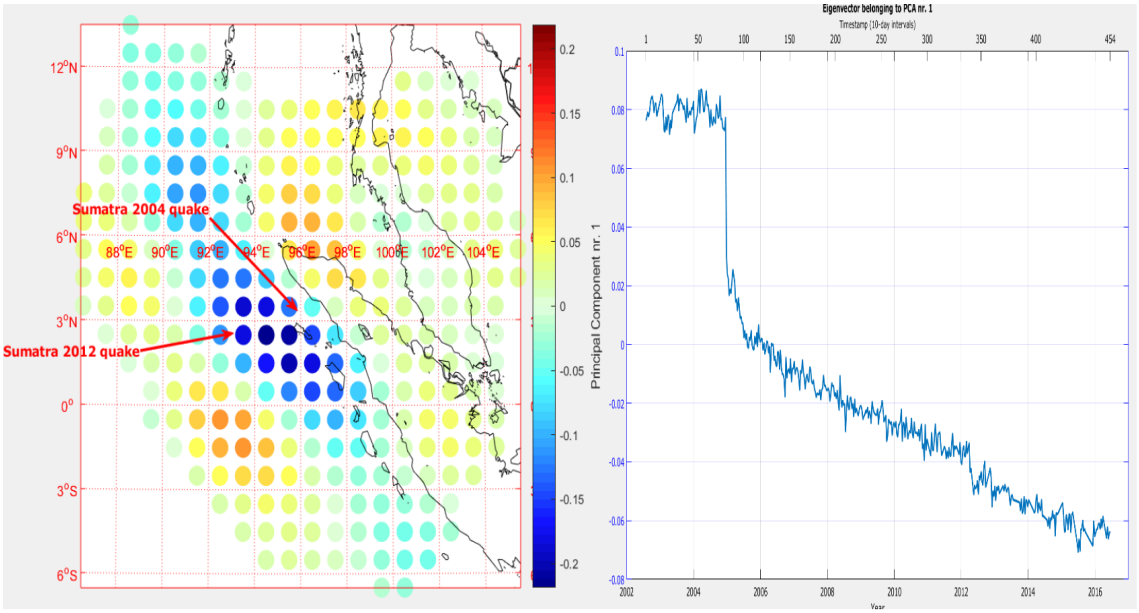

Figure 68: Sumatra mask - Principal component nr. 1 and its eigenvector

This principal component, accounting for 70.2% of the total variance, most likely shows the earthquake and the shift of mass along the plate boundaries. When examining the spatial pattern, it is seen that around the epicenters (denoted with the red lines) there is a large column of negative weights, and all around them are positive weights. Also, this 'column' of

negative weights that run up along the coast fits well with the geographical location of the Burma microplate, which was overriding (moving on top of) the subducting Indian plate (see figure 69). Thus, what is being shown here in this principal component is likely the Burma Plate moving on top of the Indian Plate, which is why there is such a contrast between the oppositely signed weights for the two geographic areas.

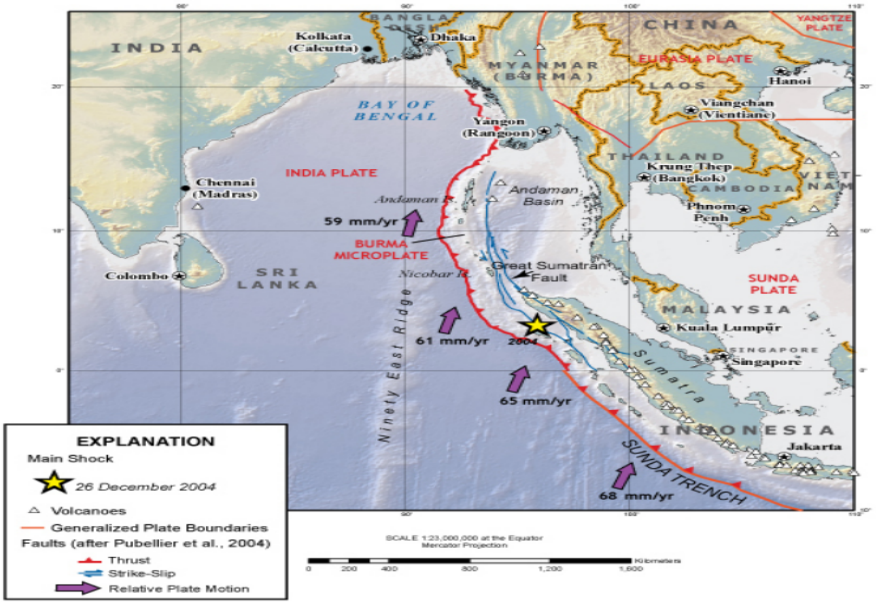

Figure 69: Tectonic Plate boundaries in south-eastern Asia
Source: (Interior and U. G. Survey 2018)

Additionally, the topography and bathymetry of Sumatra can be seen in the figure to the right.

To increase the insight into what is happening in this region, the second principal component is drawn, accounting for 16.4% of the total variance. Here, the opposite pattern of principal component 1 is seen, where the epicenters are lying on a line more or less perpendicular to the coast of Sumatra. The weights along this line all have positive weights, and all points around this line are negative. Also interesting is that the direction of the weight shift is opposite for the 2004 earthquake and the 2012 earthquake, as seen in the eigenvector. This might have something to do with the fault type, as the 2004 earthquake was a megathrust type earthquake in a subduction zone, making a violent upward-downwards motion during its rupture, and the 2012 earthquake was a strike-slip fault type earthquake, where the two tectonic plates were sliding past each other laterally during its rupture. It was also the largest strike-slip earthquake ever recorded (California - Berkeley 2012).

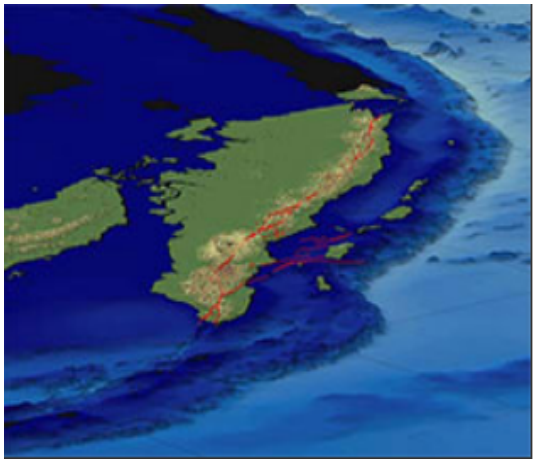

Figure 70: Bathymetry and topography of the Sumatran plate boundary *source: (Observatory and California Institute of Technology 2018)*

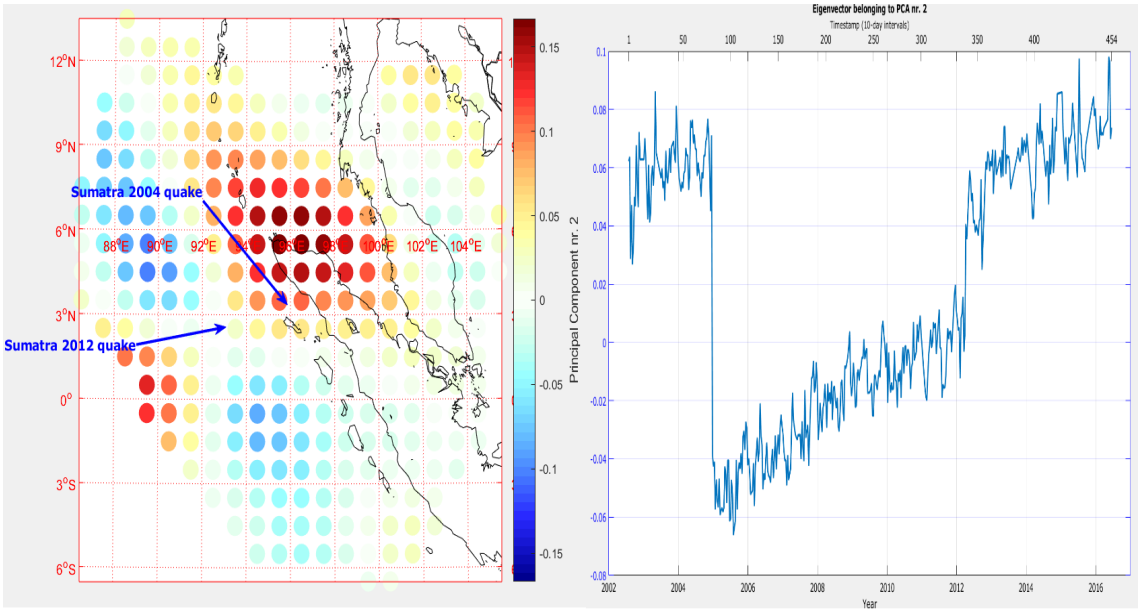

Figure 71: Sumatra mask - Principal component nr. 2 and its eigenvector

Fukushima, Japan 2011 tectonic plate movement

Similarly, by drawing a mask around Japan and making a principal component analysis here, the tectonic plate movements relative to each other can also be seen around the incident of the Fukushima megathrust earthquake. This can be seen below in the comparison between the spatial pattern of the first principal component and a map of the tectonic plates in the area:

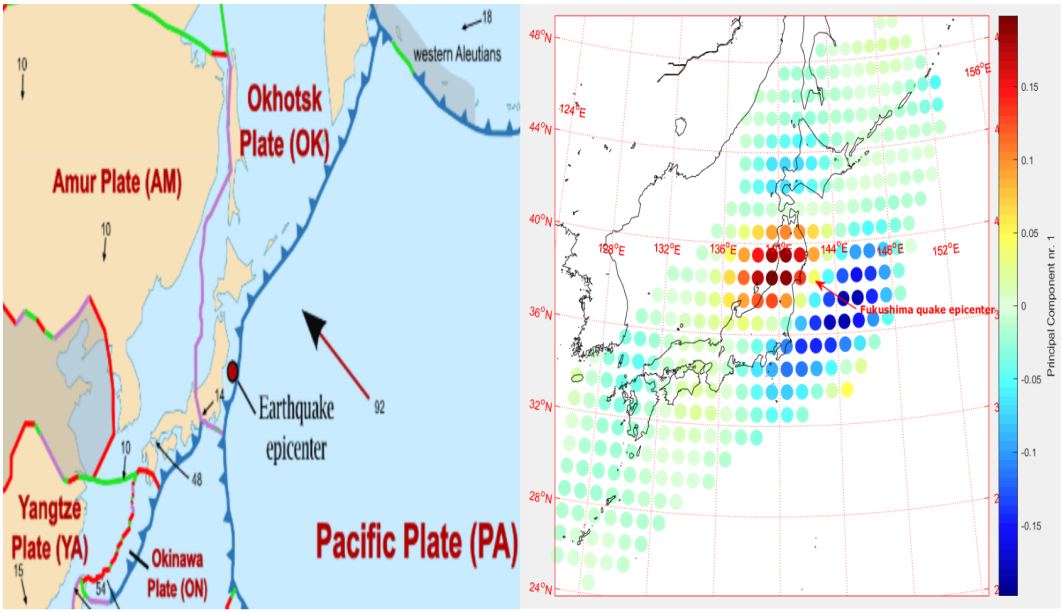

Figure 72: (Left): Visual representation of the tectonic plate movement during the 2011 Fukushima subduction megathrust earthquake in Japan. (Right): Principal component nr. 1 for the mask.
source: (Urbano 2011)

The chosen roipoly mask can be seen in appendix D.8.

5 After GRACE

5.1 The final days of the GRACE satellites

Originally, the GRACE satellites mission was designed to only last for 5 years, between 2002 and 2007. It was however extended all the way up to the beginning of 2018 (a little earlier for

GRACE-2, which ran out of fuel and suffered some battery failures).

For the two GRACE satellites to accurately track the changes in the gravity field beneath them, it required that their instruments were fully functional all the time. However, on the 3rd September, one of the 20 batteries in the GRACE-2 satellite stopped functioning altogether, due to an age-old battery issue. This was the 8th battery that had faulted since its launch in 2002. This event subsequently resulted in a complete loss of communications with the satellite on the following day.

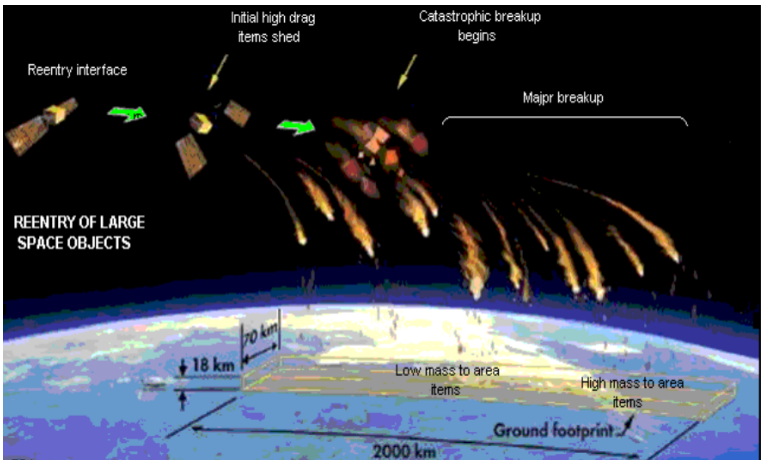

Figure 73: Re-entry illustration, image source: (Academy 2018)

On September the 8th, the GRACE missions operations team succeeded in restoring contact with the satellite, by bypassing its flight software system. After some evaluations on the health of the satellite, the team concluded that the battery initially lost on September 3rd had restored its full voltage, and the mission could continue. However, based on the many faulty battery events, and the fact that the twin-satellites were almost out of fuel, the team decided that the following October/November 2017 science data collection mission would be their last. The purpose of this final mission was to produce a new gravity-map to extend the duration of the GRACE satellites science data record as close as possible to the GRACE Follow-on successor mission, which is elaborated in section 5.2.

However, NASA stated on October the 27th that "it became apparent by mid-October that GRACE-2's remaining battery capacity would not be sufficient to operate its science instruments and its telemetry transmitter. Consequently, the decision was made to decommission the GRACE-2 satellite and end GRACE's science mission". (Quote from (Buis 2017)).

The atmospheric re-entry of GRACE-2 occurred on the 24th of December, where it burned up in the atmosphere. The GRACE-1 satellite was allowed to operate a little longer, due to its batteries still being healthy. Carmen Boening, from the GRACE project science team at NASA's Jet Propulsion Laboratory, stated the following: "GRACE-1's remaining fuel will be used to complete previously planned maneuvers to calibrate and characterize its accelerometer to improve the final scientific return and insights from the 15-year GRACE record," (Quote from (Foust 2017)). GRACE-1 made its re-entry on the 10th of March 2018. Even though a couple of small pieces from the satellites were expected to survive the reentry, the risk they posed was minimal and was within NASA requirements for satellite reentry, NASA spokesperson Alan Buis told SpaceNews (SputnikNews 2017).

5.2 GRACE Follow-on

The two new GRACE Follow-on twin satellites was launched on 22 May, 2018 on a SpaceX Falcon 9 rocket, sharing its payload with 5 other NASA Iridium NEXT satellites.

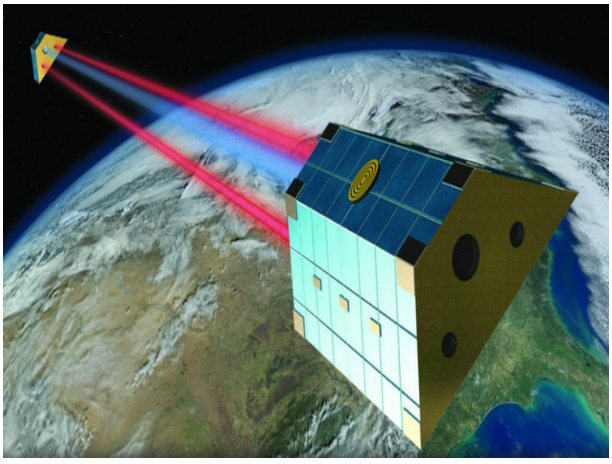

Figure 74: GRACE Follow-on concept art

The GRACE Follow-on satellites are almost identical to the original GRACE satellites, in both purpose, design, and instrumentation. They also fly in a near-polar orbit, at an altitude of about 490 kilometers, circling the Earth once every 90 minutes. However, there are a few technological improvements from the original GRACE satellites, that was launched in 2002.

The new technological improvements on the new GRACE Follow-on satellites include new and better computer systems, more efficient solar cells, better star cameras as well as a much more efficient and precise distance measurement system between the satellites: The Laser Ranging Interferometry technique (LRI), based on heterodyne laser interferometry at 1064 nm. (see figure 75).

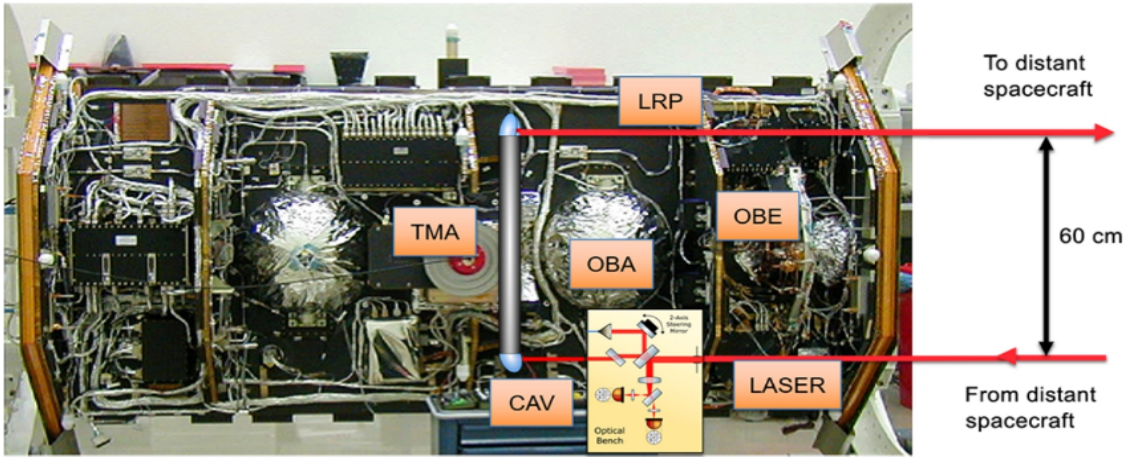

Figure 75: The Laser Ranging Interferometer instrument. Credit: Albert Einstein Institute, Hannover, Germany

The GRACE Follow-on mission works on the same principles as the previous GRACE satellites when it comes to how they measure the gravity fields below them.
However, using laser ranging interferometry in addition to the previously used microwave ranging interferometry enables the new GRACE Follow-on satellites to register distance changes between each other on a scale as small as the width of a human blood cell. This is no easy feat though, as the GRACE Follow-on satellites orbit the earth at approximately 220 [km] from each other. So as a backup system, the GRACE satellites also use the old microwave interferometer system as well, in case the laser ranging experiment (which is the first of its kind) should fail. (NASA/JPL-Caltech 2018), (Ingalls 2018).

6 Discussion

In this section, the results are shortly summarized, interpreted and discussed in terms of their meaning, what they might imply for the future, and what benefits for their respective areas of science they might contribute to.

6.1 Global Analysis

For the global analysis, it was seen that by far the most significant signal of short-time mass changes on the Earth came from the melting of ice in the Arctic regions and Antarctic regions. This signal was so powerful that it made up 63% of all the variance in the global principal component analysis. Following this was the signal from the large-scale water oscillations in the Amazon rainforest area, making up 7.87% of the total variance.

The velocity and acceleration parameters helped pinpoint where on Earth the large-scale melt-off trends are happening, and which areas to consider for the smaller, regional analyses. The findings for the various areas of interest are discussed below.

6.2 Regional Analyses discussion

In the regional analyses, the full regression model, phase, and amplitude constants, as well as a principal component analysis, was made, similarly to the global analysis. However, it was only made for the chosen mask area itself, which filtered out all other noise from other areas on the globe, so the important and interesting patterns of these chosen regions stood out clearly.

6.2.1 Greenland regional analysis discussion

In Greenland, a large magnitude of ice melt off, up to almost 600 gigatons between September 2011 and September 2012, was observed. This ice melt off was a trend that was still accelerating as of the 15th of June 2016 for south-western Greenland, but it seemed to be decelerating for south-eastern Greenland. What this implies is that the data for the ice loss observed in Greenland with GRACE is consistent with other scientific reports of ice loss in the region during 2002 and 2016 (Scambos and Koenig 2013), (Rodell 2018). If this trend continues, it can lead to dire consequences for humanity as well as Earth's ecosystem. For example, polar bears will likely go extinct due to their large dependence on the Arctic ice sheets and sea ice. Global sea levels will rise, with 365 gigatons of water contributing to about 1-millimeter increase in global sea levels (Boening 2014). Some scientists even argue that the vast amounts of freshwater from Greenlands ice sheets pouring into the Atlantic ocean could disrupt and weaken the Gulf Stream as well as other Atlantic ocean currents, which transport large amounts of heat north from the equator to the poles (Rahmstorf et al. 2015).

When ice melts on Greenland, a lot of mass disappears from this area. This loss of mass in the area means that there will be less gravity to "pull" in the water around this region. As a consequence of this, the water will then seek towards other land masses, until a balance is restored between the gravitational forces on land masses, ice, and water. What this means is that a relatively larger portion of the displaced water will seek towards the southern hemisphere, and cause the sea levels to rise here instead of at the northern hemisphere. So the ice melting in Greenland will barely be felt in the northern hemisphere, regarding increases in sea-level. The opposite effect occurs when ice melts in Antarctica (Quoted and translated from (M. G. Andersen 2018)).

6.2.2 Western Antarctica regional analysis discussion

For western Antarctica, a sizeable melt-off trend was observed at the Pine Island Bay, which was still accelerating overall, but decelerating around Larsen's Ice shelf and the tip of the Antarctic peninsula. Additionally, an ice-melt off trend of varying magnitude was observed through the years, peaking at around 2010-2012 with ice melt-offs larger than 300 Gt/yr during some periods. However, this melt-off of western Antarctica was largely counterbalanced by the increase of ice masses on eastern Antarctica.

What this might imply is that the tendency of the Antarctic ice melt-off regions is not as dramatic as one would have thought, being only around 80-110 Gt/yr, because of the countering effect from the ice gain at eastern Antarctica. It is still a lot of ice, however. In a recently published article in Nature (team 2018), it was determined that ice loss from Antarctica have contributed to a global increase in mean sea level of 7.6 ± 3.9 [mm], equivalent to $2,720 \pm 1,390$ billion tonnes of ice between 1992 and 2017. It also shows that during the course of five years, the ice-melt off rates have tripled, between 2012 and 2017, measuring about 219 gigatons of ice loss annually over this period. Comparing with the estimates of ice loss in this report for western Antarctica, seen in figure 40, this scale of ice loss fits well with the findings of the article published in Nature (M. G. Andersen 2018). Additionally, as stated in the subsection above for Greenland, the ice that melts in Antarctica will cause larger sea level increases in the northern hemisphere, and barely any in the southern hemisphere. Considering that the vast majority of the habitable landmass on Earth is in the northern hemisphere, this could lead to massive damage to infrastructure, mass evacuations and many other consequences in the future, because of permanent flooding in large coastal cities for example, such as New York and Miami, Shanghai, London, Amsterdam etc.

6.3 Alaska regional analysis discussion

Interestingly for Alaska, it is the only region to have its largest observed melt-off in the start of the measuring period, between September 2003 to September 2004. It seems to slow down significantly after this point, except for a spike between September 2012 and September 2013. However, this was right after an *increase* in mass for the area of about 60 gigatons between 2011 and 2012, so it could just be the landscape adjusting to the sudden increase in ice the previous year.

Looking at the velocity and acceleration parameters, the tendency of ice melting is strongly decelerating around central southern Alaska, and also overall for the Alaska mainland. However, it is still accelerating in south-eastern Alaska, meaning that if the trend continues past the measurement date of GRACE, climate scientists should keep an eye on this area. Finally, overall there is an annual loss of ice in this region, that seemed to start accelerating around 2008 (as seen in the eigenvector for the first principal component in the appendix, 44). This is most likely because the signal of the melting ice in south-eastern Alaska outweighs the increase in ice in Alaska's other regions. And like Greenland, the ice melt-off of Alaska will also cause an increase of sea levels mostly in the southern hemisphere.

6.4 Amazon Rainforest regional analysis discussion

The Amazon Rainforest has the most substantial oscillation of water mass on the planet, which is why its signal is so visible in the data, and why it makes up for such a large percentage of the total variance in the global principal component analysis. The peak of the rainy season changes depending on the geographical location, but for the Amazon river area, it seems to peak in May, while it peaks earlier in the year for the southern area and later for the northern area.

From the analysis of a single grid point's oscillation, it was seen that there was a significant offset of the phase between the annual oscillation signal and the model as a whole. This was caused by the half-annual and $\frac{1}{3}$ annual oscillations also having a significant impact on the model here. Also, this region was the one that had the highest RMSE-values (standard deviations of the residuals), meaning it was here the model was worst at predicting the EWH-values. This might be because the model needs to include additional oscillation parameters to work optimally here, such as the $\frac{1}{4}$ annual oscillation for example.

The findings of this regional analysis can be useful for many things. For example, the farmers inhabiting this area can use these phase differences to determine when it is best to sow seed, to harvest, and many other things, based on the knowledge of when the rainy season will start each year, in the different areas. The findings might also be used to improve weather forecasts and climate-scientists understanding of different scientific phenomena here, such as the effect of PDO (Pacific Decadal Oscillation), El Nino and others.

6.5 Caspian Sea regional analysis discussion

The water levels in the Caspian Sea have been dropping steadily for a long time now. As seen in the analysis done here, and also in other scientific papers, e.g. Chen et al. 2017a, this is a trend that is accelerating dramatically over the period, especially increasing at around 2010 as seen on figure 56. It is believed by scientists that the primary cause of the water loss is caused by increased evaporation, along with a decreased precipitation and river runoff from the Volga river. If this trend of accelerating water loss continues, the Caspian Sea might end up suffering the same fate as the Aral Sea, which went from being the 4th largest lake in the world to being almost completely dried out today, leaving only a desert behind. The drying out and desertification of the Aral Sea resulted in many serious consequences, such as the extinction of more than 20 different fish species, large amounts of pollution, water shortage, loss of jobs due to the destruction of the local fishing industry in the area, and much more (Turid Austin Wæhler 2017). If such a thing were to happen to the Caspian Sea, the consequences would be disastrous

6.6 The Himalayas and the Tibetan Plateau regional analysis discussion

In the Tibetan Plateau and Himalayan regional analysis, the main thing to take note of was the change in the water-mass balance between the two vastly different regions of the Himalayas and the Tibetan Plateau. This contrast was interesting because of their proximity to each other. The water levels in the Tibetan Plateau is largely influenced by the amount of evaporation in the Himalayan mountain ranges.

From the principal component analysis of the region, a change in what was likely the snow-water storage in the region was seen in the eigenvector belonging to the first principal component. Consistent with other scientific articles, e.g. (Rodell 2018), this could be explained by a trend of overall groundwater depletion, water depletion and precipitation decrease of the Himalayan mountains. The increase in water levels across the Tibetan plateau was likely due to increased precipitation coming from the Himalayas, but overall the region seemed to be losing water over time. The plot of the total mass-loss over time supported this claim, as seen in figure 64, where a clear, declining trend in water-mass was seen over time.

What the findings from this regional analysis might imply is that the people of the Tibetan Plateau will experience more rainfall and increased water levels in their rivers and lakes, thus potentially boosting the agriculture in the area. It also shows the effects of global warming on the Himalayas, an area that is neither in the arctic or antarctic regions but is still experiencing large-scale melt of its stored snow and ice. The increased precipitation from the Himalayas will not only affect the Tibetan Plateau but likely the entire area around the Himalayas, which is a significant part of Asia and south-east Asia.

6.7 Sumatra and Fukushima regional analyses discussion

In this region, the earthquakes of Sumatra in 2004 and 2012, as well as the earthquake in Fukushima, 2011, were analyzed. The GRACE satellites are capable of picking up on the signals of earthquakes very clearly, because of their ability to detect large-scale gravity changes over short time periods. When drawing a mask around Sumatra or Fukushima, a very large spike is seen right at the occurrence of these earthquakes. In the analyses, it was deduced that the type of earthquake could make a difference to the magnitude of the "spike". For example, subduction megathrust earthquakes, such as the Sumatra 2004 or Fukushima 2011 earthquakes, causes a very large spike in the EWH-data. However, a strike-slip earthquake, such as the 2012 Sumatra earthquake, causes a much smaller spike. This is because of the way the tectonic plates interacts during an earthquake. In a subduction earthquake, much more mass is moving and being displaced relative to each plate than for a strike-slip earthquake, which is characterized by a more horizontal plate movement.

Also, the movement of the tectonic plates themselves could be seen quite clearly in the spatial pattern of the principal component analysis. This was seen by a clear contrast between the sign of the weights located on each plate. A similar thing was seen for the Fukushima tectonic plate movement.

Using this knowledge, it might be possible for geophysicists in the future to more accurately track and study earthquakes and the movement of tectonic plates. Also, now that the GRACE Follow-on mission is underway, this kind of gravitational data can be tracked much more precisely. Only time will tell what potential breakthroughs this could enable in the future.

6.8 Uncertainties and limitations in the data

While the measuring method used by the GRACE satellites was groundbreaking in its own right, it still had some limitations. For example, the 400 [km] measuring resolution led to significant errors, especially at great northern or southern extents, due to the longitude points lying too close to each other and as such being oversampled. This could be roughly correlated for by accounting for the decreasing area of the grid points when moving away north or southwards, but it was not a perfect solution since the measured EWH values were still oversampled. This problem seems to have been vastly improved for the future Grace Follow-on mission, which has a much more precise measuring ability, due to its updated hardware and software. This will allow it to measure the gravity field with much smaller errors.

6.9 Future work

Due to the limiting scope of this project, there was only room for a light analysis of the seven chosen regional areas as well as the global analysis, using the statistical tools of regression analysis and principal component analysis. If more time was given, the chosen areas could have been examined in more detail.

For the Arctic and Antarctic areas, the various areas that experienced either a gain or a loss in mass could have been analyzed separately, to improve insight into what is happening here. For the Amazon Rainforest, the secondary and third principal components could have been interpreted on a deeper geophysical level, to understand the cause behind the observed 11-year cycle in the second principal component, for example. For the Caspian Sea, the various effects causing the decline could have been separated and studied on their own, as was done in the article by Chen et al. 2017a. For example, how much of the decline of the sea does the increased evaporation contribute to? And what about the decreased precipitation? For the Tibetan Plateau and Himalaya regions, the two regions could have been separated and studied on their own, and perhaps a model for the correlation between water increase in the Tibetan Plateau, and increased evaporation in the Himalayas, could have been deduced. Finally, for Sumatra

and Fukushima, a deeper geophysical analysis of the tectonic plate movements, earthquakes, and other relevant factors could have been made.

Apart from a deeper analysis of the chosen regions, it would also have been interesting to examine other relevant regions identified in the model for Terrestrial Water Storage seen in figure 25. Relevant regions that were originally considered but omitted in this report include the Central African rainforest, the Murray Darling basin in south-eastern Australia, the decline of the Aral Sea, the Three Gorges and other reservoirs filling in western China, as well as the precipitation increase and groundwater policy change in Northern India.

The launch of the GRACE Follow-on mission will start measuring from where the original GRACE satellites left off, despite a gap of about 1-2 years in the data that is useful (GRACE began measuring poorly towards the end of its operating period). The greatly increased accuracy of GRACE-Follow on will allow for a much better analysis on the topics covered in this project, as well as many others. The first published and processed GRACE Follow-on data is expected to be published in the summer of 2018.

7 Conclusion

The purpose of this project hsa been to analyze and interpret the data from the GRACE satellites, by using regression analysis and principal component analysis methods.

In the present project, a global analysis of the Earth has been made, based on the global gravitational data from the GRACE satellites. This analysis includes a regression analysis, followed by a determination of the phase and amplitude constants, which expresses when the rainy season peaks for different areas, and the magnitude of the annual oscillation of rainfall. The velocity and acceleration parameters from the regression model was used to give further insight into what is happening in the different parts of the world, in regards to the rate at which water is being redistributed. Following this, the precision of the models and parameters was analyzed using P-values and a Root-Mean-Square error estimate. And finally, a singular value decomposition of the array of data values followed by a principal component analysis was done.

The entire global analysis expressed that the far strongest signal observed was the melt-off of ice in Greenland, Antarctica and Alaska. The second strongest signal was the large oscillation of water masses in the Amazon Rainforest, and other rainforest areas in for example Africa and south-eastern Asia. Finally, the third strongest signal, which was also predominantly observed in the Amazon rainforest, featured a mysterious 11-year cycle of oscillation. In the report, no conclusions or assumptions were made on what caused it, but it was reasoned that it might be explained by either variations in the 11-year cycle of sunspot activity in the sun, or the Pacific Decadal Oscillation climate variability. However, nothing was concluded with certainty here, as it was outside the scope of this project.

After the global analysis, a regional analysis was carried out for 7 different, chosen regions: Greenland, western Antarctica, Alaska, the Amazon Rainforest, the Caspian Sea, the Tibetan Plateau and Himalaya mountain ranges, aswell as that of Sumatra and Fukushima. The regions that were chosen was largely inspired by a figure in an article published in Nature in 2018, aswell as the signals that were seen in various places in the plotted EWH data for the global analysis. The same analysis was done for these chosen regions as was done for the global analysis, to really focus on what was happening without the noise and disturbance of the rest of the world.

For Greenland, Antarctica and Alaska, it was concluded that there has been a large signal of accelerating ice-loss during the period of the GRACE satellites' operation, which was largely human-influenced. The geographical areas that experienced melt-off of ice saw a

change in acceleration over time, as seen in the second-largest principal components. Finally, the magnitude of ice-loss over the time period was estimated and plotted.

For the mask of the Amazon Rainforest, it was deduced that the magnitude of its global signal could be explained by its large annual oscillation in water masses. And that different areas in this region have their rainy seasons at different times, based on the phase plot. Furthermore, there was a large contribution in the signal from both the annual, half-annual and $\frac{1}{3}$ annual oscillation.

For the Caspian Sea, the decline of its water levels was examined over the timeperiod, as it had been reported to be losing water at an accelerating rate. This was likely caused by an increased evaporation aswell as a decreased precipitation and decreased river runoff from the Volga river. The findings confirmed the reported assumptions, and was consistent with the findings of other scientific articles.

For the Himalayas and Tibetan Plateau, the change in mass-distribution was examined for a mask that covered several large, very different geophysical phenomenons. The Tibetan Plateau for one is a dry, barren area with little water. The Himalayas in contrast contains vast amounts of ice and snow, which melts and evaporates each summer leading to huge monsoons and increases in river-runoffs to most of eastern and south-eastern Asia. In the spatial pattern, a clear contrast was seen between the mountain ridge and the Tibetan Plateau. From the findings of the largest principal component, it was argued that the Himalayas were losing water and groundwater due to an increase in evaporation, and that in turn, this water was being redistributed across the Tibetan Plateau, which then saw an increase in the water levels of its lakes and rivers. From the second largest principal component, a large difference in the weights between the geographical area of Jammun and Kashmir in northern India and the Himalayan mountains was seen. And it was concluded that this difference could be explained by the difference in when each area experienced the peak of its rainy season (April-May for Jammun-Kashmir and August-September for the Himalayas). Finally, it was determined that the region as a whole was losing water at an increasing rate over time, due to "warming-enhanced evaporation and glacier melt-off" caused by global warming, the magnitude of which was so large that it likely exceeded the surface water gains in the Tibetan Plateau. But it was also noted that nothing could be stated with certainty in regards to the water loss observed here.

In the last regional analysis, the earthquakes in Sumatra and Fukushima were examined. The GRACE satellites' ability to detect changes in mass over small time-periods were unprecedented, so they picked up these signals very clearly. Drawing a mask of the areas around Sumatra, the movement of the tectonic plates became quite visible in the spatial pattern, as one could visually see the Burma plate subducting the Indian plate during the 2004 earthquake. Additionally, the fault type of the earthquake and its magnitude seemed to make a big difference in regards to the magnitude of the signal, as seen in the second principal component of the Sumatra regional analysis. Furthermore, to examine the strength and propagation of the signals from the two earthquakes, 2 different points in the Sumatra region were chosen and plotted. One was in the epicenter of the 2012 earthquake, where the 2012 earthquake was quite visible. The other was 249 [km] away, where the 2004 earthquake was still very visible, but the 2012 earthquake was not. This proved in part just how much more powerful the 2004 earthquake was than the 2012 earthquake.

As written in the Discussion chapter, the findings of the results section are useful for many different areas of science, and for many different people in the world. It may help farmers determine when to place their crops, or the people living close to fault-lines know what to expect from the next earthquake. Climate scientists will be able to improve their models based on GRACE data, and future weather forecasts may also be improved. In conclusion, the uses of the GRACE data is numerous and important in many different areas, as has been demonstrated throughout this project.

8 Appendix

A Principal component 1 and its eigenvector for Alaska

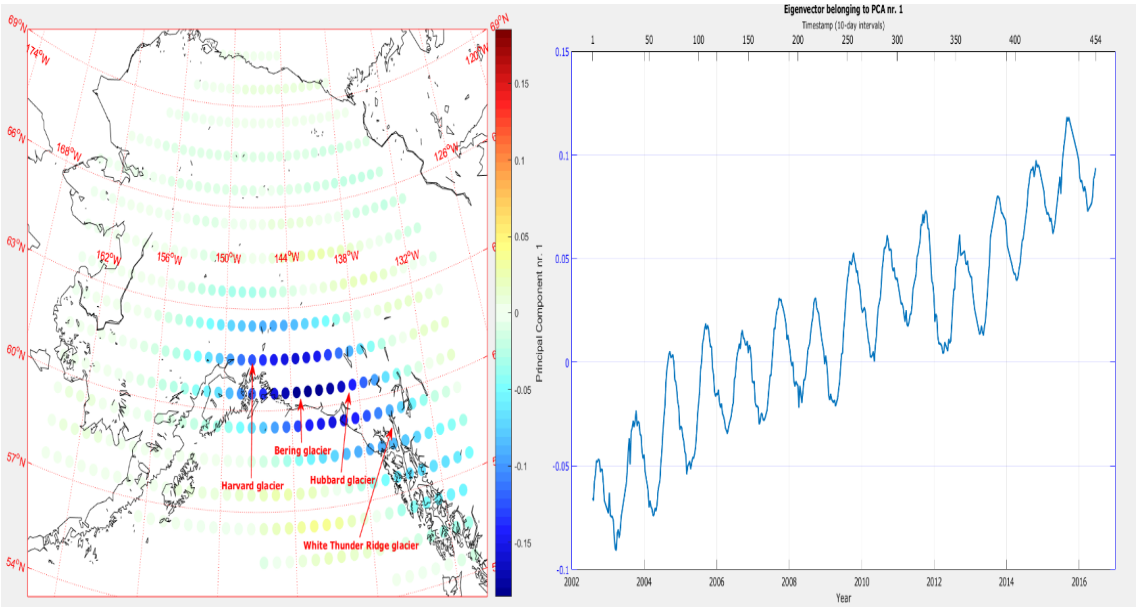

Figure 76: Principal component 1 for Alaska

B Strength of the mantle and various materials

The top and most solid of the mantle is known as the Lithosphere. It lies just above the Asthenosphere, and makes out the middle of the mantle. These two mantle parts have vastly different viscosities (a measure of a fluids resistance to gradual deformation by either tensile stress or shear stress), and hence reacts differently to the loading of the ice. Since the Lithosphere is solid and stiff, it will bend down in the same way as if one presses down on the middle of a ruler. The Asthenosphere however is more soft and plastic, and will be pushed away to the sides as the Lithosphere is pressed down. Table 6.2 portrays the distribution of viscosities in the Lithosphere aswell as the Asthenosphere, depending on the depth.

During the Glacial Isostatic Adjustment, at some point, an equilibrium will be reached in the Asthenosphere, between the weight pressing it down and the force which is pushing the material to the side. This equilibrium disappears when the ice melts away, because the loading on top will become smaller. The Asthenosphere will then attempt to pull itself back to its original, pre-Glacial Maximum shape, by pushing the Lithosphere back upwards.

6-10 POSTGLACIAL REBOUND 241

TABLE 6-2 **Distribution of Viscosity in the Mantle from Postglacial Rebound Studies**

Region	Depth (km)	Dynamic Viscosity (Pa s)
Lithosphere	0–100	Elastic
Asthenosphere	100–175	4×10^{19}
	175–2848	10^{21}

Figure 77 shows how an ice

glacier is loading on a surface, and how it reacts after the ice has melted away. It is the period between c) and d) which takes many thousands of years.

Elasticity vs. Plasticity

There are 2 very important physics concepts which describe the properties of materials aswell as their responses to deformation (See figure 78.

Elasticity:

This concept describes a physical materials ability to resist deformation when it is impacted by external forces, and its ability to return to its original shape after the external forces are removed.

Plasticity

Describes the deformation of a material, which is non-reversible and permanent. A good example of this phenomenon is when a hard metal, such as steel, is beaten into new shapes and purposes.

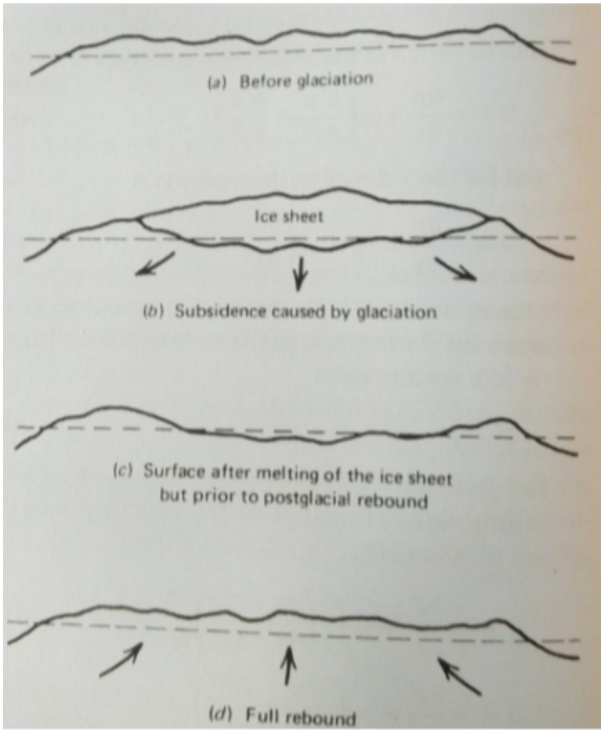

Figure 77: Mantle response to ice loading

Yield and Tensile Strength

The boundary which lies between when a material moves from being Elastic to Plastic is denoted as its *Yield Stress*. After a material is subjected for this or a larger amount of stress, it will be undergo a plastic deformation. Materials which are subjected to a plastic deformation is also known as *ductile mateirals*. Copper is a good example of such a material.
Finally, *Tensile Strength* is a materials maximum boundary for stress or strain, before it breaks completely and is destroyed. A good example of such a material that typically behaves this way is Iron or Concrete.

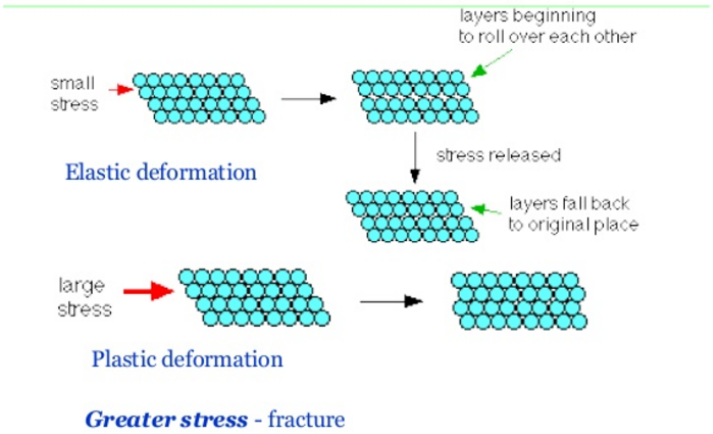

Figure 78: Elastic vs. Plastic deformations

Elasticity in itself is an ideal concept. No materials exists which are perfectly elastic. This means that **all** materials will, at some point when enough stress or strain has been induced upon them, become plastic and be deformed permanently, or break and be destroyed.

Elastic Deformation

Elastic deformation is an almost instantaneous effect, which happens over a couple of days or less. It arises due to the Lithosphere being elastic and stiff, and therefore bending like a ruler when subjected to stress. If the stress then disappears, it will "jump back" to its original shape. This is what is observed when glaciers melt on Greenland, where the mantle is rising proportional to the melt-off of ice.

The above mentioned conclusions indicate that the Lithosphere in itself has a final amount of yield stress it can withstand, and in theory is capable of being deformed permanently. But this threshold would require a massive amount of force to reach, which not even the heavy glaciers of the last Glacial Maximum could provide (but a good example of such a force is meteor craters, such as the Chicxulub Crater that killed probably killed off the dinosaus, found in the Yucatán Peninsula of Mexico).

C A short introduction to earthquakes and plate tectonics

90 % of earthquakes arise from tectonic events, and in most cases from movements on faults. (A *fault* is a fracture of a volume of rock, resulting from a large displacement due to rock-mass movements, usually due to tectonic plate forces and active plate boundaries. A *fault plane* represents the fractured surface of this deformation.)

The remaining 10% arise from volcanism, subterranean cavities or from man-made events, like coal mining or drilling (Fundamentals of Geophysics).
The *Elastic Rebound Model* depicts the way an earthquake typically may occur. It is illustrated below in the far left side of figure 65, along with the three different types of faulting an earthquake can have, and the three types of tectonic plate boundaries that exist.

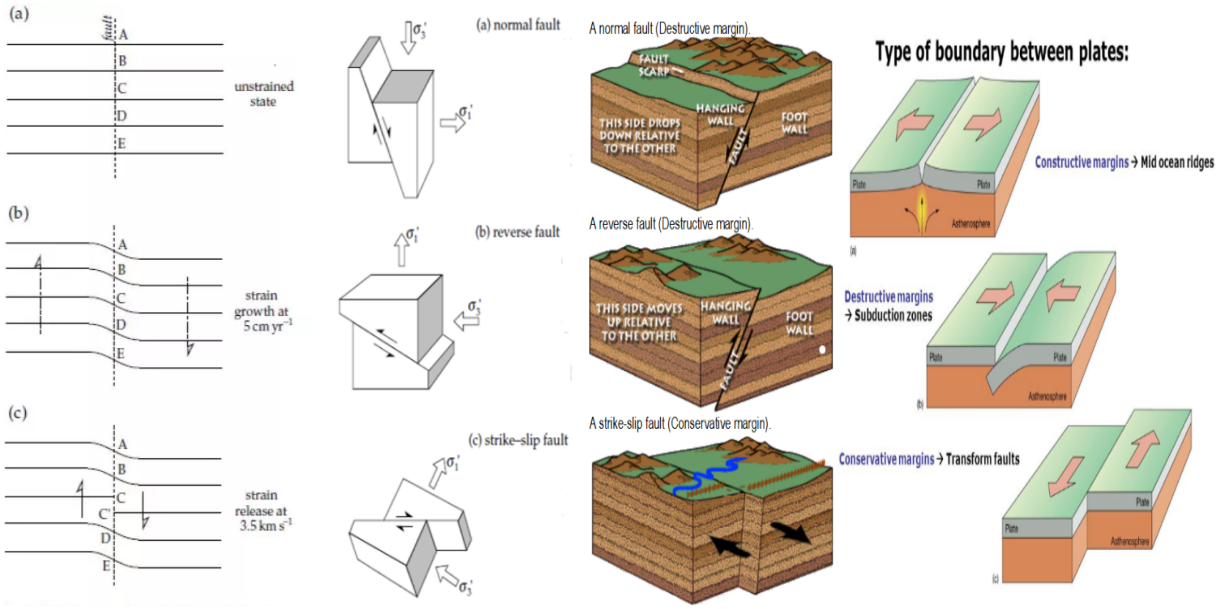

Figure 79: Earthquakes, fault types and plate boundaries.

(U. S. G. Survey 2017) (Fundamentals of Geophysics)
When 2 tectonic plates meet, they will "rub against each other", thus building up tension over many years. The stress or strain between the plates will continue to build up and accumulate until it exceeds the *yield stress* of the tectonic plate (the maximum amount of elastic deformation a material can withstand) (see also section 5 for further elaboration). When this breaking point is exceeded, the rupture occurs and a violent displacement along the fault-plane will happen. During this event, all the stored potential energy between the plates, which have been accumulating over many years, will be released in a couple of seconds as a *shock wave*. The magnitude of the resulting earthquake will depend on the length of the activated fault-plane.

There are three ways tectonic plates may interact with each other, which may be described by their *tectonic fault* type, and their plate boundary type. (see figure 79).

When the movement of the tectonic plates appear up or down the fault plane, it is called a *dip-slip fault*. And when the movement is horizontal, parallel to the strike of the fault, it is called a *strike-slip fault*. There are 2 types of *dip-slip faults*. (a): For the normal fault, one tectonic plate drops down an inclined plane relative to the other tectonic plate. (b): For the *reverse fault* or *thrust fault*, the tectonic plate on the upper side of the fault moves upwards along the fault-plane, overriding the underlying tectonic plate (Fundamentals of Geophysics). Finally, there are 3 distinct categories of plate boundaries: *Conservative, Constructive* and *Destructive plate boundaries* (See figure 65).

For *Constructive plate boundaries*, the tectonic plates moves in opposite directions, away from a mid-oceanic ridge. A *Conservative plate boundary* is when plates slide past each other, creating friction. This friction will build up potential energy over time, which will eventually be released all at once, when a threshold is reached (The San Andreas fault or the 2012-Sumatra earthquake is good examples of strike-slip fault type areas). Finally, the *Destructive Plate Boundary* is when two tectonic plates moves directly into each other, colliding. This will eventually cause the lightest of the two plates to slide over on top of the other, forcing the heavier plate down deep into the mantle of the Earth, where it will eventually be melted down and destroyed. This is also known as a *subduction zone*, and are the type of plate boundaries that causes the most disastrous and damaging types of earthquakes. For example, this is what happened in the 2004 Sumatra-Andaman megathrust earthquake, where the Indian tectonic plate was subducted by the Burma tectonic plate, resulting in a tsunami that killed 230,000-280,000 people. And the 2011 Fukushima earthquake was also this type of a subductive megathrust earthquake (Fundamentals of Geophysics).

Even though the 2004 Boxing day tsunami and 2011 Fukushima tsunami were among the deadliest and most destructive in history, the 2012-Sumatra earthquake, despite being one of the most powerful of its kind ever recorded, caused very little damage in comparison. The reason for this was that it was a strike-slip type of earthquake, characterized by a more lateral kind of movement than an upward-downwards kind of movement. It is the upward-downwards kind of movement of the megathrust earthquakes that create the deadly tsunamis, because the upwards motion creates a large disturbance in the water. But the horizontal motion of the strike-slip fault type doesn't disturb the water as much, since there is barely any uplift of the ocean floor. This is the reason why it wasn't as destructive (Fundamentals of Geophysics; Interior and U. G. Survey 2006; Program 2018; Stein and Okal 2005; California - Berkeley 2012).

D Regional Analysis appendices

D.1 Greenland regional analysis

Coordinates of notable places:

1. **City of Nuuk**: 64.175**N**, 51.739**W**
2. **Jacobshavn outlet glacier**: 69.17**N** 49.8**W**
3. **Helheim outlet glacier**: 66.35**N**, 38.2**W**
4. **Kangerdlugssuaq outlet glacier**: 68.633**N**, 33**W**
5. **Garm outlet glacier**: 63.5**N** 42.29**W**

Timestamps used for measuring total ice loss each year in Greenland:

```
total_mass{5,:}; % 7 Sep - 2002
total_mass{34,:}; % 2 Sep - 2003
total_mass{70,:}; %06 Sep - 2004
total_mass{106,:}; %01 Sep - 2005
total_mass{143,:}; %06 Sep - 2006
total_mass{179,:}; %01 Sep - 2007
total_mass{216,:}; %05 Sep - 2008
total_mass{252,:}; %31 Aug - 2009
total_mass{289,:}; %05 Sep - 2010
total_mass{320,:}; %31 Aug - 2011
total_mass{353,:}; %04 Sep- 2012
total_mass{380,:}; %29 Sep - 2013
total_mass{407,:}; %04 Sep - 2014
```

Figure 80: Timestamps used for when measuring total ice loss in Greenland

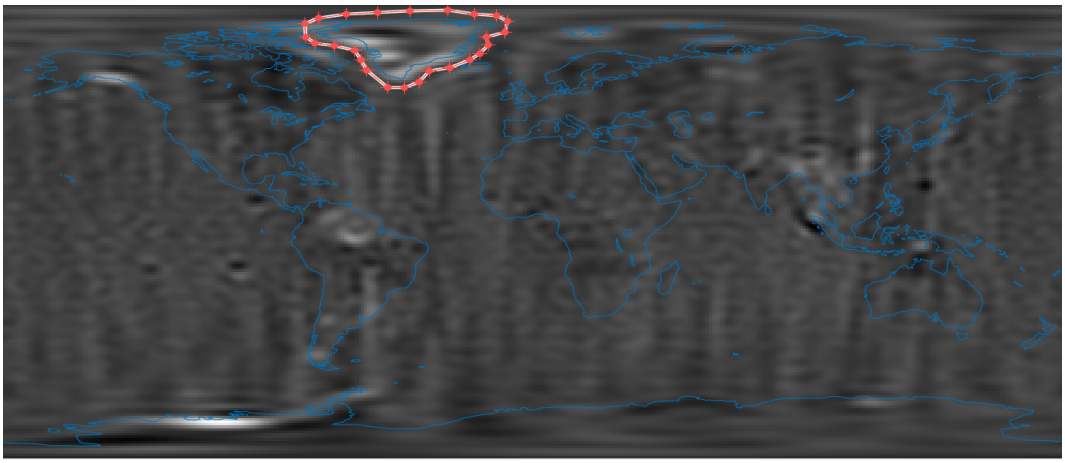

Figure 81: Mask area for Greenland

D.2 Antarctica regional analysis

Coordinates of notable places:

1. **Thwaites glacier**: 75.5**S**, 106.75**W**
2. **Larsen C**: 67.5**S**, 62.5**W**
3. **Pine island glacier**: 75.17**S**, 100**W**

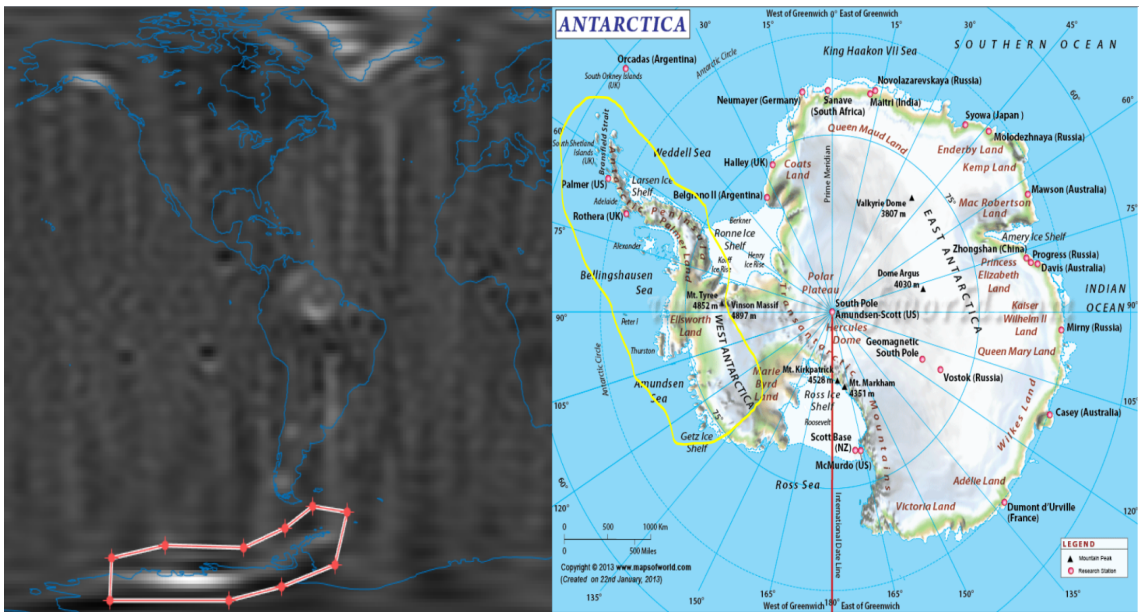

Figure 82: Antarctica map and its mask area (yellow polygon region in the right figure illustrates the mask area)

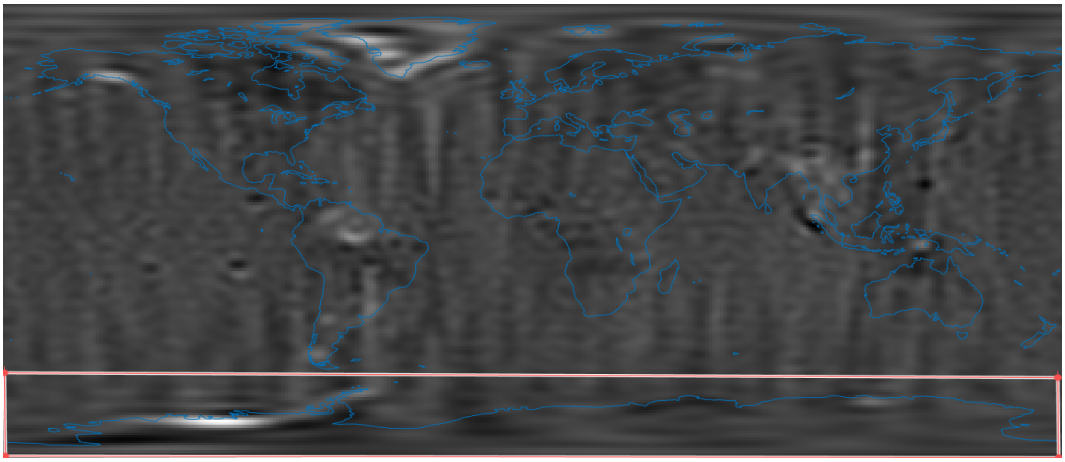

Figure 83: All of Antarctica mask - (red rectangle in the bottom denotes the mask area)

```
total_mass{20,:}; % 06 Mar - 2003
total_mass{52,:}; % 10 Mar - 2004
total_mass{88,:}; %05 Mar - 2005
total_mass{125,:}; %10 Mar - 2006
total_mass{161,:}; %05 Mar - 2007
total_mass{198,:}; %09 Mar - 2008
total_mass{234,:}; %04 Mar - 2009
total_mass{271,:}; %09 Mar - 2010
total_mass{304,:}; %04 Mar - 2011
total_mass{337,:}; %08 Mar - 2012
total_mass{367,:}; %21 Feb - 2013
total_mass{392,:}; %08 Mar - 2014
total_mass{421,:}; %03 Mar - 2015
total_mass{447,:}; %07 Mar - 2016
```

Figure 84: Timestamps for Antarctica ice loss, March 2003 to March 2016

D.3 Alaska regional analysis

Coordinates of notable places:

1. **White Thunder Ridge**: 59.03**N**, 136.19**W**
2. **Hubbard glacier**: 60.31**N** 139.37**W**
3. **Harvard glacier**: 61.39**N**, 147.44**W**
4. **Bering glacier**: 60.30**N**, 143.42**W**

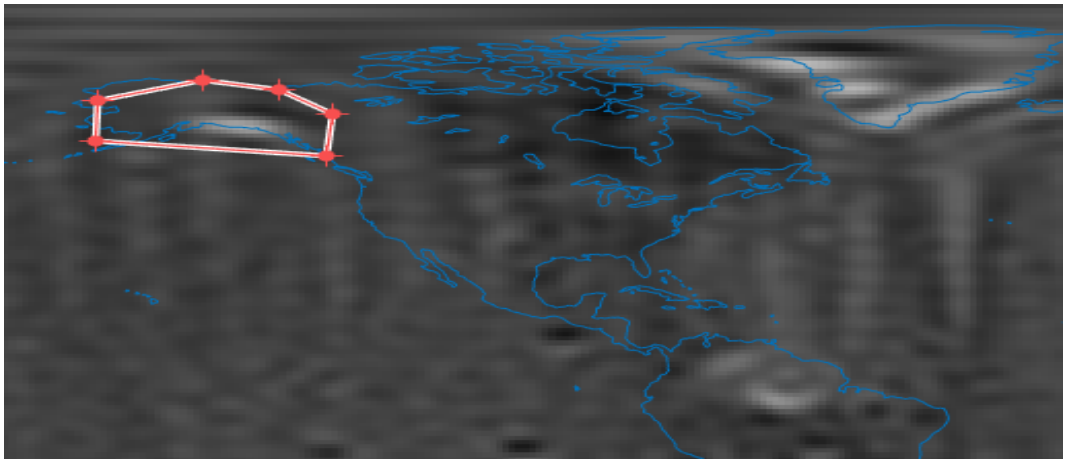

Figure 85: Mask area for Alaska

D.4 Amazon regional analysis

Coordinates of notable places:

1. **City of Rio de Janeiro**: 22.93**S**, 43.23**W**
2. **Island of Trinidad and Tobago** 10.33**N**, 61.22**W**
3. **Amazon River mouth** 0.06**N**, 50.39**W**

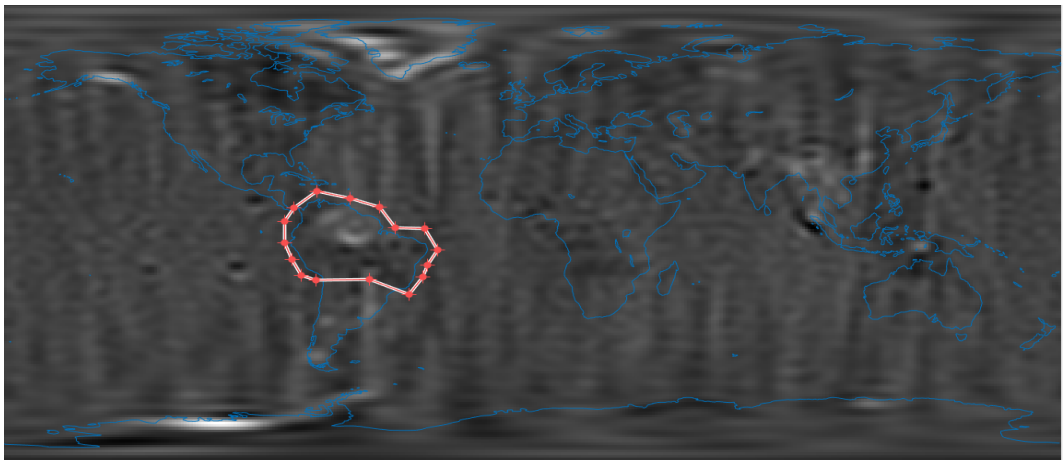

Figure 86: Amazon chosen mask

D.5 Caspian Sea regional analysis

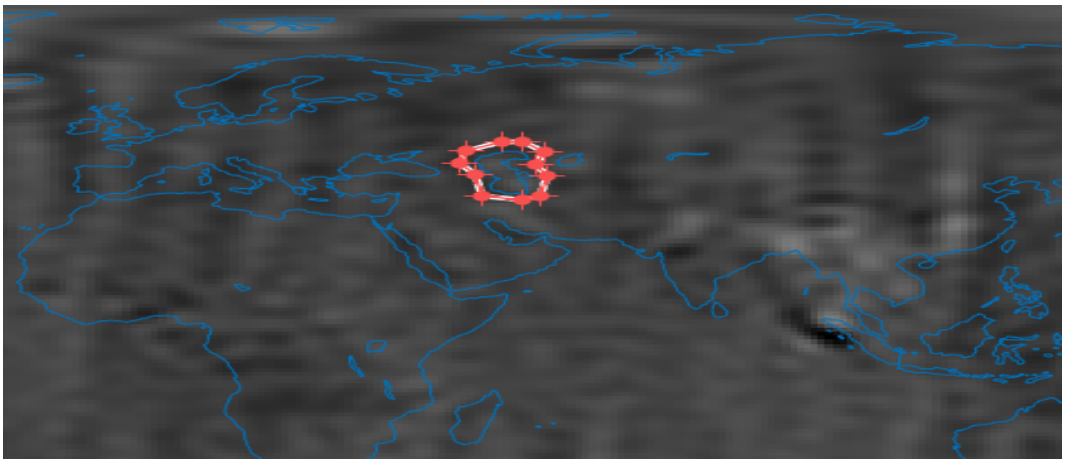

Figure 87: Caspian Sea mask area

D.6 Tibet and Himalaya regional analysis

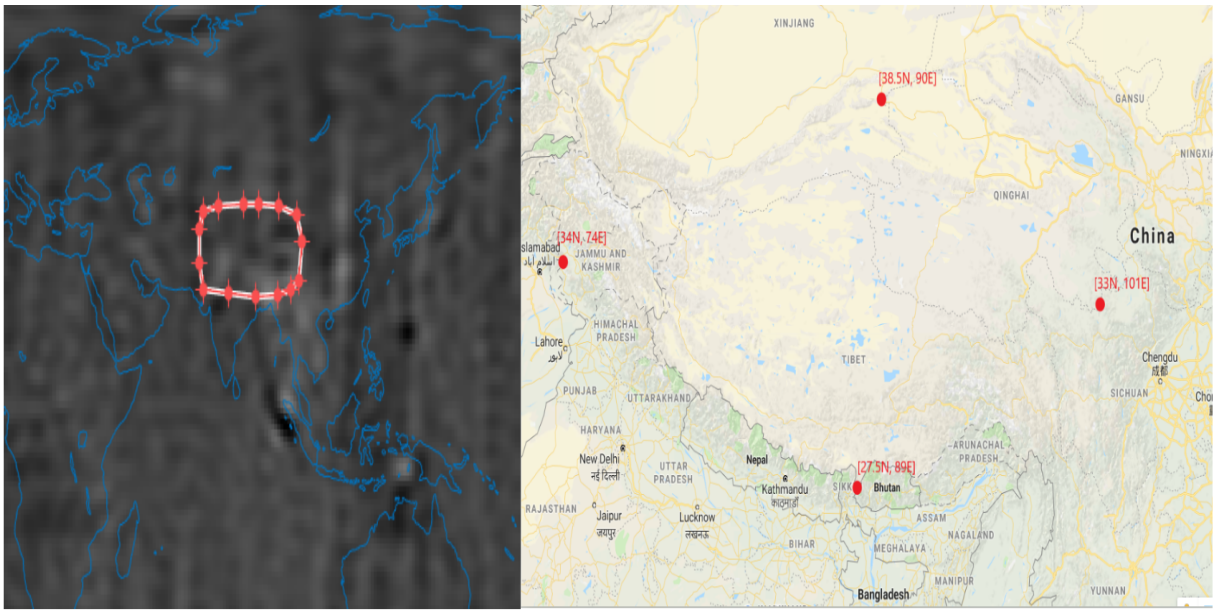

Figure 88: Himalaya and Tibetan Plateau chosen mask, with google maps comparison

Comparing the longitude and latitude extremes with google maps, it can be seen that these longitude and latitude spans roughly fit the area of the Tibetan Plateau and the Himalayas. (see figure 88).

D.7 Sumatra regional analysis

Coordinates of notable places:

1. **Sumatra 2004 quake epicenter**: 95.854**E**, 3.316**N**
2. **Sumatra 2012 quake epicenter**: 93.063**E**, 2.311**N**

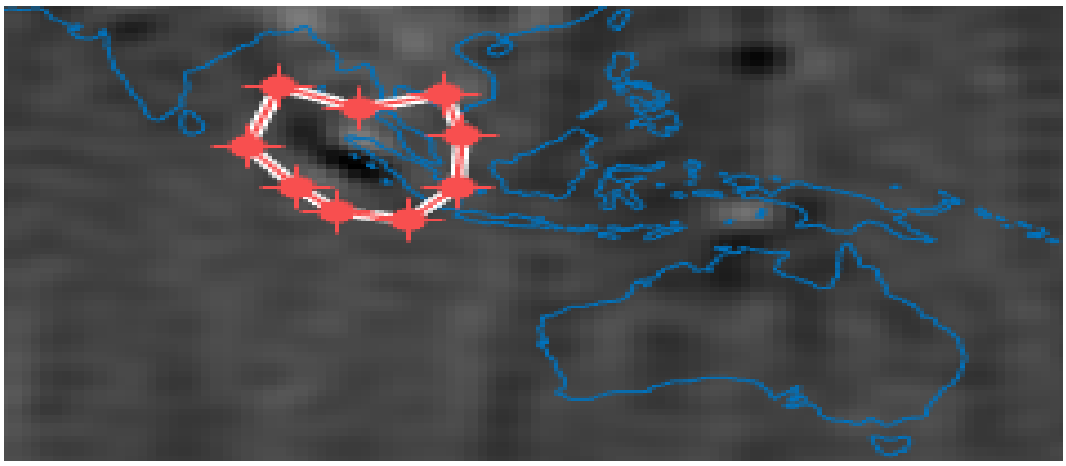

Figure 89: Zoomed-in mask area around Sumatra

D.8 Fukushima regional analysis

Coordinates of notable places:

1. **Fukushima 2011 quake epicenter**: 142.369**E**, 38.322**N**

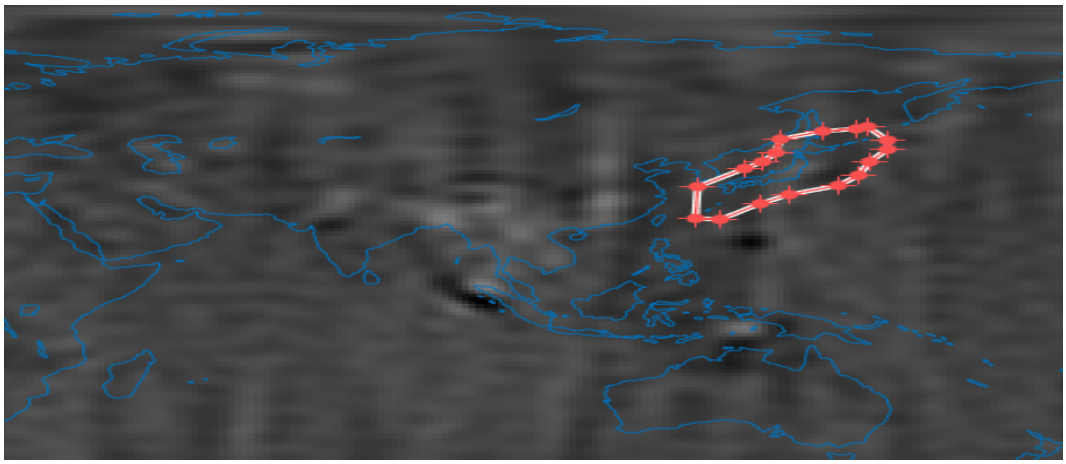

Figure 90: Chosen mask area around Fukushima

9 References

Scientific papers:

Stein, Seth and Emile A. Okal (2005). "The 2004 Sumatra earthquake and Indian Ocean tsunami: What happened and why?" English (US). In: *Visual Geosciences* 10.1, pp. 21–26. ISSN: 1610-2924. DOI: 10.1007/s10069-005-0025-x.

Rahmstorf, Stefan et al. (2015). "[Exceptional twentieth-century slowdown in Atlantic Ocean overturning circulation]". In: *Nature* 5, pp. 475–480. DOI: 10.1038/nclimate2554.

Chen, J. L. et al. (2017a). "[Long-term Caspian Sea level change]". In: *Geophysical Research Letters* 44.13, pp. 6993–7001. DOI: 10.1002/2017GL073958.

— (2017b). "[Points of Significance: Principal component analysis]". In: *Nature* 14.7, pp. 641–642. DOI: 10.1038/nmeth.4346.

Forsberg, R. et al. (2017). "[Greenland and Antarctica Ice Sheet Mass Changes and Effects on Global Sea Level]". In: *Surveys in Geophysics* 38.1, pp. 89–104. DOI: 10.1007/s10712-016-9398-7.

Rodell, M. (2018). "[Emerging trends in global freshwater availability]". In: *Nature* 557.7705, pp. 651–659. DOI: 10.1038/s41586-018-0123-1.

team, The IMBIE (2018). "[Mass balance of the Antarctic Ice Sheet from 1992 to 2017]". In: *Nature* 558, pp. 475–480. DOI: 10.1038/s41586-018-0179-y.

Books extracts

Roger G Barry, Eileen A. Hall-McKim (2014a). "Essentials of the Earth's Climate System". In: *Essentials of the Earth's Climate System*. Vol. 1: *Essentials of the Earth's Climate System*. United States of America: Cambridge University Press, pp. 111–112.

— (2014b). "Essentials of the Earth's Climate System". In: *Essentials of the Earth's Climate System*. Vol. 1: *Essentials of the Earth's Climate System*. United States of America: Cambridge University Press, pp. 154–157.

Lowrie, William (2016). "Fundamentals of Geophysics". In: *Fundamentals of Geophysics*. Vol. 2: *Fundamentals of Geophysics*. United Kingdom: Cambridge University Press, pp. 148–158.

Webpages and online articles:

7.548, M.I.T. BE.400 / (2002). *Singular Value Decomposition (SVD) tutorial*. URL: http://web.mit.edu/be.400/www/SVD/Singular_Value_Decomposition.htm.

Lindsey, Rebecca (2002). *Collapse of the Larsen-B Ice Shelf*. URL: http://www.projectmidas.org/blog/calving/.

worldlakes.org (2004). *Lake profile - Caspian Sea*. URL: http://www.worldlakes.org/lakedetails.asp?lakeid=8762.

Observations, ESA Earth (2005). *Earth from Space: The Southern Caspian Sea*. URL: http://www.esa.int/Our_Activities/Observing_the_Earth/Earth_from_Space_The_southern_Caspian_Sea.

Interior, U.S. Department of the and U.S. Geological Survey (2006). *What is a Fault?* URL: https://geomaps.wr.usgs.gov/sfgeo/quaternary/stories/what_fault.html (visited on 06/22/2018).

Urbano, L. (2011). *Plate Tectonics and the Earthquake in Japan*. (Retrieved June 18th, 2018, from Montessori Muddle: http://MontessoriMuddle.org/). URL: http://MontessoriMuddle.org/ (visited on 06/18/2018).

California - Berkeley, University of (2012). *2012 Sumatra earthquake triggered temblors worldwide for nearly a week, research shows*. URL: https://phys.org/news/2012-09-sumatra-earthquake-triggered-temblors-worldwide.html.

Dunbar, Brian (2013). *GRACE Launch*. URL: https://www.nasa.gov/mission_pages/Grace/launch/index.html#.WyAcwYozZPZ.

Scambos, Julienne Stroeve ed and Lora Koenig (2013). *An intense Greenland melt season: 2012 in review*. URL: http://nsidc.org/greenland-today/2013/02/greenland-melting-2012-in-review/.

Boening, Carmen (2014). *Causes*. URL: https://sealevel.nasa.gov/understanding-sea-level/causes/drivers-of-change.

Leskovec, Rajaraman and Ullman (2016). *Singular Value Decomposition — Stanford University*. URL: https://www.youtube.com/watch?v=P5mlg91as1c.

Zwally, Dr. H. J. (2016). *ICESat: GLAS Instrument*. URL: https://icesat.gsfc.nasa.gov/icesat/glas.php.

Buis, Alan (2017). *GRACE Mission Making Plans for Final Science Data Collection*. URL: https://www.jpl.nasa.gov/news/news.php?feature=6947.

Carol Rasmussen, Written by (2017). *New Study Shows the Amazon Makes Its Own Rainy Season*. URL: https://www.nasa.gov/feature/new-study-shows-the-amazon-makes-its-own-rainy-season.

Foust, Jeff (2017). *GRACE mission comes to an end.* URL: http://spacenews.com/grace-mission-comes-to-an-end/.

Ong, Thuy and Alessandra Potenza (2017). *An iceberg the size of Delaware has broken off Antarctica.* URL: https://www.theverge.com/2017/7/12/15957870/section-of-larsen-c-ice-shelf-breaks-off.

SputnikNews (2017). *GRACE Under Pressure: NASA to Decommission Aging Climate Satellites.* URL: https://sptnkne.ws/f5tX.

Steve Cole, Alan Buis (2017). *Prolific Earth Gravity Satellites End Science Mission.* URL: https://www.nasa.gov/press-release/prolific-earth-gravity-satellites-end-science-mission.

Survey, United States Geological (2017). *Visual glossary.* URL: https://geomaps.wr.usgs.gov/parks/deform/gfaults.html.

Turid Austin Wæhler, Erik Sveberg Dietrichs (2017). *The vanishing Aral Sea: health consequences of an environmental disaster.* URL: https://tidsskriftet.no/en/2017/10/global-helse/vanishing-aral-sea-health-consequences-environmental-disaster.

Andersen, Morten Garly (2018). *Enorme mængder is smelter bort fra Antarktis hvert år.* URL: http://www.space.dtu.dk/nyheder/nyhed?id=6C761E96-3F86-4D9D-B384-AAF6A5B48F74.

Dunbar, Brian (2018). *GRACE Spacecraft and Instruments.* URL: https://www.nasa.gov/mission_pages/Grace/spacecraft/index.html.

Eoas.ubc (2018). *m $_m$apsmappingtool.* URL: https://www.eoas.ubc.ca/~rich/map.html.

Ingalls, NASA/Bill (2018). *Twin Spacecraft Launch to Track Earth's Water Movement.* URL: https://gracefo.jpl.nasa.gov/news/134/twin-spacecraft-launch-to-track-earths-water-movement/.

NASA/JPL-Caltech (2018). *Lasers in Space: GRACE-FO Tests New Technology.* URL: https://gracefo.jpl.nasa.gov/news/128/lasers-in-space-grace-fo-tests-new-technology/.

Starmer, Josh (2018). *StatQuest: Principal Component Analysis (PCA), Step-by-Step.* URL: https://www.youtube.com/watch?v=FgakZw6K1QQ.

Thome, Kurtis (2018). *Advanced Spaceborne Thermal Emission and Reflection Radiometer.* URL: https://terra.nasa.gov/about/terra-instruments/aster.

10.3, ArcMap (2018). *What are geographic coordinate systems?* URL: http://desktop.arcgis.com/en/arcmap/10.3/guide-books/map-projections/about-geographic-coordinate-systems.htm (visited on 06/10/2018).

Academy, Australian Space (2018). *SPACE DEBRIS REENTRY HAZARDS.* URL: http://www.spaceacademy.net.au/watch/debris/reentryhaz.htm (visited on 06/13/2018).

Centre, Theia Land Data, CNES, and LEGOS (n.d.). *Time series of water levels in the rivers and lakes around the world.* URL: http://hydroweb.theia-land.fr/.

Interior, U.S. Department of the and U.S. Geological Survey (2018). *Tectonic base map of the Sumatra subduction zone.* URL: https://walrus.wr.usgs.gov/tsunami/sumatraEQ/tectonic.html (visited on 06/19/2018).

Klemann, Dr. Volker (n.d.). *Glacial isostatic adjustment (GIA).* URL: https://www.gfz-potsdam.de/en/section/earth-system-modelling/topics/solid-earth-dynamics/glazial-isostatic-adjustment-gia/.

Mathworks (n.d.). *SVD - Singular Value Decomposition.* URL: https://se.mathworks.com/help/matlab/ref/svd.html?nocookie=true&s_tid=gn_loc_drop.

Observatory, Tectonics and the California Institute of Technology (2018). *THE SUMATRAN PLATE BOUNDARY PROJECT.* URL: http://www.tectonics.caltech.edu/sumatra/ (visited on 06/19/2018).

Program, USGS Earthquake Hazards (2018). *Earthquake Glossary.* URL: https://earthquake.usgs.gov/learn/glossary/?term=fault%5C%20plane (visited on 06/22/2018).

Technology, California Institute of (n.d.). *Analysis of the Sumatra-Andaman Earthquake Reveals Longest Fault Rupture Ever*. URL: https://www.nsf.gov/news/news_summ.jsp?cntn_id=104179.